Fiber Engineering for Extreme Environments

Fiber Engineering for Extreme Environments

a dissertation presented
by
Grant Michael Gonzalez
to
The John A. Paulson School of Engineering and Applied Sciences

in partial fulfillment of the requirements
for the degree of
Doctor of Philosophy
in the subject of
Engineering Sciences

Harvard University
Cambridge, Massachusetts

April 2019

Fiber Engineering for Extreme Environments

Abstract

Textile fibers in clothing have provided protection from heat, high-performance fibers in body armor have enabled protection from fragmentation injuries, and fiber-reinforced composites have increased the life span of products undergoing abrasive wear. All these environments provide extreme conditions for materials. A material used in each of these environments is poly(*p*-phenylene terephthalamide) (PPTA) fibers. With the common PPTA building block, its ultimate structure dictates its function: fiber weaves provide mechanical protection, fibers turned into a pulp act as insulation, and short fibers mixed into composites improve wear. The material's functionality is therefore limited by its structure. To protect from improvised explosive devices (IEDs) in the desert, a material needs to provide both mechanical and heat protection simultaneously. To enable this material, we hypothesized combining the PPTA structure of continuous fibers with the porosity of aerogels would achieve these properties simultaneously. To create the porous network, however, the fibers would need to be on the scale of 1 μm in diameter, the length scale of nanofibers. As no method exists to create PPTA nanofibers, we first developed a method to produce PPTA nanofibers. After scaling that system to produce PPTA nanofiber sheets with porous networks, we performed fragmentation and heat insulation testing to reveal that the nanofiber sheets had a 15% lower fragmentation protection and 20x the insulation ability of commercial PPTA fiber weaves. With a slight loss in fragmentation protection, the material gained the ability to provide heat protection simultaneously. In addition to providing simultaneous structures and functions, the PPTA nanofibers also improved the wear of fiber reinforced composites by changing the mechanism of wear from a volumetric wear rate to a fracture wear mechanism based on the interaction of the fiber with the matrix. The PPTA nanofibers enabled novel structure to improve functionality of materials in extreme environments.

Contents

Figure List

Acknowledgments

Thank you to my advisor Prof. Kevin Kit Parker, committee members Prof. Joanna Aizenberg, Prof. Katia Bertoldi, Prof. Jennifer Lewis, and the DBG lab members both past and present who have guided me to make this work possible. In addition, I would like to thank our United States Military Academy at West Point Collaborator COL John Burpo for help preparing samples and our Natick Combat Capabilities Development Command's Soldier Center collaborators Janet Ward, Dr. Kathleen Swana, John Song, and Dr. Stephen Fossey for help in testing samples. I would like to thank the SEAS Scientific Instrument Shop, Jesse Ward, and Stan Cotreau for their fabrication work. I am thank full for the use of the Materials Research and Science Center (MRSEC) at Harvard University for funding and use of center equipment. Finally, thank you to Prof. Kwanwoo Shin of the Biological Interfaces Lab at Sogang University for the opportunity to intern at his lab in addition to his scientific insight.

Chapter 1

Introduction

Most species need to evolve to adapt to new extreme environments. Humanity can also utilize materials engineering to overcome these challenges of extreme environments: insulation in clothing and houses allows for dwelling in deserts and tundras, the protective covering of shoes and boots allow for the crossing of vast rocky terrain, elastic ropes and sticky shoes allows for the vertical ascension of mountains, and high-performance fibers and ceramics allow for the survival in the extreme man-made environment of war. While advances to overcome extreme environments enable humanity to survive greater environments, advances to survive war trade off with advances in the lethality of war. Protection to weight is the most critical criteria for useful protection on an individual.[1, 2]

Some of the best protective materials are high-performance fibers, both woven and non-woven, due to their great strength to weight ratio protection. Current high-performance fibers, outperform their bulk material counterparts by 100x[3]. As a result we us high-performance fibers in clothing, fragmentation resistant vests, and to increase the abrasion resistance of composites. Their strength to weight ratio derives from their structure-function relations.[4, 5] Fiber materials at the macro-scale are woven together into textiles while non-woven fabrics are composed of fibers that are mechanically or chemically fused together. Fibers, the functional units of the fabric, are typically between 10 and 100 μm in diameter.[6] Fibers in general may contain amorphous or crystalline segments depending on their polymer chain building blocks and the mechanism by which they were formed. Polymers can either be flexible or rigid, hydrophobic or hydrophillic, sterochemically large or small depending on polymer chain backbone and side chain composition. High-performance fibers utilize the polymer chain to align polymer domains along the axis of the

fiber to obtain a high degree of polymer alignment leading to crystallinty, mechanical performance, and ultimately functionality. The first fibers to attain high-performance functionality were Kevlar and Twaron: Both commercial fibers were produced from a rigid rod polymer that allowed for the ability to control polymer alignment and therefore fiber functionality[6]. One of the key advances in the past twenty years in controlling fiber functionality is the development of nanofibers: fibers with a diameter of 1 μm or less. For nanofibers developed for high-performance mechanical properties, the small diameter size are constraining boundary conditions forcing the polymer to align along the principle axis of the fiber. For nanofibers designed for filtration or heat insulation, the small fibers allow for fiber entanglements, both mechanical and chemical, to create large pore sizes. While nanofibers are new, controlling fiber properties as a function of diameter is most famous by Alan Arnold Griffith who showed that decreasing glass fiber diameter from 4.2 to .130 inches increased mechanical bursting strength from 42,300 to 491,000 lbs. per sq. inch[7]. The decrease in fiber size, unlike with what is attributed to nanofibers, resulted from a probabilistic decrease in defect concentration as function of a change in volume.

Due to their characteristic length scale, nanofibers have the potential to combine the mechanisms of increased mechanical performance with the ability of nanofiber sheets to include porous networks for heat insulation[8]. This combination of mechanical strength and heat insulation will enable new materials for protection to extreme environments, in particular protection against improvised explosive devices (IEDs). Another benefit to the small size scale of nanofibers is the change in the mechanism of abrasive wear by changing the aspect ratio of particle-surface interactions. As a result, smaller fibers will improve the wear of fiber reinforced composites such as boot soles. One of the highest performing materials for these applications is the para-armid polymer poly(p-phenylene terephthalamide) (PPTA): PPTA fibers provide exceptional mechanical performance for fragmentation protection and chopped PPTA staple fibers provide heat insulation. However, to combine both structures to attain both functions simultaneously requires a new mechanism to form the nanofibers as current fiber platforms are unable to make PPTA nanofibers. To accomplish this task, we built a nanofiber system capable of producing large PPTA nanofibers, scaled that system to produce nanofiber sheets, and then utilized those fiber sheets to improve the simultaneous heat and fragmentation protection against IEDs and to improve the wear rate of boots.

Chapter 2

Immersion Rotary Jet-Spinning: A Precipitation-Based Spinning Platform Enabling Novel Nanofibers

Fibrous materials possess unique combinations of properties, such as pliability, toughness, and durability that make them an attractive material for various applications. Synthetic fiber production emerged in the 19th century and high-strength synthetic fibers such as Nylon and Kevlar® were commercialized in the 1930s and 1970s, respectively.[9, 10] Today, synthetic fibers are widely used to reinforce composite building materials, tires, sporting equipment, and armor.[11, 12] High porosity fibrous scaffolds are used for filtration, sensors, and catalysis[13] as well as for tissue engineering and regenerative medicine.[13–15, 15, 16] Since unique properties of fibrous materials derive from the high aspect ratios of fibers,[17–19] recent efforts have focused on developing techniques for producing nano-fibers with diameters less than 1 μm. Examples of commonly used nanofiber production techniques include self-assembly,[20, 21] phase separation,[22] template synthesis,[23] touch spinning,[24] magnetospinning,[25] fluidic spinning,[26–28] electrospinning (ES),[10] and rotary jet-spinning (RJS).[29–32]

ES is a popular and versatile method for manufacturing polymer nanofibers.[10, 33] However, producing nanofibers using highly charged polymers jets can be challenging due to electric field interference. For instance, ES of pure alginate[34–36] or DNA[36] dissolved in water, even into a precipitation bath, is hampered by interference from their polyelectrolyte backbones.[33, 34, 36–38] Additionally, some non-charged polymers cannot be spun using common volatile solvents such as hexafluoroisopropanol (HFIP), requiring additives to facilitate fiber formation. For instance, the addition of salts has been critical to spin meta-aramid dopes.[39–43] Moreover, polymer solution viscosity and solvent evaporation rate must be

carefully balanced in order to overcome instabilities caused by surface tension. Unless these spinning conditions are nominal, the dominance of surface tension can create a high-energy Raleigh-Plateau instability that forces the polymer-jet to bead or break apart.[29, 44, 45]

To facilitate fiber production from non-volatile solvents and from polymers with charged groups, we developed immersion Rotary Jet-Spinning (iRJS), a centrifugal dry-jet wet spinning platform. The iRJS is an evolution of our previously reported Rotary Jet-Spinning (RJS) platform wherein high centrifugal forces are applied to extrude polymer dopes into nanofiber forming jets. While the RJS relies on carrier solvent evaporation, the iRJS contains a vortex-controlled precipitation bath in which fiber solidification occurs. The precipitation bath chemically crosslinks or precipitates polymer nanofibers, removing the need for using volatile carrier solvents. By utilizing precipitation instead of evaporation, the iRJS allows the fabrication of a variety of polymer nanofibers that cannot be readily formed using conventional RJS and ES techniques. To demonstrate the broad applicability of the iRJS, we spun nanofibers using diverse material precursors that included poly (para-phenylene terephthalamide) (PPTA, brand names: Kevlar®, Twaron®), Nylon, DNA, and alginate. For biological applications, we developed pure alginate and blended alginate-gelatin nanofibers for use as tissue scaffolds. Using Kevlar® as a model high-strength material precursor, we controlled the mechanical properties of PPTA nanofiber sheets for future use in composite materials.

2.1 Engineering a Precipitation-Based Nanofiber System

Nanofibers are produced by the iRJS platform by extruding a polymer solution through an orifice of a rotating reservoir by centrifugal forces (Figure 2.1.1a). During extrusion, the solution forms a jet and undergoes jet-elongation and polymer alignment as it travels through an adjustable air gap. At the end of the

Figure 2.1.1 ***(following page)*****:** The immersion Rotary Jet-Spinning System (iRJS). a) The iRJS system controls the manufacturing of nanofibers by controlling the nanoscale properties, microscale assembly, and macroscale functionality. The iRJS spins a nanofiber solution through an orifice of a rotating reservoir. b) In an air gap, the polymer solution undergoes jet elongation, thinning while polymer chains align. After jet-elongation, the polymer solution enters the precipitating or crosslinking bath to form nanofibers. c) The streamlines of the vortex pull and collect the fibers onto the rotating collector. d) The iRJS system fabricates bulk nanofiber sheets around e) the collector with f) a removable sleeve. g) The polymer sheets were fabricated from nylon, biopolymers DNA and hydrated alginate in addition to synthetic PPTA after 30 s of spinning. These bulk sheets are comprised of h) nanofibers (scale bar = 40 m) made from the i) following materials: nylon (scale bar = 500 nm), DNA (scale bar = 250 nm), alginate (scale bar = 1 m), and PPTA (scale bar = 1 m) as revealed by SEM images. Reproduced with permission[46].

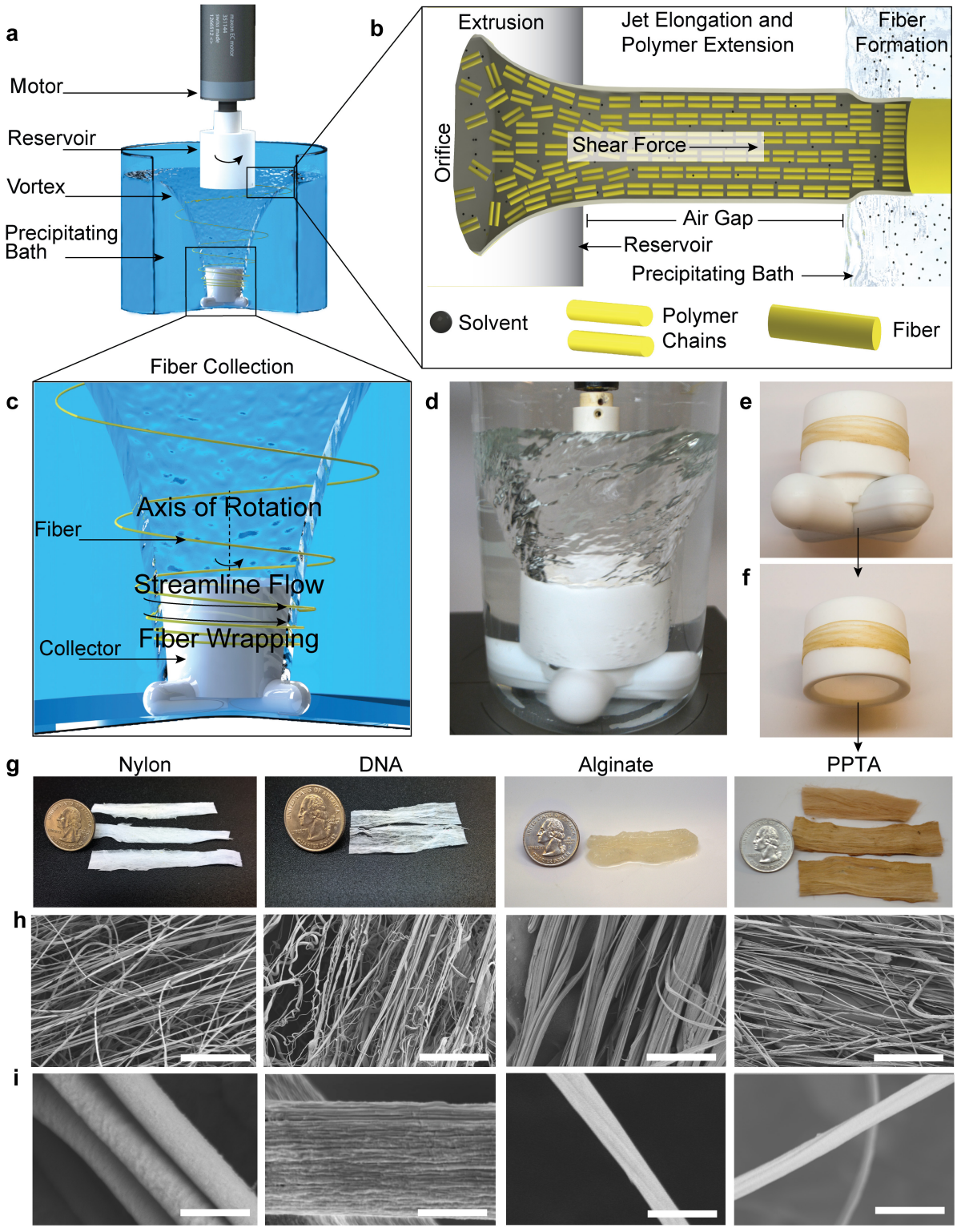
a
Motor
Reservoir
Vortex
Precipitating Bath
b
Extrusion
Jet Elongation and Polymer Extension
Fiber Formation
Orifice
Shear Force
Air Gap
Reservoir
Precipitating Bath
Solvent
Polymer Chains
Fiber
Fiber Collection
c
Axis of Rotation
Fiber
Streamline Flow
Fiber Wrapping
Collector
d
e
f
g
Nylon
DNA
Alginate
PPTA
h
i

air gap, the polymer jet enters a precipitating vortex bath where the carrier solvent diffuses out, nanofiber solidification occurs (Figure 2.1.1b), and nanofibers are collected, for instance, onto a rotating collector in the form of oriented sheets (Figure 2.1.1c-f). The selection of an appropriate liquid for the precipitating bath is critical, as it must dissolve jet carrier solvent while simultaneously precipitating or crosslinking the fiber polymer. For example, we spun PPTA or Nylon into water, DNA into ethanol, and alginate into an aqueous $CaCl_2$ solution (Figure 2.1.1g-i). The use of a precipitation bath reduces the tendency towards extruded polymer jet beading driven by the Raleigh Plateau instability,[44] which limits the parameter space of dry RJS[29] or ES.[10, 45] Before skin formation or phase separation suppresses this hydrodynamic instability, the timescale of fiber beading (Figure 2.1.2a) is governed by $\tau \approx \frac{\mu}{\gamma r}$, where μ is the solvent viscosity, γ is the surface tension, and r is the jet radius. By spinning into a bath which is miscible with the carrier solvent, but precipitates the polymer, the surface tension of the interface approaches zero, $\gamma \to 0$, increasing the time scale of bead formation, $\tau \to \infty$, (Figure 2.1.2b). As a result, iRJS fibers are bead-free (Figure 2.1.2b), provided that the air gap is sufficiently small, such that the polymer solution reaches the precipitating bath before beading occurs. To verify this mechanism, we compared the formation of nylon fibers in the RJS platform, which contains no precipitant liquid, to fibers spun into a variety of precipitant baths using the iRJS platform (Figure 2.1.2a). Using the RJS platform, we dissolved nylon in volatile hexafluoroisopropanol (HFIP) and spun fibers at 30k RPM. Under these conditions, nylon fibers formed solely through the evaporation of the volatile solvent showed significant beading (Figure 2.1.2a).

In contrast, beading was not observed in fibers produced with the iRJS platform when a water precipita-

Figure 2.1.2 ***(following page)*****:** iRJS Control Over the Morphology, Diameter, and Alignment of Sheets. a) iRJS control over the morphology, diameter, and alignment of sheets. a) Traditional nanofiber spinning systems relying on volatile solvents cause beading as described by the Raleigh–Plateau instability and revealed in SEM images of nylon (left scale bar = 20 m, right scale bar = 5 m). b) Fibers spun with the iRJS system minimizes surface tension due to the precipitating bath, delaying Raleigh–Plateau instability to produce bead-free fibers as revealed by SEM images (left scale bar = 20 m; right scale bar = 5 m). In addition to controlling fiber morphology, the iRJS controls fiber diameter by c) varying air-gap distance, d) rotation speed, and e) solution concentration (n = 3 production runs for each condition). For each mean fiber diameter, their corresponding distribution is plotted and denoted with roman numerals. The iRJS creates aligned sheets of these fibers by using the f) streamlines of the vortex to wrap the fibers around the collector. g) These resulting nanofiber sheets (scale bar = 100 m) h) were measured by OOP corresponding angle-color image algorithms (scale bar = 100 m). Across multiple spinning conditions, the iRJS nanofiber sheets are highly aligned as quantified in i) where 0 marks random order and 1 marks complete alignment. (n = 3 field of view for each spinning condition). Error bars are s.e.m., *$p < 0.05$. Reproduced with permission[46].

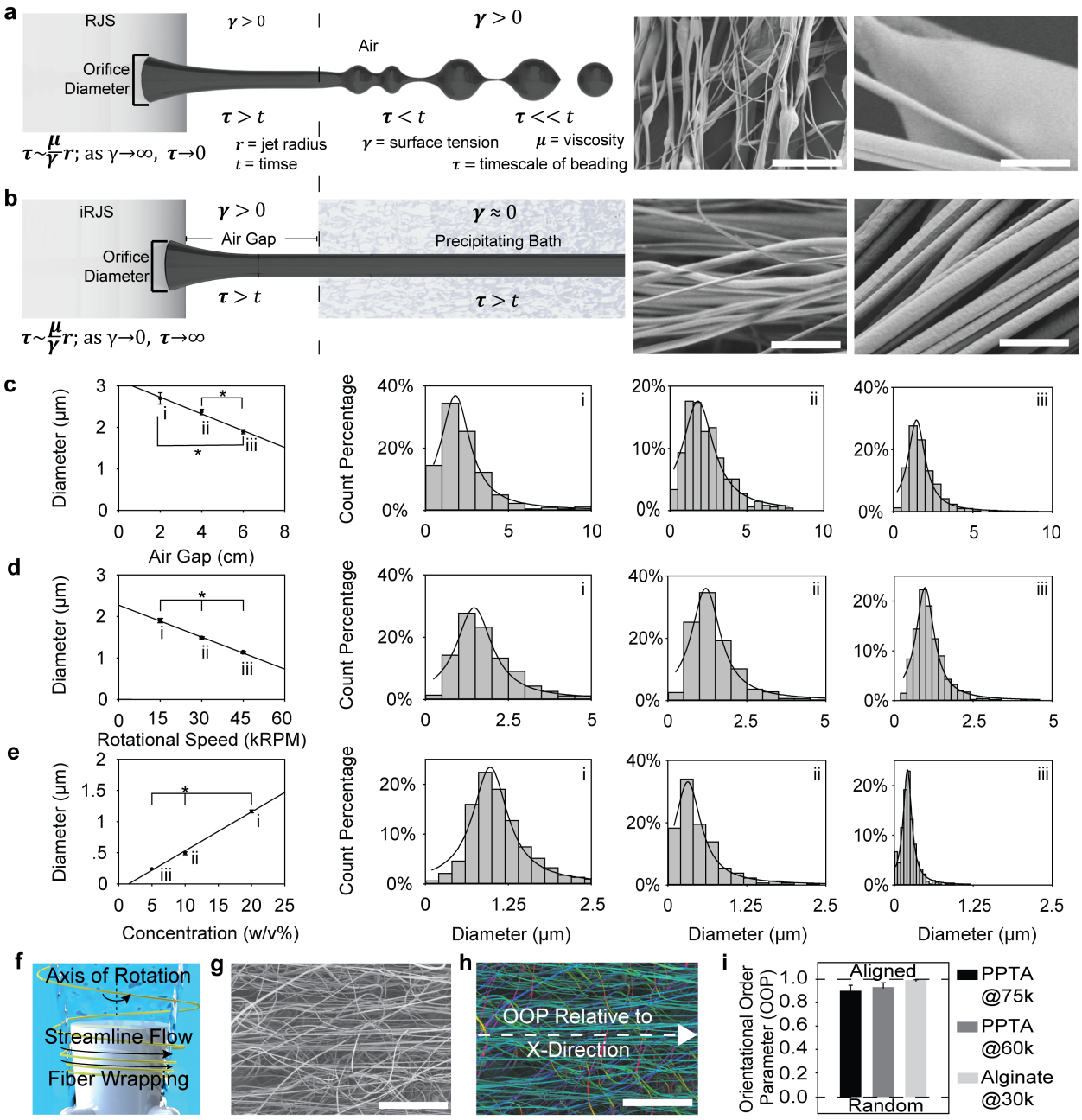
a
RJS
Orifice Diameter
γ > 0
Air
γ > 0
τ > t
τ < t
τ << t
τ~μ/γ r; as γ→∞, τ→0
r = jet radius
t = timse
γ = surface tension
μ = viscosity
τ = timescale of beading
b
iRJS
Orifice Diameter
γ > 0
Air Gap
γ ≈ 0
Precipitating Bath
τ > t
τ > t
τ~μ/γ r; as γ→0, τ→∞
c
Diameter (μm)
Air Gap (cm)
Count Percentage
d
Diameter (μm)
Rotational Speed (kRPM)
Count Percentage
e
Diameter (μm)
Concentration (w/v%)
Count Percentage
Diameter (μm)
f
Axis of Rotation
Streamline Flow
Fiber Wrapping
g
h
OOP Relative to
X-Direction
i
Orientational Order Parameter (OOP)
Aligned
Random
PPTA @75k
PPTA @60k
Alginate @30k

a

Polymer	Concentration (w/v %)	Solvent	Precipitant Bath	Speed (RPM)	Air Gap (cm)	Morphology
Nylon	20%	HFIP	Isopropanol	45k	6	No Precipitate
Nylon	20%	HFIP	Ethanol	45k	6	No Fibers, Small Precipitate
Nylon	20%	HFIP	Ethanol 50%: Water 50%	45k	6	Sponge Fibers, Sponge Beads
Nylon	20%	HFIP	Ethanol 25%: Water 75%	45k	6	Beaded Fibers
Nylon	5%	HFIP	Water	15k	6	Beaded Fibers
Nylon	5%	HFIP	Water	45k	6	Fibers
Nylon	10%	HFIP	Water	45k	6	Fibers
Nylon	20%	HFIP	Water	15k	2	Fibers
Nylon	20%	HFIP	Water	15k	4	Fibers
Nylon	20%	HFIP	Water	15k	6	Fibers
Nylon	20%	HFIP	Water	30k	6	Fibers
Nylon	20%	HFIP	Water	45k	6	Fibers
Nylon	20%	HFIP	Water	45k	6	Fibers

b c

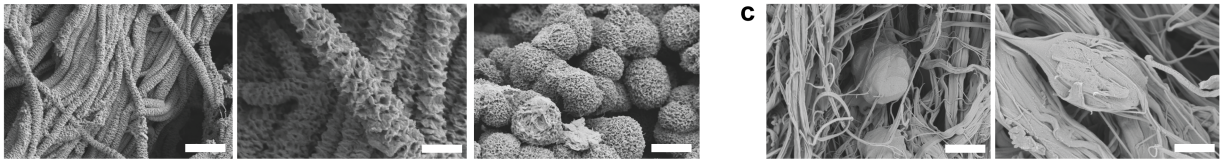

Figure 2.1.3: Nanofiber Morphology as a Function of Bath Concentration. a) Table of nylon precipitates from the iRJS ranging from no formation to bead-free fibers. b) SEM images of sponged fibers and beads formed by spinning nylon dopes into a 50-50 mixture of water-ethanol precipitant bath (left scale bar = 5 m, middle scale bar = 1 m, right scale bar = 5 m). c) SEM images of beaded nylon fibers (left scale bar = 2 m, right scale bar = 1 m) purposely formed in the iRJS using a 75-25 mixture of water-ethanol to show that if there is an interfacial tension between the precipitant and the jet, beading may occur. This interfacial tension was created by doping water with ethanol, a liquid non-miscible with HFIP. (n = 3 production runs).

tion bath was used (Figure 2.1.2b). Water was chosen for the precipitation bath because it is miscible with HFIP, resulting in negligible interfacial tension between the jet-bath interface. Notably, after adding 25% vol. ethanol to the water precipitation bath, beading was observed, as ethanol is non-miscible with HFIP, and thus increased interfacial tension. By further increasing ethanol content to 50%, severe beading and further defective morphologies were observed (Figure 2.1.3).

While the precipitant bath influences fiber morphology, varying iRJS system parameters (speed, concentration, air gap length) enables the production of fibers with tunable diameters. For the case of nylon fibers, average fiber diameter decreased with increasing air gap distance (2 cm < d < 6 cm) and extruder rotation speed (15 kRPM < ω < 45 kRPM). In contrast, fiber diameter increased with increasing weight per volume solution concentration (5% w/v < C < 20% w/v). Within this parameter space, average nylon fiber diameters of 250 nm to 2.75 μm were produced (Figure 2.1.2c-e, Figure 2.1.4). Reconfiguration of

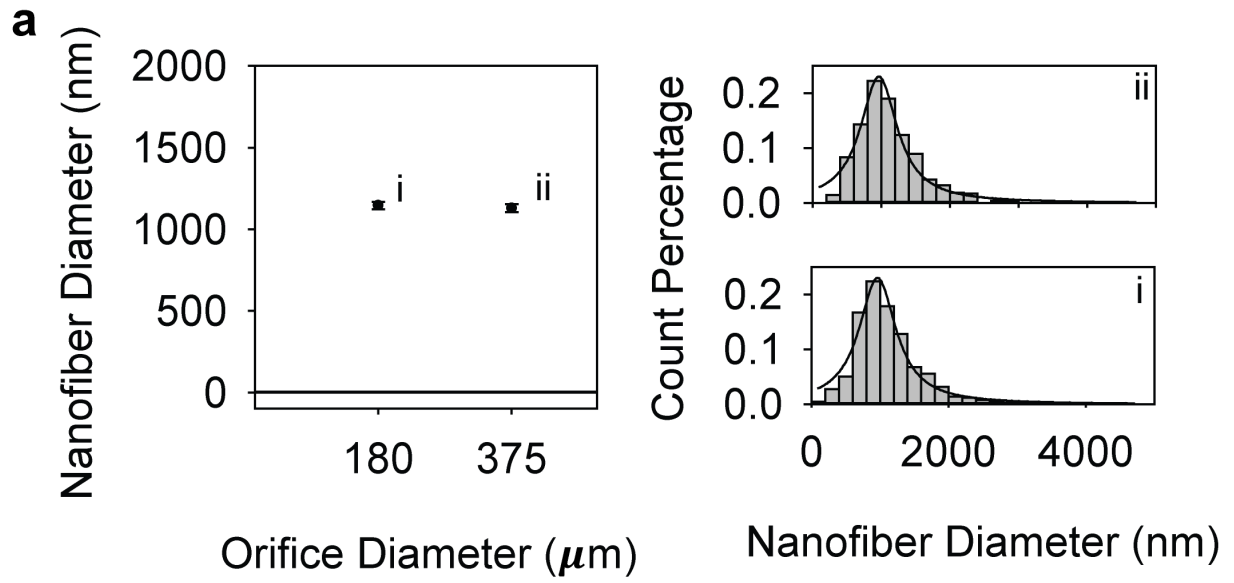

Figure 2.1.4: Effect of Orifice Diameter on iRJS Spun Nanofibers. a) There was no statistically significant change ($p > .05$) in nanofiber average diameter or distribution using orifices of different sizes. ($n = 3$ production runs).

the precipitating bath vortex and fiber collector allows production of nanofiber constructs in a variety of structural arrangements. For instance, highly aligned anisotropic sheets are obtained by using a rotating drum collector (Figure 2.1.2d). We quantified the anisotropy of such sheets using an orientation order parameter[47] (OOP) metric ($0 \leq OOP \leq 1$) with perfect alignment normalized to a value of one. The iRJS nanofiber sheets had OOP values approaching 1 ($OOP > 0.95$), indicating near perfect alignment (Figure 2.1.2f-i). Nanofiber yarns can also be produced using a funnel collection method in place of a rotating collector (Figure 2.1.5), applying a similar practice used in ES yarn collection systems.[48–50] Finally, randomly oriented nanofibers can be achieved by adjusting the vortex to wrap the fibers above the collector (Figure 2.1.5).

2.2 Enabling DNA and Alginate Nanofibers

The fabrication of bio-polymer nanofibers for bio-medical applications often requires the use of a non-volatile aqueous carrier solvent. Using a precipitating solvent, such as ethanol in the iRJS, DNA bio-polymer nanofibers can be readily made using distilled water as carrier solvent, (Fig 1g-i). Additionally, aqueous precipitation baths can be used by applying crosslinking agents to generate stable fibers. As an example,

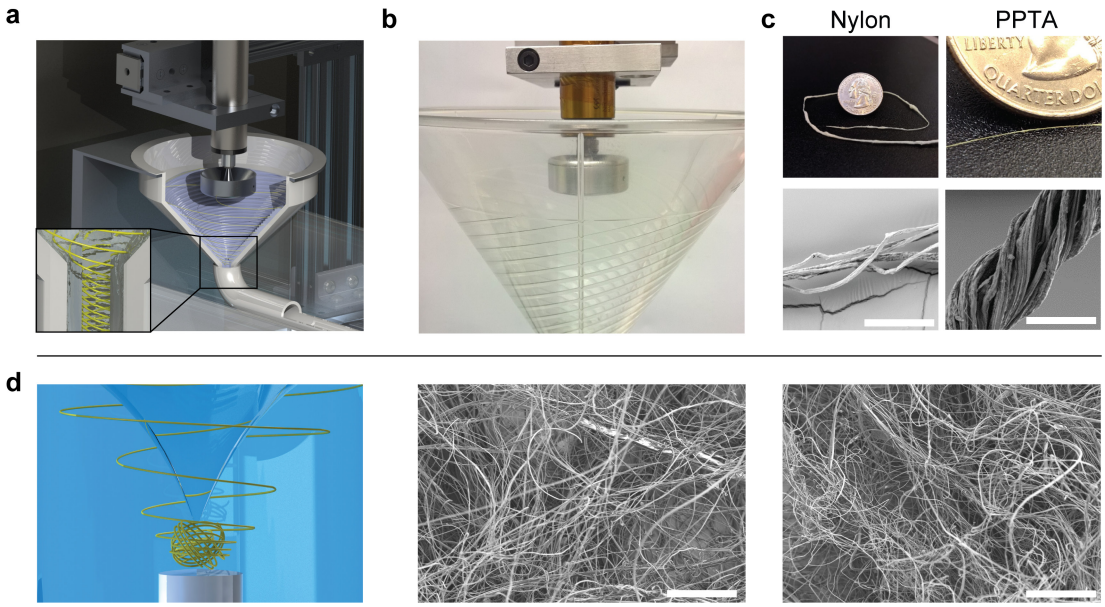

Figure 2.1.5: Additional Collection Methods of the iRJS. a) Using a funnel collection system, b) the streamlines of the vortex wrap individual nanofibers into yarns, allowing for the manual collection of c) nylon and PPTA nanofiber yarns (scale bars = 50 m). The vortex was created by having an inlet precipitant fluid flow into and out of a funnel at a rate that created and sustained the vortex. d) In order to collect isotropic and unaligned nanofibers, a vortex terminating above the collector will cause the nanofibers to wrap randomly around each other as seen in SEM images of randomly distributed nylon nanofibers (scale bars = 100 m).

we used the iRJS to produce nanofibrous alginate scaffolds crosslinked in an aqueous $CaCl_2$ bath. Alginates are naturally occurring polysaccharides used in food products[51, 52] and for biomedical applications that benefit from alginate's biocompatibility, low toxicity, and mild gelation conditions.[15] Medical uses of alginates include drug delivery vehicles[53, 54] and tissue engineering scaffolds,[55, 56] where cell-adhesive molecules are bound to alginate hydrogels to promote cell attachment.[57] Although alginate nanofibers can be produced by ES, interference between the electric field and the alginate polyelectrolyte backbones[33, 34, 36, 38] must be overcome, for example, by spinning in a mixed glycerol-water solvent[58] or by using a carrier polymer such as poly(ethylene oxide).[34–36, 57, 59–61] Leveraging the ability of the iRJS to fabricate aligned nanofiber sheets, we produced alginate and blended alginate-bioprotein nanofibers, and explored their potential for skeletal muscle tissue engineering with tunable size and modulus (Figure 2.2.1a,b). Tissue engineering scaffolds are designed to mimic properties of the extra cellular matrix in order to promote cell adhesion and guide tissue morphogenesis. Biocompatibility of naturally-derived materials produced using non-toxic methods are advantageous because they can be

more readily translated to clinical applications.[15, 16] Thus, we produced anisotropic nanofibrous scaffolds based on alginate blended with gelatin to promote cell adhesion. Gelation in $CaCl_2$ proved sufficient to produce nanofibers from solutions in which the gelatin concentration was as high as 50 %. By varying alginate-gelatin concentrations and subsequent gelatin crosslinking conditions, we produced scaffolds with elastic modulus values ranging between 5 - 60 kPa (Figure 2.2.1c). These values are comparable to native skeletal muscle (Supporting Information). In addition, our scaffolds were anisotropic (Figure 2.1.2f) and guided anisotropic cell assembly (Figure 2.2.1d-f). We seeded these scaffolds with C2C12 myoblasts and verified the scaffold's support of cell attachment, proliferation, and differentiation. C2C12 myoblasts could either be matured in situ, following 1 week of culture in differentiation media (Figure 2.2.1e), or could be maintained in their immature single nucleated state within these scaffolds for up to 2 months (Figure 2.2.1f). These experiments demonstrate that co-spinning alginate with cell-adhesive bioproteins (e.g. gelatin) provides a simple and effective means of producing blended alginate-bioprotein nanofibers. Similarly, through the inclusion of nutritional proteins in these nanofibers (Figure 2.2.2), fibrous alginate scaffolds may achieve nutritional and medical goals while simultaneously enabling engineering of texture and taste, for future applications such as synthetic and cultured foods.[62–64]

2.3 Enabling Para-Aramid Nanofibers

Beyond nanofiber production based on common carrier or aqueous solvents, the iRJS platform is well-suited for fabrication of nanofibers based polymers which requires the use of highly protic non-volatile solvents. To demonstrate this, we applied the iRJS capabilities for spinning Kevlar®-based para-aramid nanofibers, which mandates that concentrated sulfuric acid is used as carrier solvent. Poly(para-phenylene terephthalamide) (PPTA, the polymeric material of commercial Kevlar® and Twaron®) is a class of ultra-strong temperature-resistant para-aramids with broad uses that include ballistic apparel, brake and transmission friction parts, ropes and cables, and reinforcement of rubbers and other composites.[6, 12] Commercial PPTA fiber diameters are on the order of 10 μm and possess an inhomogeneous core-skin morphology that depend on proprietary production processes.[65–68] Reducing fiber diameter will be of interest for use in composites, where the surface area-to-volume ratio of nanofibers can lead to improved adhe-

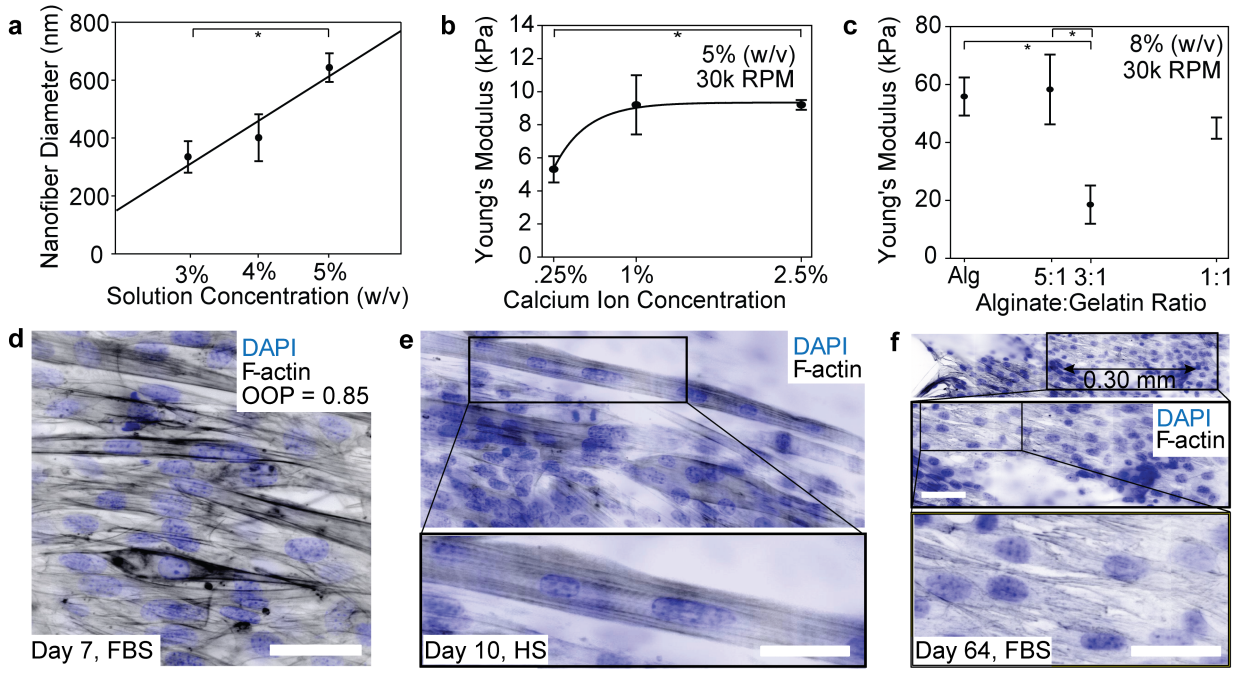

Figure 2.2.1: iRJS Alginate–Gelatin Nanofiber Scaffolds Cultured with C2C12 Myoblasts. a) Alginate nanofiber diameter depends on solution concentration (n = 3 production runs). b) Alginate nanofiber sheet mechanical strength depends on precipitation bath ion concentration (n = 3 for each condition). c) The cellular scaffolding Young's modulus depends on alginate–gelatin ratio (n = 3 for each condition). d) C2C12 myoblasts in 3D alginate–gelatin scaffolds with anisotropic orientation (scale bar = 20 m). e) C2C12 maturation induced by culture in media supplemented with horse serum (HS) (scale bar = 20 m). f) Long-term (64 d) C2C12 proliferation in an immature state using high concentration fetal bovine serum (15% FBS) (scale bars = 20 m). DAPI and F-actin stains are shown with an inverted color-map to improve contrast. Error bars are s.e.m., *p $<$ 0.05.). Reproduced with permission[46].

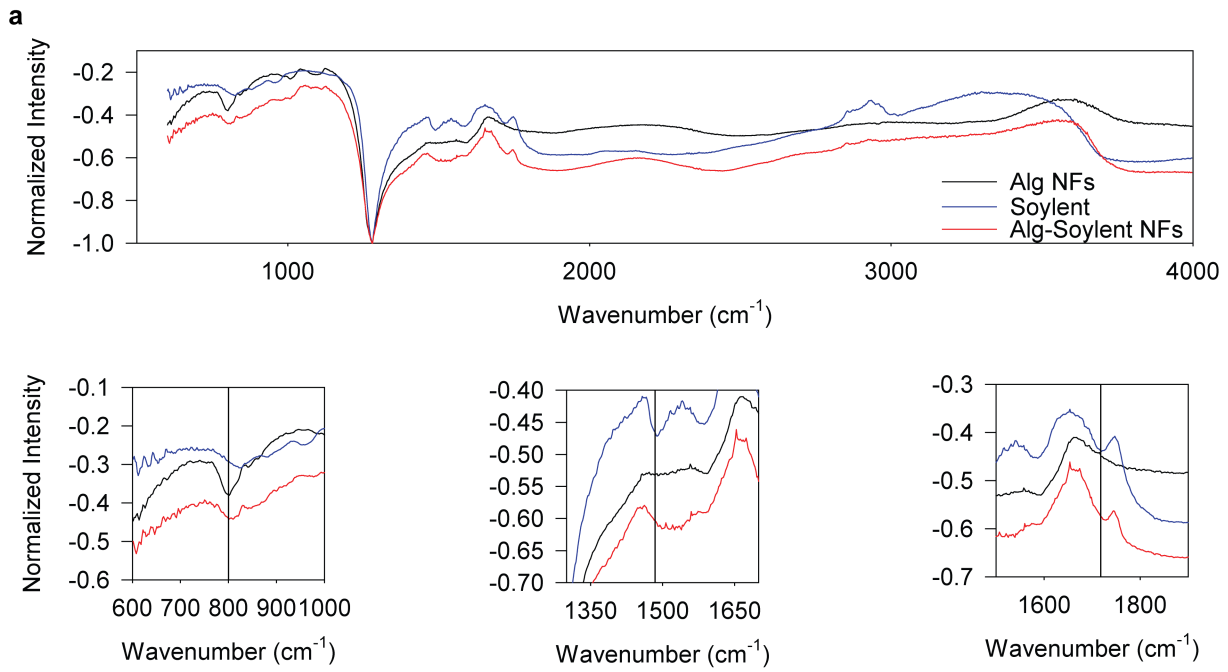

Figure 2.2.2: Preservation of Proteins Co-Spun within Alginate Nanofibers. a) In preliminary experiments, we spun alginate blended with a popular meal replacement powder, Soylent (Rosa Labs, Los Angeles CA), and observed Soylent inclusion within the alginate matrix by qualitative comparison of averaged FT-IR spectra. (n = 3 production runs).

sion to the matrix and strengthening of the composite.[17, 69] Production of PPTA nanofibers using ES has been described.[70, 71] However, complications with low and unreliable production yields have been reported.[42, 71, 72] Alternative approaches to fabricate para-aramid nanofibers include chemical cross-linking of hydrolyzed or monomeric PPTA into short micron-long nano-fibrils.[73, 74] In contrast, the iRJS is capable of higher throughput production of PPTA nanofibers with intact chemical structure.

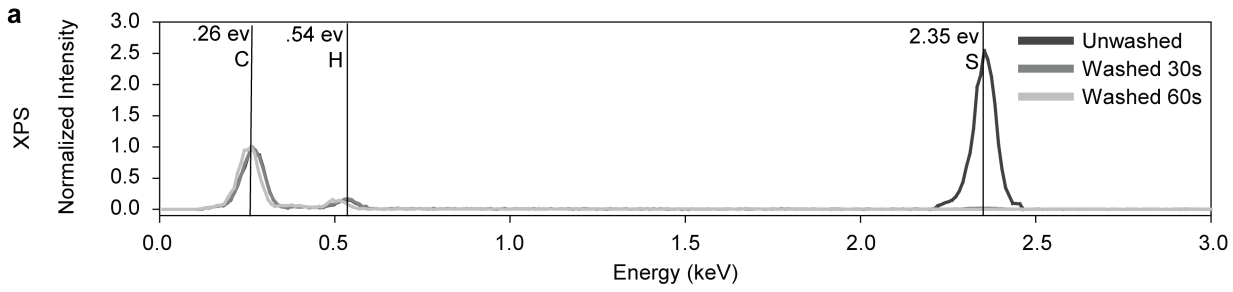

Figure 2.3.1: Elemental Analysis of PPTA Nanofibers. a) Energy Dispersive X-Ray Spectroscopy (EDS) reveals the atomistic components of the PPTA nanofibers, detecting carbon, hydrogen peaks, and sulfur peaks for unwashed PPTA nanofiber sheets and only carbon and hydrogen peaks for washed samples.

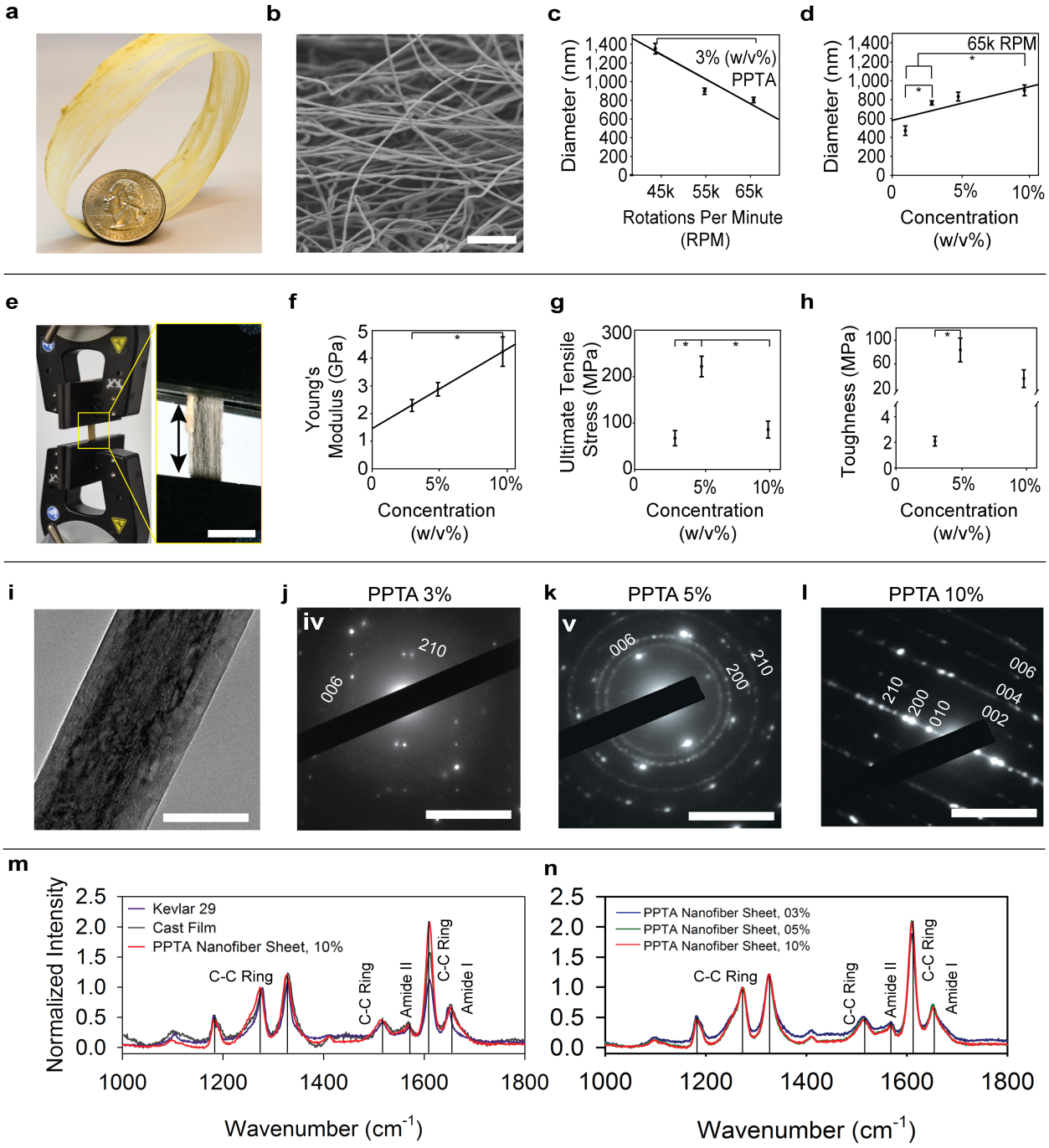

Figure 2.3.2: iRJS PPTA Nanofiber Sheets with Control Over Nanofiber Size and Mechanical Strength. a) PPTA sheets are composed of b) nanofibers (scale bar = 20 m) with an average diameter dependent on c) spinning speed and d) polymer concentration. (n = 3 production runs). e) Uniaxial tensile testing was performed to determine the mechanics of fabricated PPTA sheets including f) Young's modulus, g) tensile stress, and h) toughness (n = 3 production runs). i) TEM imaging of the nanofibers (scale bar = 150 nm) allows for imaging of the selected area diffraction of the j) 3%, k) 5%, l) 10% PPTA nanofibers and designation of Miller Indices (scale bars = 5 nm-1). m) Representative Raman spectrum of commercial Kevlar microfibers, cast film, and nanofiber sheets are graphed for comparison in addition to n) 3%, 5%, 10% PPTA nanofiber sheets spectrums. Error bars are s.e.m., *p $<$ 0.05. Reproduced with permission[46].

Using the iRJS, we spun Kevlar® dissolved in sulfuric acid at various concentrations into an aqueous precipitation bath. In the bath, sulfuric acid is diluted 1000 times and fibers solidified. To ensure that residue sulfuric acid did not degrade the nanofibers over time, we additionally washed the nanofiber fabrics with distilled water for 30 seconds followed by a 1 hour drying step at 100°C: The successful removal of sulfuric acid impurities was confirmed by energy-dispersive X-ray spectroscopy (EDS) (Figure 2.3.1). Applying this procedure, we fabricated PPTA nanofibers with various diameters and tensile strength. Fiber diameter was controlled in the iRJS by adjusting polymer concentration and the shear forces applied via variable rotational speed. For 3% (wt/v %) polymer solutions, increasing spinning speed from 45k RPM to 65k RPM decreased nanofiber diameter from 1300 nm to 800 nm (Figure 2.3.2a). On the contrary, increasing concentration increased nanofiber diameter. Spun at 65k RPM, PPTA concentrations of 1, 3, 5, or 10 % (wt/v %) produced sheets of nanofibers with mean diameters of 500, 800, 850, or 900 nm, respectively. (Figure 2.3.2a-d).

To determine the mechanical properties of the PPTA nanofibers, we performed uniaxial tensile testing of macroscopic nanofiber sheets, spun at 65k RPM at varying PPTA concentrations (Figure 2.3.2e-h). The 10% PPTA fiber sheets displayed the highest Young's modulus (Figure 2.3.2f). However, the 10% sample displayed lower ultimate tensile stress compared to the 5% sample (Figure 2.3.2g). Also, compared to higher PPTA concentrations, the PPTA nanofiber sheets spun from 3% precursor solutions had lower ultimate tensile stress and Young's modulus (Figure 2.3.2d). All the macroscopic PPTA nanofiber sheets had lower Young's modulus and ultimate tensile stress compared to the reported values for Kevlar types 29 and 49.[6, 73] However, this apparent difference may be caused by uneven load distribution in the nanofibrous network.[75, 76] For instance, a 1000-fold difference in apparent Young's modulus has been reported for single PCL nanofibers, compared to values measured for macroscopic sheets composed of the same fibers.[75] Assuming that the fibers of the anisotropic sheets span the entire sheet length, the toughness, the total amount of energy required to fracture all the fibers in the sample, whether in concert or one by one, will be less influenced by disorganization of the nanofiber sheets.[77, 78] To this point, the tensile toughness of the highly crystalline 5% and 10% nanofiber sheets were 81 ± 20 MPa and 33 ± 14 MPa respectively (Figure 2.3.2h), which is comparable to that of commercially available microfibers re-

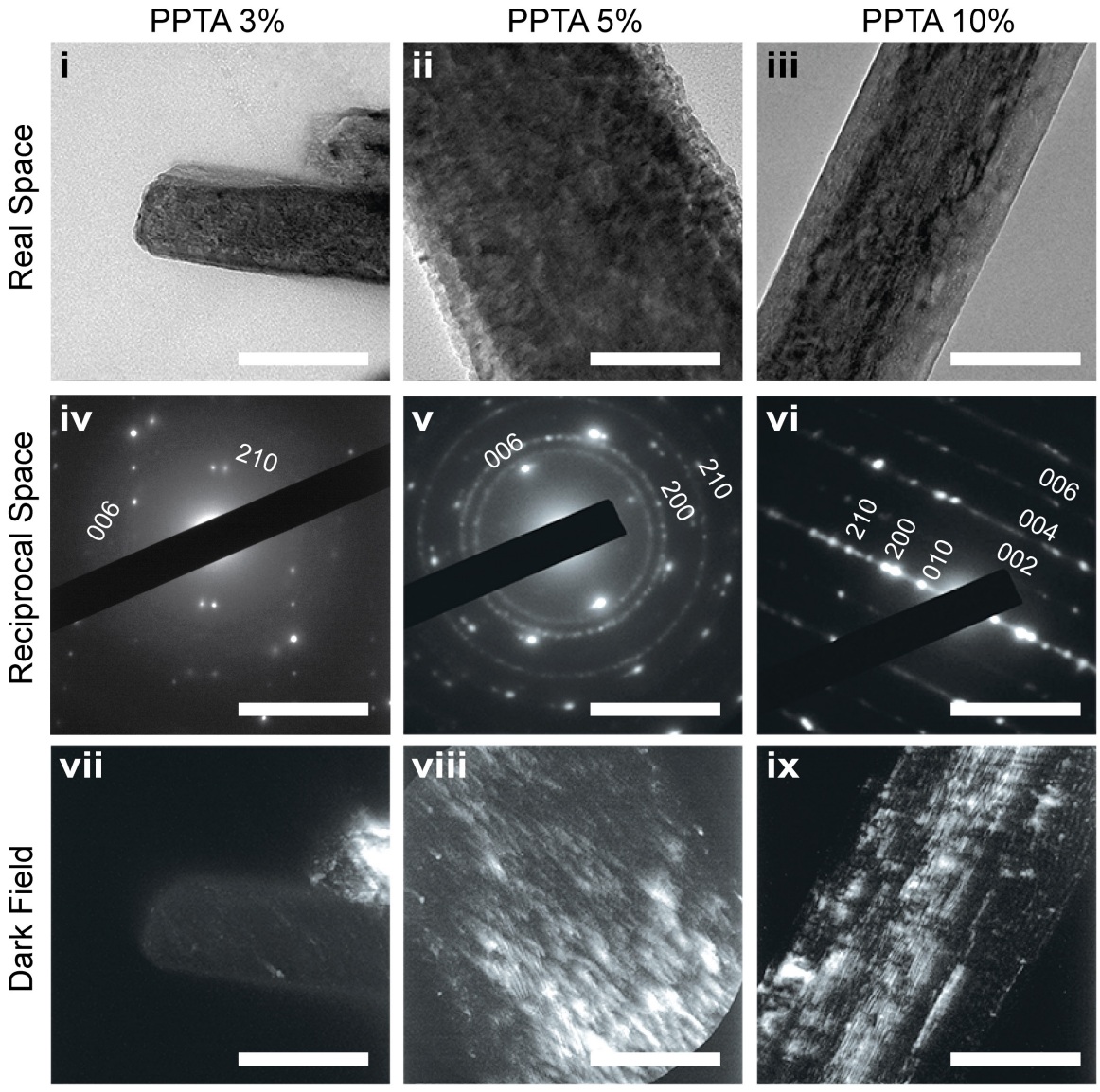

Figure 2.3.3: TEM Images of PPTA Nanofibers Across Increasing Polymer Concentration. Real space imaging of PPTA nanofibers (scale bars = 100 nm), their corresponding selected area reciprocal space diffraction images (scale bars = 5 nm^{-1}), and dark field images (scale bars = 100 nm).

ported at 50 MPa.[79] These findings are promising because high toughness is central to a wide range of high-performance material applications.[6, 79]

For commercial PPTA fibers, Young's Modulus increases with increasing crystallinity while toughness decreases.[11, 80] To determine the relationship of PPTA nanofiber mechanics with crystallinity, we evaluated the local crystallinity of single PPTA nanofibers using transmission electron microscopy (TEM) (Figure 2.3.2i-l). The 3%, 5%, and 10% (wt/v %) precursor solutions spun at 65k RPM all produced semi-crystalline PPTA nanofibers (Figure 2.3.2m-n, Figure 2.3.3) without a loss in the PPTA polymer bond chemistry (Figure 2.3.4). For the 3% fibers, amorphous ring diffraction caused by randomly aligned polymer chains was dominant (Figure 2.3.2j), while for the 5% and 10% samples, discrete diffraction with high local band intensity was seen (Figure 2.3.2k,l), indicative of aligned polymer chains and crystalline domains. Furthermore, for the 10% sample, the meridial (002, 004, 006) and equatorial (010, 200, 210) diffraction bands along with a crystalline core and amorphous skin were observed (Figure 2.3.3). These variations follow the trend in Young's moduli observed in the mechanical tests of the 3, 5 and 10% samples, as increased crystalline morphology should lead to stiffer, more brittle fiber materials. Nevertheless, when investigating the bulk crystallinity of macroscopic fibrous sheets using Raman (Figure 2.3.2m,n), we observed no quantifiable differences between the nano-fibrous samples (Figure 2.3.4). In these tests, all three nanofiber samples had comparable degrees of crystallinities which were higher than a cast film comparison, but significantly lower than that of a commercial Kevlar® microfiber reference (Figure 2.3.5). This inconsistency between the local crystallinity as observed by TEM and the bulk measurements relying on Raman, might arise from TEM imaging relying on fibers of diameters smaller than the average of the production run. It might also indicate that only local areas of increased crystallinity are present in the high concentration samples.

Nevertheless, the iRJS PPTA nanofibers possess potentials due to their small diameter. While commercial fiber diameters typically range from 10 – 20 um,[6] the significantly smaller diameter of the iRJS PPTA nanofibers (500-1000 nm) provide a 10 – 20 times increase in surface area-to-volume ratio. For composite materials, the smaller diameter PPTA nanofibers may enhance fiber dispersion within matrix materials, increasing uniformity, minimizing local stress concentrations, and increasing the number of fibers available

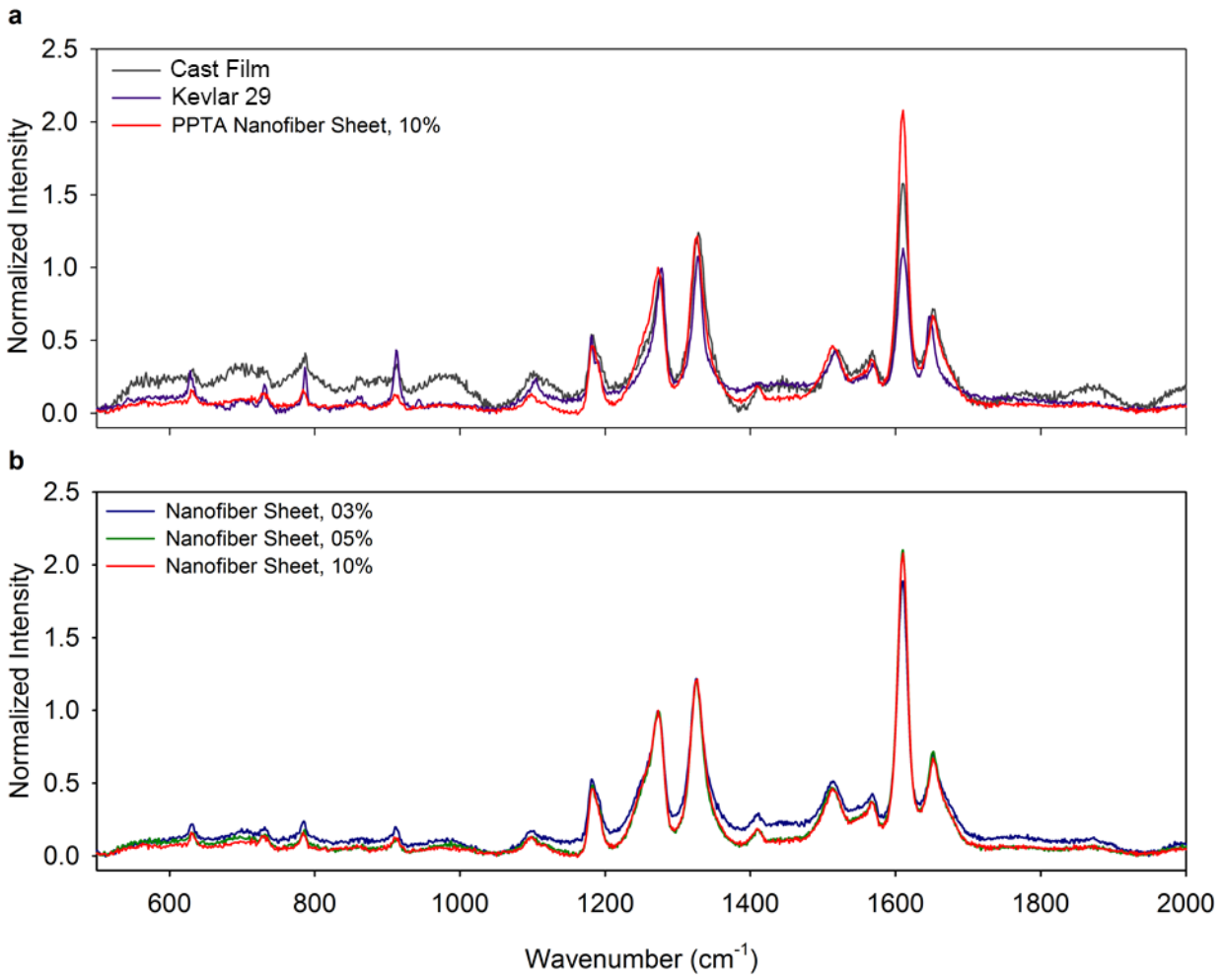

Figure 2.3.4: Raman Spectroscopy of PPTA Nanofibers, commercial Kevlar, and cast film. a) Raman spectrums of PPTA Nanofibers, commercial Kevlar, and cast film. b) Raman spectrums of nanofibers at spun from different concentration solutions.

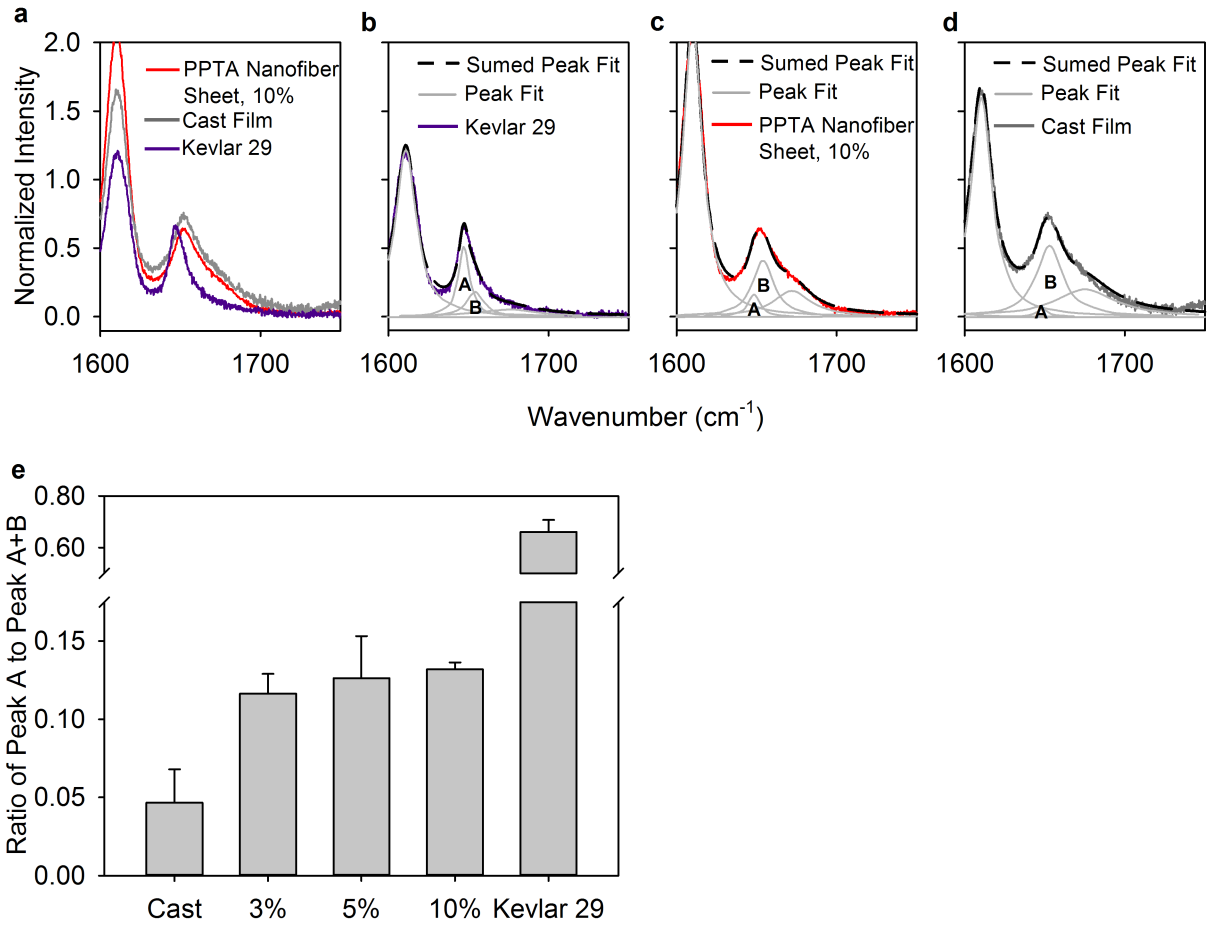

Figure 2.3.5: Raman Bond Analysis of PPTA Nanofibers, Cast Film, and Commercial Kevlar. Focusing from a general Raman spectrum, a) the 1640-1680 Amide I region of the samples to provide an approximation of crystallinity. Peak determination for the crystalline 1648 cm-1 and amorphous 1654 cm-1 regions of b) commercial fibers, c) nanofibers, d) cast film. Comparing the area of the crystalline peak to the total area of the Amide I allows for an e) approximation of crystallinity. Cast film and commercial fibers agree with literature values. In addition, the full width half max (FWHM) of the nanofiber sheets are narrower on average than the cast film indicating less variability between bonds and therefore more ordered structure (n = 3).

for bridging crack formations.[81] Furthermore, the higher surface area-to-volume ratio of nanofibers can improve adhesion to the matrix, strengthening the composite[69] as seen with other nanofiber composites[17] with possible application towards composite materials for ballistic protection such as helmets.

2.4 Summary

The iRJS platform described here minimizes surface tension and fiber beading by spinning a polymer solution into a liquid bath. The bath chemically crosslinks or precipitates the polymer without the need for a volatile solvent. Adjusting the iRJS system parameters (air gap distance, rotational speeds, and solution concentration) enables control over nanofiber diameter. By avoiding the need for solvent evaporation and electric charge, the iRJS enables straight-forward production of PPTA, Nylon, DNA, and pure or blended alginate nanofiber sheets. Structural, mechanical, and biochemical properties of these nanofiber materials were controlled within the broad iRJS parameter space. Significantly, this wide range of nanofibrous materials was achieved without limiting production throughput.

2.5 Experimental Design

Design and Assembly of the iRJS: The iRJS system was custom built with the following parts: a 250 watt DC motor (35114, Maxon Percision Motors Inc., Fall River, MA) with variable speeds from 1,000 to 80,000 RPMs, a motor control board (306089, Maxon Precision Motors Inc., Fall River, MA), a microcontroller (Arduino Due, Arduino LLC), and a potentiometer. Changing the resistance of potentiometer changed the voltage supplied to and the speed of the motor. The rotating reservoir was custom manufactured from polysulfone or aluminum and included one 175 or 375 μm diameter orifice. The precipitating bath was contained in a 2L beaker or a custom-built polycarbonate container. A stir plate with variable power drove the stir bar and collector. The speed of the spinning reservoir ranged from 15,000 to 65,000 RPM, while collector speed was 350 RPM. The collector was machined from a rod of polytetrafluoroethylene (PTFE) into a cylinder with an opening for the stir bar. For the funnel collection system, precipitant was pumped into a funnel to create a vortex. For both collection methods, the air gap distance may be controlled independently by changing the height of reservoir relative to the vortex. The precipitating bath used

is a miscible liquid to the solution solvent while not having the ability to solubilize the polymer. For example, nylon dissolved in hexafluoroisopropanol was spun into water, DNA dissolved in water into ethanol, alginate dissolved in water into calcium chloride solution, and PPTA dissolved in sulfuric acid into water.

Solution Preparation and Spinning: To make solutions of PPTA-sulfuric acid, PPTA (339741, McMaster-Carr, Elmhurst, IL) was dissolved into 99.999% sulfuric acid (339741, Sigma Aldrich, St. Louis, MO) and heated at 70°C for 24 hours or until dissolved. The PPTA-sulfuric acid solutions were spun at 70°C and at variable speeds. Low viscosity alginate (A0682, Sigma Aldrich, St. Louis, MO) was used for measuring the effect of Ca2+ ion concentration on mechanical strength and alginic acid sodium salt (180947, Sigma Aldrich, St. Louis, MO) was used for cellular scaffolding to increase the mechanical strength of the alginate to more closely approximate skeletal muscle. To avoid gelation, alginate-gelatin solutions were spun at 60°C and at 30k RPMs. Experimental procedures were carried out in a chemical hood to limit exposure to hazardous materials used in the fiber spinning process. If increasing concentration of carrier solvent diffusing into the bath hinders fiber formation, it is recommended to change the bath or utilize the funnel collection system to ensure fresh precipitant is used.

Scanning Electron Microscopy and Energy Dispersive X-Ray Spectroscopy: A field emitting electron microscope (FESEM Supra 55VP, Zeiss, Oberkochen, Germany) was used at a voltage of 3kV to measure the diameter and to reveal the microscale assembly of the nanofibers. For sample preparation, 8 mm diameter samples were cut and adhered via carbon tape to 12 mm aluminum SEM stubs and then plated with a 10 nm coating of Platinum/Palladium (Pt/Pd) using a Quorum Sputter Coater (EMS 300T D, Quorum Technologies, Sussex, United Kingdom) to avoid charge build-up during imaging. Diameter measurements of nanofibers were done manually with ImageJ. Energy Dispersive X-Ray Spectroscopy (EDS) in the Zeiss SEM was performed in order to detect sulfuric-acid impurities in the final nanofiber PPTA fabric. For EDS analysis, we used the same method as above for the SEM preparation minus the Pt/Pd coating. EDS was performed at 15kV energy to produce enough signal for detection.

Transmission Electron Microscopy: Transmission electron microscopy (TEM) was used to view the

nanoscale features and crystallinity of the PPTA nanofibers. All TEM imaging was performed on a JEOL 2100 TEM (JEOL, Peabody, Ma). Due to the small size of the fibers and the carbon content of the PPTA polymers, the PPTA nanofibers were imaged directly on a TEM sample grid at 80 kV. Miller Indexing of the diffraction patterns was determined using known lattice parameters (a = .78 nm, b = .519 nm, c = 1.29 nm) and crystal structure (orthorhombic).[6, 82] To ensure accuracy of measurements, the 80 kV diffraction patterns were calibrated using a known aluminum sample.

Tensile Testing: Uniaxial tensile testing was performed with a mechanical tester (5566, Instron, Norwood, MA). The end of PPTA nanofiber sheets were embed in epoxy and taped to avoid stress concentrations at the location of the clamp and sample interaction. Tests were performed under a constant strain rate of 500 mm/min at a gauge length of 2 cm. The maximum strain rate was chosen to most closely replicate the mechanical environment of high performance applications. Young's modulus was calculated as the slope of stress-strain curve, ultimate tensile stress was calculated as the maximum value of the stress-strain curve, and toughness was calculated as the area underneath the stress-strain curve. The area occupied by the nanofibers in the sheets was calculated by measuring the area of the sheet and then subtracting the void space of the fibers based on density difference between the sheet and a single fiber. For PPTA nanofibers tested mechanically, fiber diameters ranged from 750 – 900 nm, density was .43 gm/cm3, and OOP values were .95 or greater. Mechanical testing of alginate-gelatin nanofibers after transglutaminase crosslinking (Modernist Pantry, Portsmouth, NH) crosslinking was obtained with a biaxial tension test (CellScale BioTester, Waterloo, Canada). For alginate nanofibers tested mechanically, fiber diameters ranged from 600 – 800 nm, density was 1.02 gm/cm3, and OOP values were .95 or greater.

Skeletal muscle cell seeding and culture: Alginate-gelatin produced scaffolding with post-processing transglutaminase (Modernist Pantry, Portsmouth, NH) were used as a cellular scaffolding. Mouse myoblast cell lines (C2C12, ATCC CRL-1772) were seeded at 50,000/cm2 and cultured in a growth medium of DMEM culture medium (11995-065, Gibco, Carlsbad, CA) supplemented with 15% fetal bovine serum (Invitrogen, Carlsbed, CA). C2C12 maturation medium was DMEM/F-12 (12-719F, Lonza, Walkersville, MD) supplemented with 5% horse serum (Gibco, Carlsbad, CA).

Fourier Transform Infrared (FT-IR) and Raman Spectroscopy: A Bruker FT-IR Microscope (Lumos, Bruker, Billerica, MA) was used in attenuated total reflection (ATR) mode to measure the infrared spectra of the nanofibers. Horiba Multiline Raman Spectrometer was used with a 633 nm laser and 1800 mm grating. LabSpec 6 from Horiba was used to perform peak analysis and fitted to literature values.[83, 84]

Statistical Analysis: Nanofiber diameter and mechanical properties were evaluated using SigmaPlot software (v12.5, Systat Software Inc., San Jose, CA). Nylon size dependence (Figure 2.1.2c), fiber diameter versus polymer weight concentration (Figure 2.2.1a, Figure 2.3.2b) and fiber diameter versus rotations per minute (Figure 2.3.2a) failed the Shapiro-Wilk normality test, and thus were evaluated using Kruskal-Wallis One Way Analysis of Variance on Ranks using the Dunn's Test for post hoc analyses. Mechanical data (Figure 2.2.1b-c, Figure 2.3.2d) passed the Shapiro-Wilk normality test and were thus compared using One-Way ANOVA, and the Tukey test for post-hoc analysis. For all statistical analyses, p-values less than 0.05 were considered statistically significant.

Chapter 3

Scaling the Platform to Produce Continuous Nanofiber Sheets

While the iRJS is capable of producing novel nanoifber from non-volatile dopes, the work presented previously only enabled the fabrication of small samples (1 by 5 cm) from 3 mL solutions. This small sample size inhibits the production of fibers in large enough quantities for testing biopolymer wound dressing on pigs or para-armid fiber for fragmentation testing as edge affects influence its performance[85]. To enable greater volume of production, continuous spinning of solutions needs to be the goal as bath production is too inefficient. Continuous spinning requires a spinning reservoir which can be continuously fed and a larger bath to larger samples. Continuous production however has a drawback: instabilities can form in the polymer jet if it undergoes shear forces which are too great. Such shear forces result in shark skinning where the fiber forms rough, undulating features.[86] Further shear stresses cause further destruction of the fiber surface. Before these instabilities occur however, die swelling occurs. Die swelling is where the extruded jet is greater in size than the die it passed through[87]. Even though shark skinning instabilities may be beneficial in some applications, such as in the production of pasta, to create a greater surface area, shear forces need to be minimized in the scaled iRJS to decrease die swelling and avoid these instabilities and large fiber diameters[87]. Finally, in addition to scaling the production of sheets, scaling the production of yarns enables industrial scalability of the system. As a result, we scaled the iRJS systems to make large sheets and to make continuous yarns (Figure 3.0.1).

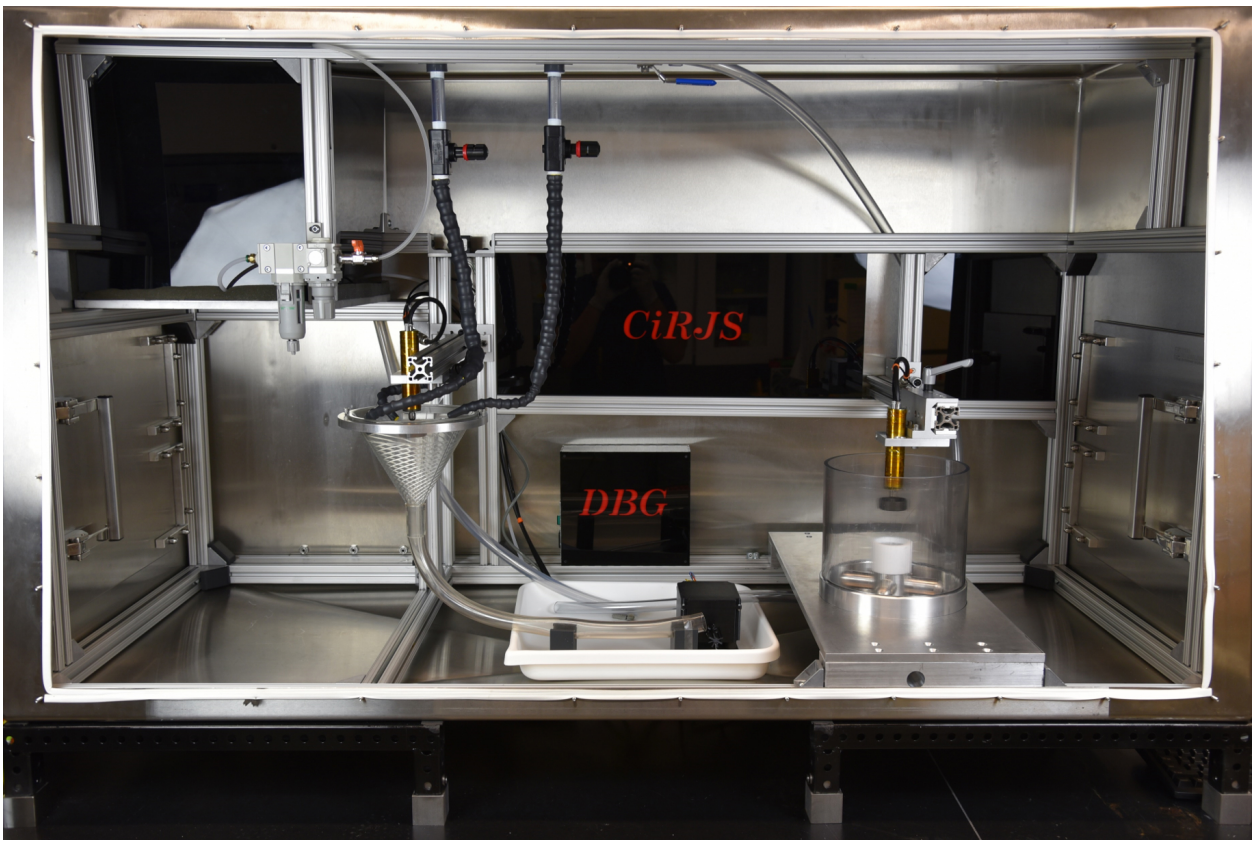

Figure 3.0.1: Scaled iRJS Precipitation Based Nanofiber Platform. To produce larger samples for fragmentation testing and large scale testing of materials, a continuous nanofiber yarn system was built on the left of the glovebox and a non-woven system was built on the right of the glovebox. Both systems required the individual components including continuous, top loading reservoirs and scaled collection schemes.

3.1 Engineering Continuous Loading Reservoir to Enable the Fabrication of Continuous Fibers

To continuously spin fibers, a top loading reservoir with the ability to be continuously feed is critical. However, as the motor that spins the reservoir speeds up to 80k RPM and that the motor is oriented above the reservoir due to the position of the bath, the reservoir needs to be at least double the width of the motor to allow access to a polymer feed. In addition, the reservoir needs a lipped cap to contain the polymer solution to ensure it exits the orifice instead of flying out the top. Increasing the diameter of the reservoir to 30 mm or greater and adding a topped lip adds weight and size. These additions will cause most materials to fail at speeds greater than 30k RPM. Simulation analysis of reservoir design and material selection allows us to build a reservoir with a safety factor of at least 2. For example, making a reservoir out of common milling aluminum (Grade 2011) will fail at 45k RPM. However, a reservoir machined from aluminum grade 7075 allows for the spinning of a reservoir (45 mm in diameter) to speeds of 80k RPM with a safety factor of 5 (Figure 3.1.1).

To protect the 7075 reservoir from slight corrosion, the 7075 reservoirs were coated in an anodized Teflon hard coat with a 25 μm buildup (ASTM B117). This allows for the reservoir to be used with slightly corrosive solutions and to avoid material degradation due to exposure of salts which are usually employed to spin biopolymer fibers (Figure 3.1.2).

AS sulfuric acid eats away at the hard coat, another material is needed to spin PPTA solutions continuously. Materials capable of withstanding sulfuric acid are glass, ceramics, Stainless Steal 316L, and Hastelloy C276[88]. Glass and ceramics were not chosen as any sub-fracture or fault could cause the reservoir to break at high speeds seemingly instantly. As plastic deformation allows for visual inspection and removal of a failing component, the reservoir material was chosen to be metal. As Stainless Steel 316L does not provide corrosion resistance to splashes of sulfuric acid (not full immersion), Hastelloy C276 was chosen. Using the same design as with the previous reservoir, the C276 reservoir was designed with a safety factor of 2 at 45k RPM. Any faster would cause the reservoir to fail and any plastic deformation or 'wobble' in the reservoir means it needs to be replaced before failing catastrophically.

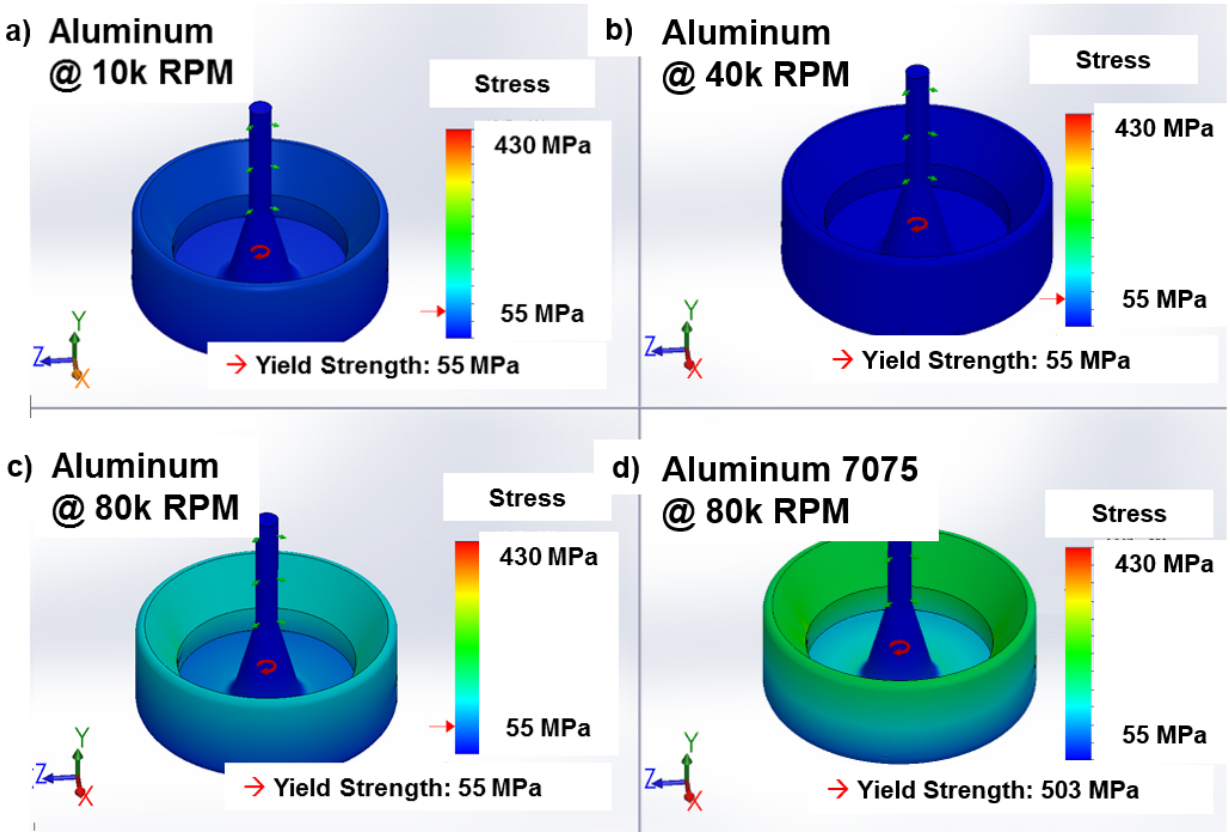

Figure 3.1.1: Simulated Failure Analysis of Reservoir Designs. The finite elemental analysis of Solid Works was utilized to predict the failure of continuous loading reservoirs based on the material choice. For aluminum 2011, the reservoir did not have a predicted stress above its yield stress at a) 10k or b) 40k. At 80k RPM c), however, the reservoir was predicted to yield and fail. A reservoir from aluminum 7075 was predicted to survive speeds up to d) 80k RPM with a safety factor of 2.

(a) **(b)**

Figure 3.1.2: Continuous Loading Reservoirs for Engineering Continuous Fibers. a) Reservoir milled from Al 7075 and hard coated with anodized Teflon was engineered for spinning solutions with slight corrosivity at speeds up to 80k RPM and b) Hasetlloy C276 reservoir was engineered to spin PPTA-sulfuric acid dopes up to speeds of 45k RPM.

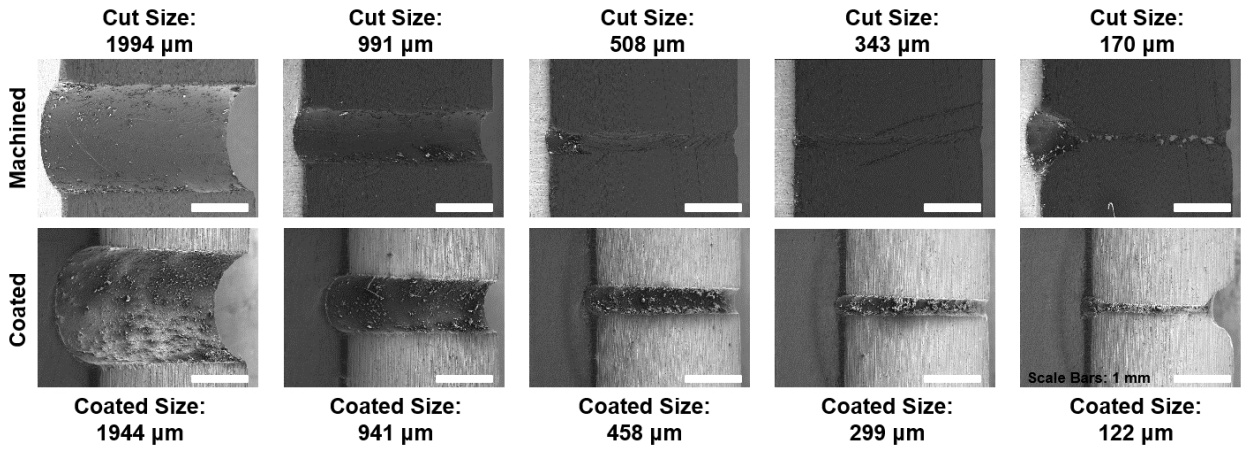

Figure 3.2.1: Reservoir Orifice Sizes. Orifice can be made machined with diameters of 2 mm down to 170μm. Using the anodized Teflon hard coating (ASTM B117) will reduce the orifice size by 50 μm. Coating buildup could be greater to further decrease orifice size. Scale bars = 1 mm. Note: Some orifices were closed by machining debris during the sectioning of these samples.

3.2 Control of Orifice Diameter

To verify the hole size of the orifices, plates with varying hole sizes were manufactured and then sectioned in half to verify the hole ran true through out the 4 mm thickness. For all cuts ranging in size from 2 to .170 μm, the hole sizes were roughly 10% larger than drill bit size. For the small .170 μm orifice, the end of the drilled hole broke, creating a Y shaped defect. Coating the holes decrease the hole size by 50 μm due to the 25 μm buildup on the surface (Figure 3.2.1).

3.3 Limiting Die Swelling on the iRJS

Die swelling is where the jet, after exiting an orifice or die, is greater than the hole size. While Newtonian fluids may have a die swell of 10%, polymer solutions may exhibit a 250% die swelling or greater due to over pressurization.[87] The pressure is created by the polymer chains wanting to relax from the stretched state implied by shear forces. Increasing shear rate while die swelling occurs may lead to fracture instabilities of the jet surface. In addition, die swelling on the scaled version of the iRJS lead to a fiber of the same size even when spun from orifices of smaller size (Figure 3.3.1).

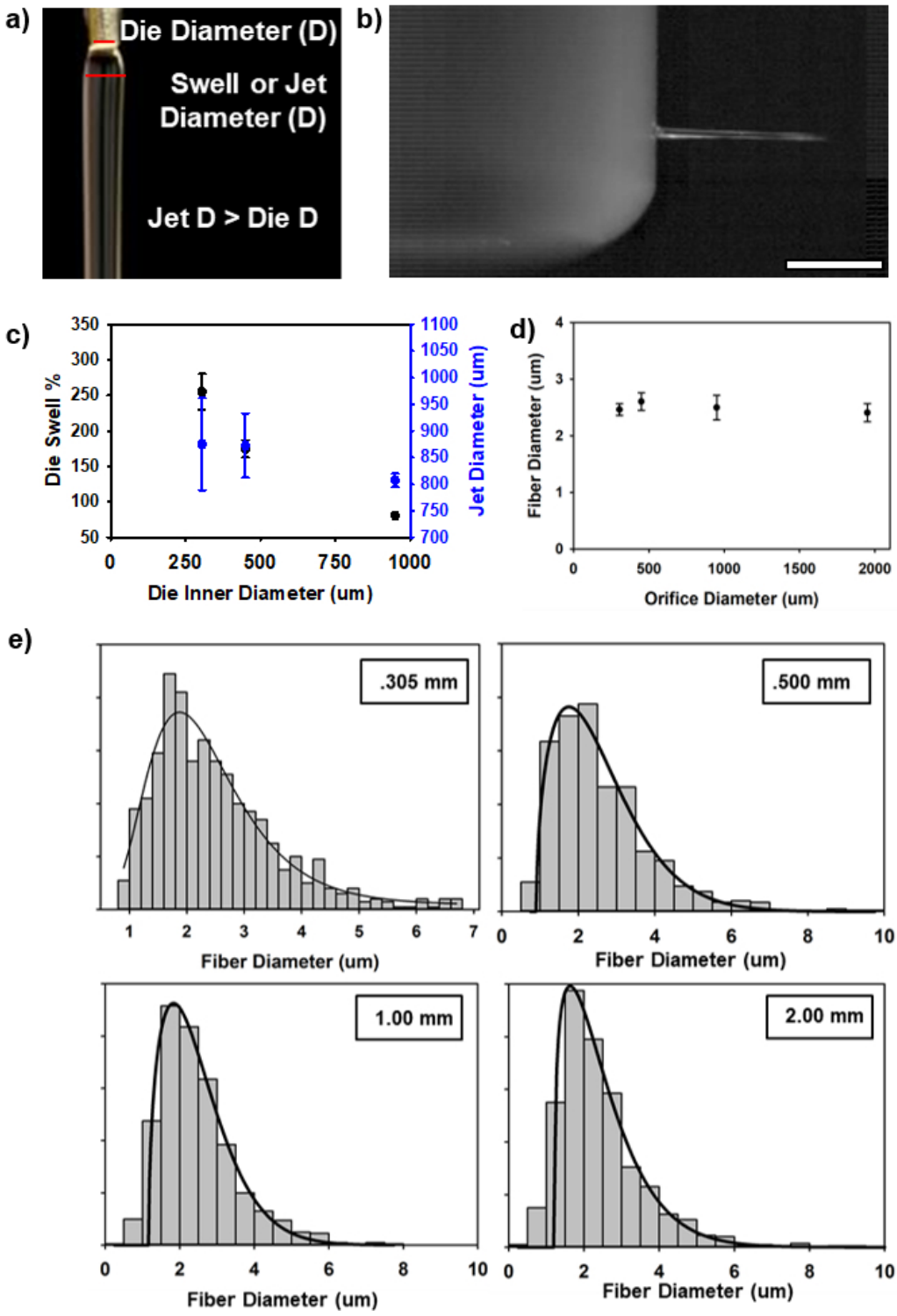

Figure 3.3.1: Die Swelling in the iRJS Negates Decreasing Orifice Size. a) Die swelling is the phenomena where a liquid jet exiting an opening swells to a size greater than the die opening. This phenomena is caused by the tendency of polymers extended underflow to relax into an energy favorable, unextended state. This relaxation causes a normal force generation across the surface of the jet, culminating a pressure that expands the solution. In testing hyaluronic acid-water solutions on the iRJS b), a 3x die swelling was observed for a die size of 305 μm (scale bar = 5 mm). c) Die swelling of these solutions increased with decreasing orifice size. d) This resulted in the average fiber diameter being consistent between fibers manufactured from reservoirs with different orifice sizes. The fiber diameter distributions e) between fibers spun from orifices of .3, .5, 1, and 2 mm were also similar.

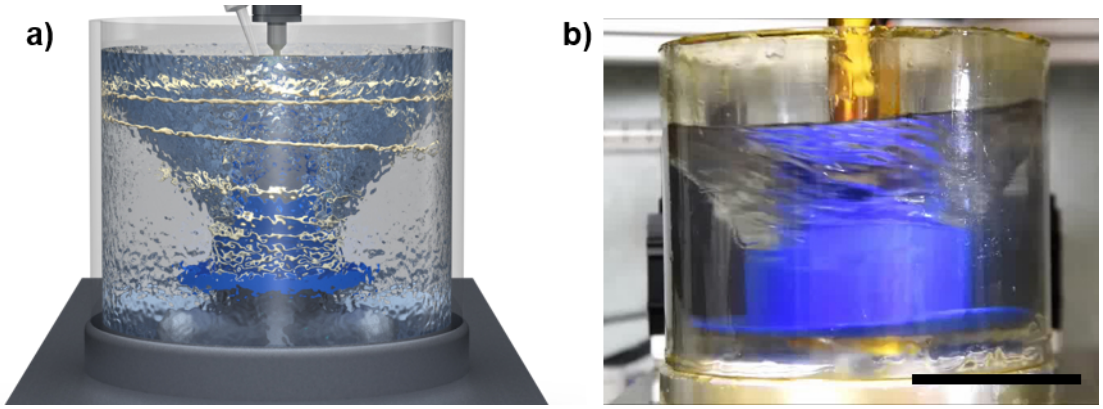

Figure 3.4.1: Scaled iRJS to Produce Continuous Fiber Sheets. a) The design of the scaled iRJS was done in Solid Works and included a top loading reservoir, a rotating collector, a pulley system to rotate the collector, a rotary seal to maintain a water-sight seal, and a continuous feeding polymer syringe. b) the platform was then built and tested to ensure all the components worked together to produce continuous sheets (Scale bar = 10 cm).

3.4 Scaling the iRJS Collection

To enable a motorized collector to control the collector of the scaled iRJS, a PTFE rotary seal was employed to create a leak-tight seal between the rotating shaft of the collector and the stationary plate. The rotary seal design and housing was designed following the Rotary Seal Handbook Guidelines from Parker Hannifin (Figure 3.4.1).

3.5 Scaling the iRJS Yarn Formation

To scale the iRJS yarn capability to produce nanofiber yarns, a funnel system was employed to create the vortex. A PVDF diaphragm pump was selected to recirculate the bath through the the funnel continuously without concern of light corrosive liquids. The iRJS reservoir was placed into the funnel using a linear motor. After spinning, the nanofiber would be wound up by the funnel, directed with the movement of the water to a collector that would spool the yarn (Figure 3.5.1).

3.6 Summary

To make large sheets with fibers running the length of the sample, the iRJS precipitation system needed to be scaled from batch to continuous spinning processes. One of the key components required to make the system continuous was a continuous, top loading reservoir. By making a top loading reservoir, poly-

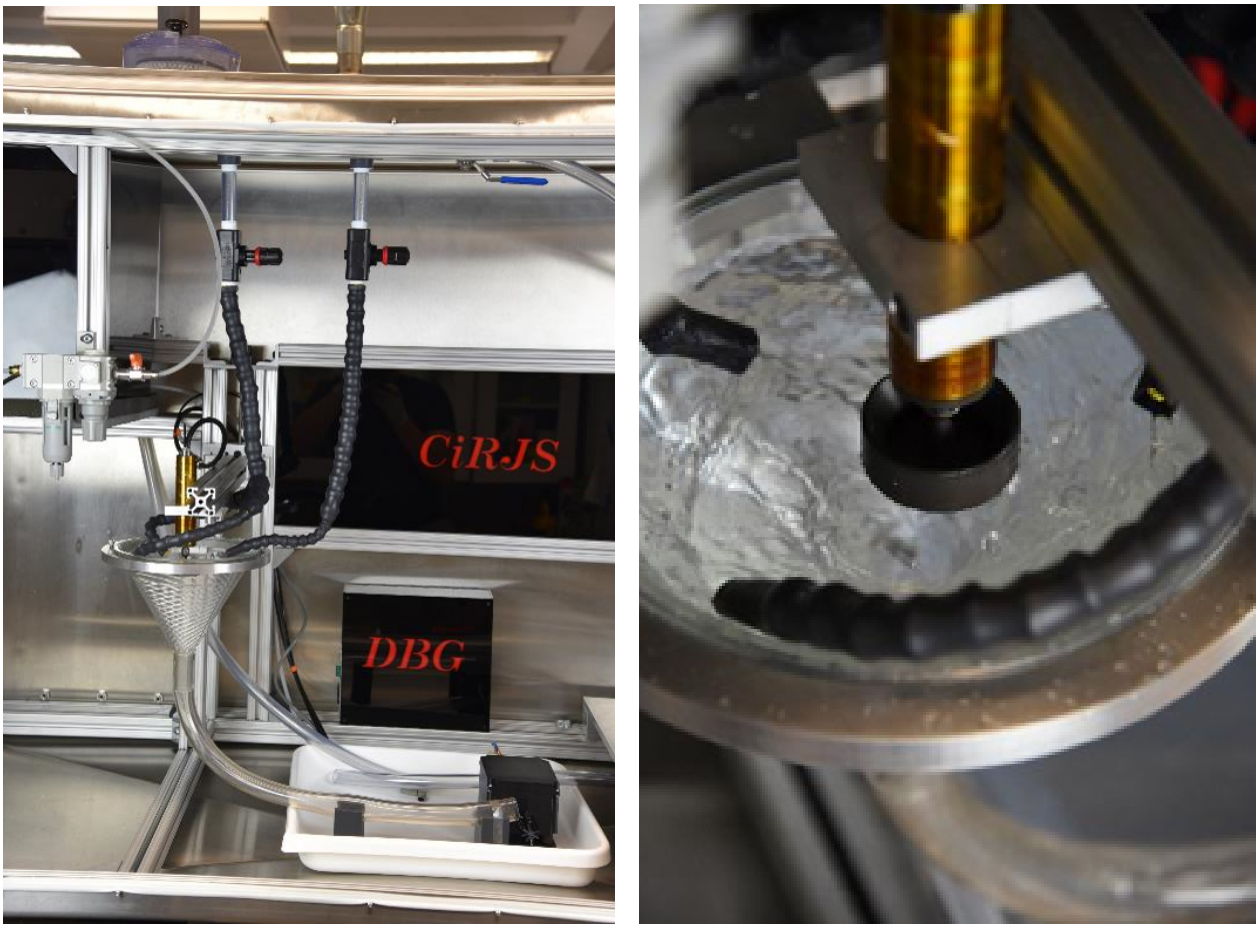

(a) **(b)**

Figure 3.5.1: Continuous iRJS for Yarn Fabrication. a) Using a funnel system allowed for the spinning and collection of yarns on the iRJS. b) Top-view of the funnel vortex that allowed for the fibers to be twisted into yarns.

mer solution can be replenished at the same volumetric flow rate as spinning. As a result, the polymer jet can be continuous leading to fibers spanning the entire length of the sample. In addition, the bath also needs to be scaled in size to allow for the collection of these large samples. To accomplish this scaling, a custom container was made and fitted with an electrical motor via a pulley system to rotate the bath and to collect the fibers. As a whole, this enables the production of large aligned sheets. In addition, continuous yarns were made by replacing the rotating bath with a recirculating funnel bath to allow for the twisting of fibers together into yarns. These two improvements proved the scalability of the iRJS system for fabricating samples for ballistic testing.

Chapter 4

Para-Aramid Nanofiber Sheets: Overcoming the Trade-Off Between Mechanical Performance and Heat Insulation

With the deployment of shrapnel in the 18th century and high explosive ordinances in the 19th century, the mechanism of injury in war has transitioned from primarily gunshot to explosive wounds.[1, 2] While high-performance fibers and ceramic plate armor systems protect the torso of the warfighter from these injuries, the extremities are left unprotected (Figure 4.0.1). Due to this concentration of armor, and the use of improvised explosive devices in unconventional warfare, 80% of American Service Personnel injuries result from explosive and fragmentation mechanisms (Figure 4.0.2). Fragmentation is the process where an explosion throws metal fragments from the site of origin. Since fragments are not aimed at any section of the body, extremity injuries are the most common and 44% of all wartime injuries are classified as severe limb injuries.[2] Materials exist to protect from the average kinetic energy of a fragmentation missile which is lower than the kinetic energy of a 7.62 round. However, the current use of torso fiber-ceramic systems provide this protection at a 20 kg weight cost that would over encumber the warfighter if protecting the entire body. Such a protective system with current materials would prevent warfighter movement entirely. Already, the tactile effectiveness of torso protection, in addition to the 30 kg of gear carried, is questionable due to the mobility constrictions placed on the wearer. Since the warfighter is already burdened by materials that provide protection at a too high cost of weight, any advances in protection should prioritize lightening the material protection already in place.

Fragmentation protection was first possible with the development of the synthetic aramid fiber nylon in

Figure 4.0.1: The warfighter carries 50 kg of equipment including 20 kg of body armor that protects only the torso, leaving the extremities unprotected.

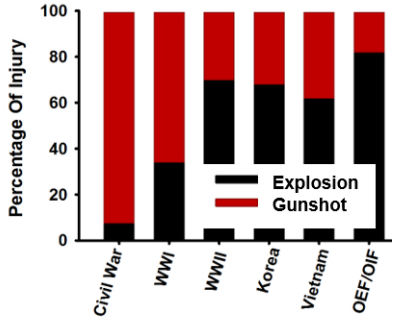

Figure 4.0.2: Starting in World War II, explosions became the primary mechanism of injury replacing gunshots (REF).

the early 20th century.[1] Due to its relatively low protection to weight ratio, it was only deployed on WWII airmen to protect from the flak: fragmentation rounds designed to shred apart airplane hulls. With further advances in nylon development, nylon vests were fielded to US Army personal in the Korean War. With the development of the para-armaid fibers under brand names Kevlar by DuPont and Twaron by Tejin Aramid, fragmentation vests finally protected from hand gun rounds but not rifle rounds. Para-aramid fibers were a revolutionary material development due to the liquid crystal polymer para-phenelyne teraphalamide: the rigid rod polymer enabled it to be oriented and crystallize along the axis of the fiber.[6] Due to this structural advancement, it had higher mechanical properties of any fiber previously spun and higher functional protective performance. With the development of ceramic plates able to stop rifle rounds, the role of fiber protection stopped at providing torso protection against fragments from explosions and the debris generated from a bullet fitting ceramic plates. Research still continues to improve the mechanical properties of fiber to provide greater protection.

The 20 kg torso vest is not the only part of the warfighters 50 kg kit and Kevlar fibers do not only provide mechanical protection.[2] Para-armid staple or non-continuous short fiber pulp has been used to provide heat insulation and recent research on this material in nanofiber form has enabled high insulation sheets with low mechanical properties.[6] This ability to have either high mechanical properties or high thermal insulation is uncommon as classes of materials usually trade-off between heat insulation and high mechanics.[89] The ability to have both high mechanical properties and high thermal insulation simultaneously is rare. In addition to Kevlar having many potential benefits, the warfighter carries more than a Kevlar vest for fragmentation protection. For example, the Universal Combat Uniform provides heat protection. Instead of attempting to improve the mechanical performance of Kevlar fibers to provide better protection for its weight, we attempt to improve a material to overcome the trade-off between heat-mechanical protection for the Universal Combat Uniform that can provide both heat and fragmentation protection. Since staple fibers and porous nanofibrillar networks provide heat protection but no mechanical protection and high performance fiber weaves provide fragmentation protection but low insulation, we hypothesized making continuous nanofibers into an aligned, porous sheet would provide low fragmentation and high heat protection for the warfighter. To make these fiber sheets, we utilized the recently developed immersion Rotary Jet-Spinning(iRJS) system to spin PPTA aramid nanofiber sheets.

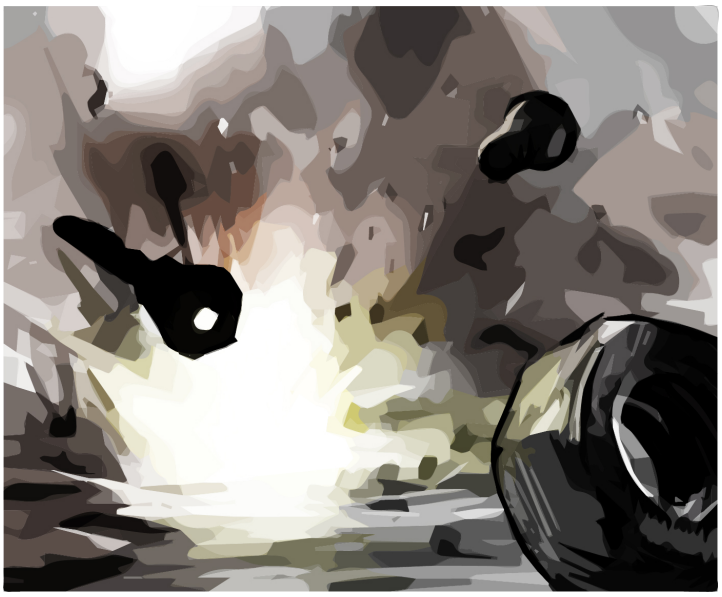

Figure 4.1.1: An explosion from an improvised explosive device (IED) generates fragmentation, shrapnel, and heat.

4.1 Rationale for Para-Aramid Nanofibers Material Selection

The warfighter needs protection for their extremities against explosions and fragmentation (Figure 4.1.1). A material's ability to stop a fragmentation projectile is its V_{50} rating or the velocity at which a missile breaks a materials 50% of the time. This functional protection measurement is proportional to fiber material properties: Young's Modulus (E), elongation to break (ε), strength (σ), and density (ρ)[90]:

$$V_{50} = \left(\frac{\sigma \varepsilon}{2\rho} \sqrt{\frac{E}{\rho}} \right)^{\frac{1}{3}}$$

On the other hand, thermal insulation R is the inverse of the fundamental material property heat conductivity k multiplied by the materials length[91]:

$$R = \frac{L}{k}$$

A material's ability to stop a fragmentation projectile is its V_{50} rating or the velocity at which a missile breaks a materials 50% of the time.

Plotting material Young's Modulus against its heat conductivity (Figure 4.1.2), we see that materials generally simultaneously gain increases to thermal conductivity and modulus; therefore, materials trade-off be-

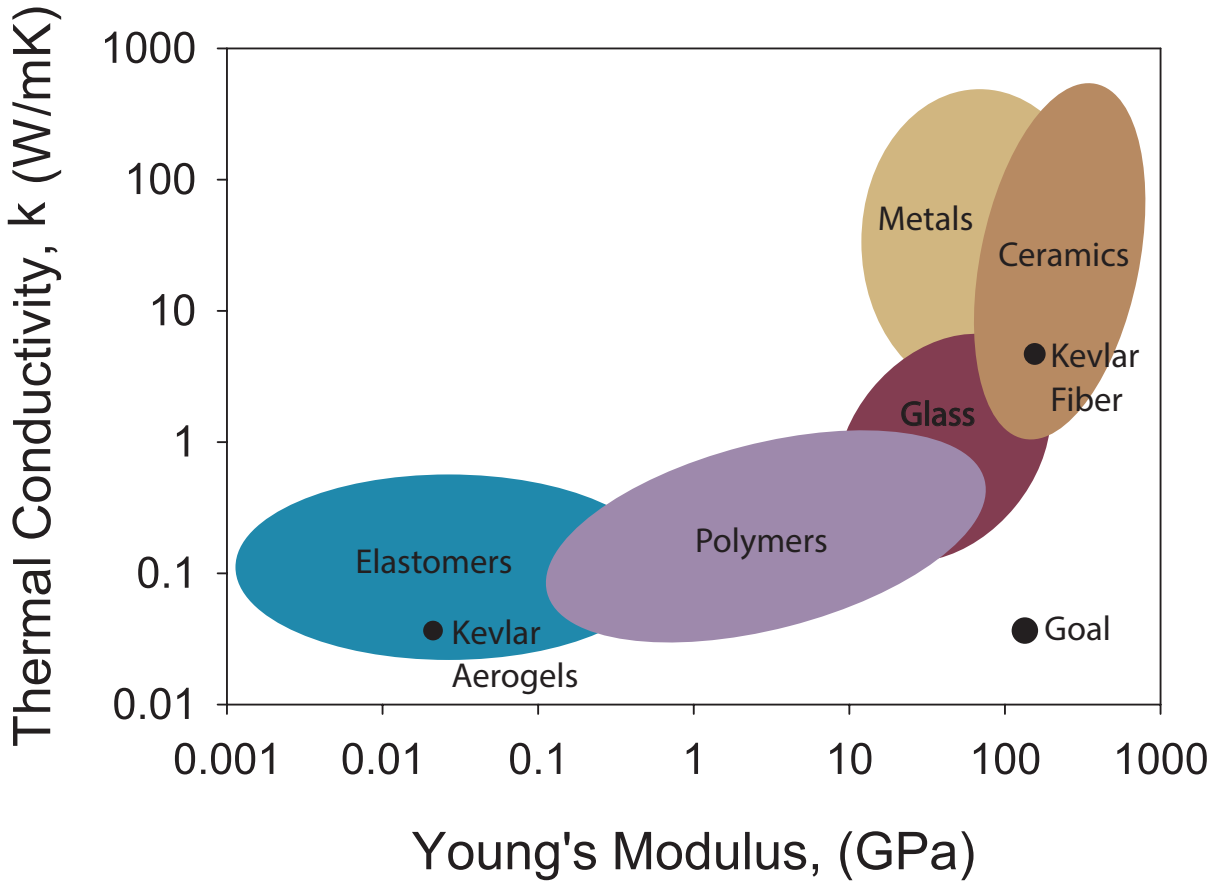

Figure 4.1.2: Due to the structure function relationships, material families trade-off between low thermal conductivity and high Young's modulus. Kevlar, depending on its structure, is unique in that it is a polymer fiber that can have one of these properties at a time. We aim to combine Kevlar aerogel and fiber structures to attain dual functionality.

tween thermal insulation and modulus. Generally, an increase in mechanical modulus and strength comes with a loss in elongation to break: strong materials are generally crystalline (metals, ceramics, high performance polymers) and break by elastic rupture while materials with a high elongation to break are amorphous (polymers) and fail by plastic deformation. The crystallinity of the material also increases thermal conduction. Due to the organized structure, heat transfer which is conducted through phonon crystal lattice vibrations, is directed along the axis of the fiber. In an unorganized amorphous material, heat transfer is a random walk and therefore slower. Bulk, homogeneous materials trade-off between these properties due to a fundamental difference in structure[91].

While most materials are limited to one of these extremes, PPTA can be processed into crystalline Kevlar

fibers or be made into amorphous, nanofibril aerogel.[89, 91] The Kevlar fibers are continuous (aspect ratio > 1000) and woven together with no spacing. On the other structural extreme, aerogels are comprised of fibrills or small fibers (aspect ratio < 100) chemically fused together to form a network of trapped pores. To overcome the trade-off of choosing one of these structure-function relations, we hypothesized an aligned continuous nonwoven of PPTA nanofibers would allow for the fiber to bear the mechanical load and the porosity to limit heat diffusion (Figure 4.1.3). To fabricate the nanofiber sheets we chose to use the immersion Rotary Jet Spinning (iRJS) platform to fabricate the PPTA nanofibers[46]. It relies on the spinning of a reservoir at speeds greater than 1k RPM and centrifugal forces to extrude out polymer solution. Once in an air gap, the jet thins out before hitting a precipitating bath where diffusion will drive the sulfuric acid from the jet into the water bath. The bath itself is a vortex formed from a rotating collector at 300 RPM; the collector pulls the fibers along the streamlines of the vortex onto a collector. During spinning, the fibers interconnect to make a network. After spinning, freeze drying preserves that network, replacing water with air.

4.2 Selecting Dopes with Appropriate Viscoelastic Properties

To ultimately test the materials performance in fragmentation and heat protection, fragmentation testing and heat testing were performed. Fragmentation or ballistic testing requires sheets of a 10 cm by 10 cm minimal size. While the iRJS has been shown to be capable of making PPTA nanofiber sheets, the sizes of sheets were limited to 1 cm by 5 cm. To be able to fabricate sheets of this size, an understanding of the viscoelastic properties of the PPTA-sulfuric acid dope during spinning was critical. During extrusion from the orifice, the solution needs to thin into a jet and therefore be viscous dominant. During collection, the dope needs to be elastic dominant to ensure the jet does not deform before solidifying. To measure these properties, we assumed an oscillatory rheometer probing the material at the a time scale relevant to spinning (5k RPM $\approx$ 83 Hz) and collection (300 RPM $\approx$ 5 Hz) would directly apply to forces on the material during spinning. When the tangent of delta or ratio of viscosity to elasticity is greater than 1, then the material is viscous dominant. Testing revealed low concentration dopes (.5%, 1%, 2%) to have the opposite properties during spinning collected than what was needed (Figure 4.2.1). During spinning they

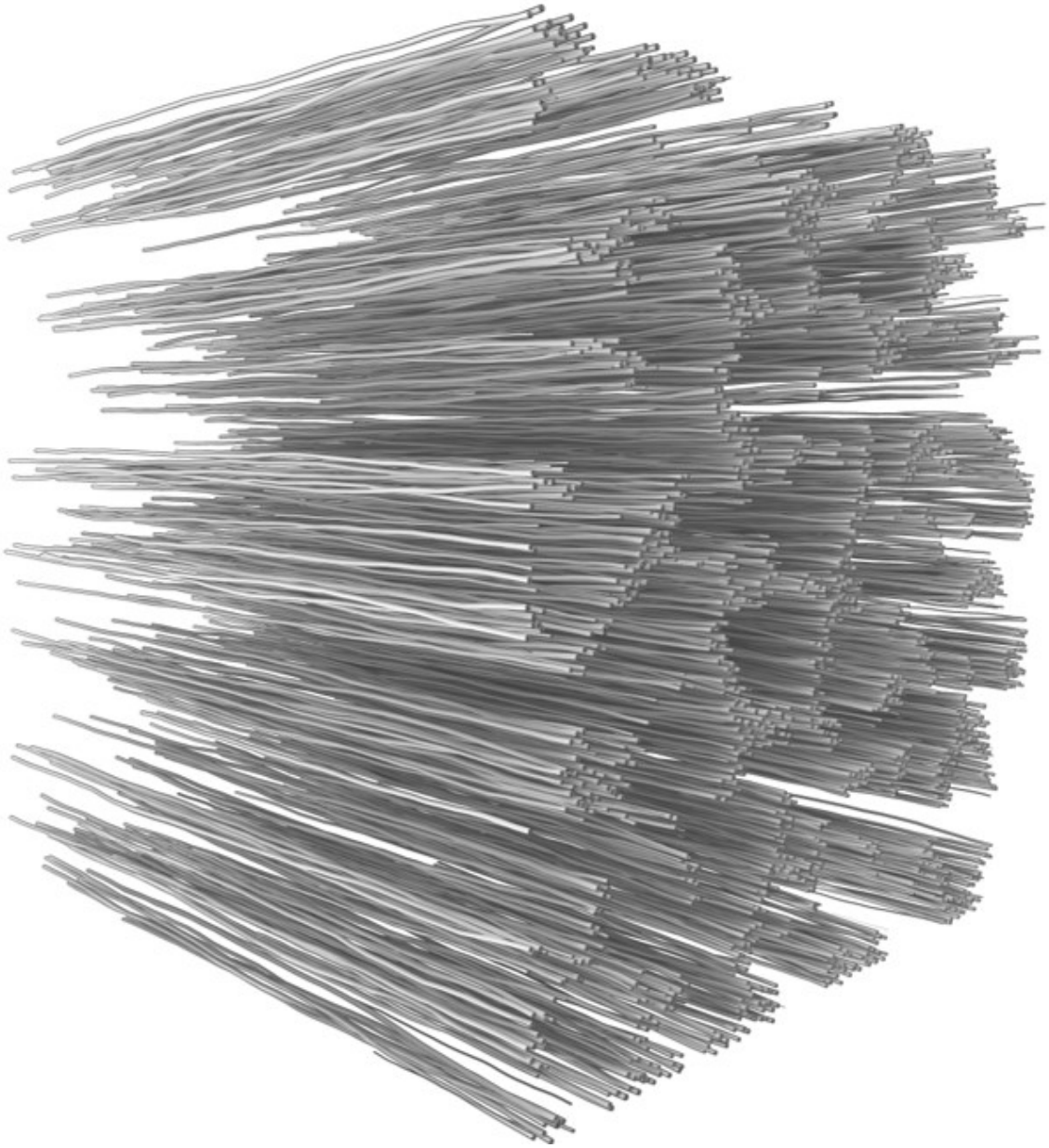

Figure 4.1.3: An artistic schematic representing a porous sheet constructed from aligned nanofibers. The nanofiber will provider mechanical protection by bearing applied load along the length of the fibers while the porosity will limit heat diffusion, enabling thermal insulation.

were elastic dominant and during collecting they were viscous dominant. This is because the characteristic time scale (or where the material transitions from being viscous to elastic dominant) of the .5% dope was at 60 and 80 Hz. Generally, at faster time scales, a polymer solution becomes more elastic dominant because the polymer chains do not have time to relax, a characteristically viscous effect.

Therefore, we wanted to make stable jet spinning conditions for spinning to ensure stable continuous production of long nanofibers. During jet initiation and jet spinning, a solution needs to be viscous dominant to ensure a continuous jet. If the solution was elastic, it would bead instead of thinning leading to short fibrils. Furthermore, the solution being ejected into the reservoir would bead and not enter the orifice to allow for jet initiation. Changes in temperature influence the viscoelastic properties of materials: an increase in temperature increases the movement of polymer chains allowing for an increase in viscosity while a decrease in temperature limits their movement causing a shift to elastic dominance. At 83 HZ frequency relevant to spinning, the material needs to be elastic-dominant. Increasing temperature from -10 C to 80 C showed an increase in tan(delta) for 1% and 2% solutions. However, only the 1% became viscous dominant and this occurred when the at 18 C or greater. Important to note is that the .5% solution does not follow the trend of the other solutions. This is because PPTA-dopes have different solution packing and the .5% solution has a different packing structure. To further ensure the jet turns into a fiber, it needs to be elastic-dominant after jet thinning and when entering the bath. More specifically, the jet in the bath needs to have a characteristic time scale that is longer than the time scale of diffusion of the sulfuric acid from the jet. As diffusion will be dependent on the ultimate size of the fibers, we assumed an elastic-dominant material during collection will always enable the timescale to be greater than the time scale of the material and therefore greater than time scale of diffusion. Only the 2% solution became elastic-dominant and this occurred at 2 C. However, as the solution was elastic-dominant during spinning, it was not a suitable material to choose for spinning. As a result, we selected the 1% solution which had a 2:1 ratio of its elasticity to viscosity and

Figure 4.2.1 ***(following page)***: Selecting precursor viscoelastic material properties allows for the production of sheets for ballistic testing: spinning requires the solution to be viscous while collecting requires the solution to be elastic. However, the PPTA-sulfuric acid dopes are a) elastic at the timescale of spinning and viscous at the time scale of collecting. b) Solutions become more elastic as they are strained past 50%. Temperature ramps revealed the ratio of elasticity-viscosity at time scales of c) the reservoir and d) the collector. e) Flow curves of the solutions reveal the shear thinning solutions of the properties and the f) normal force generation. Balancing these properties enabled the fabrication of g) continuous nanofiber sheets with h) 1.2 μm median fiber diameter.

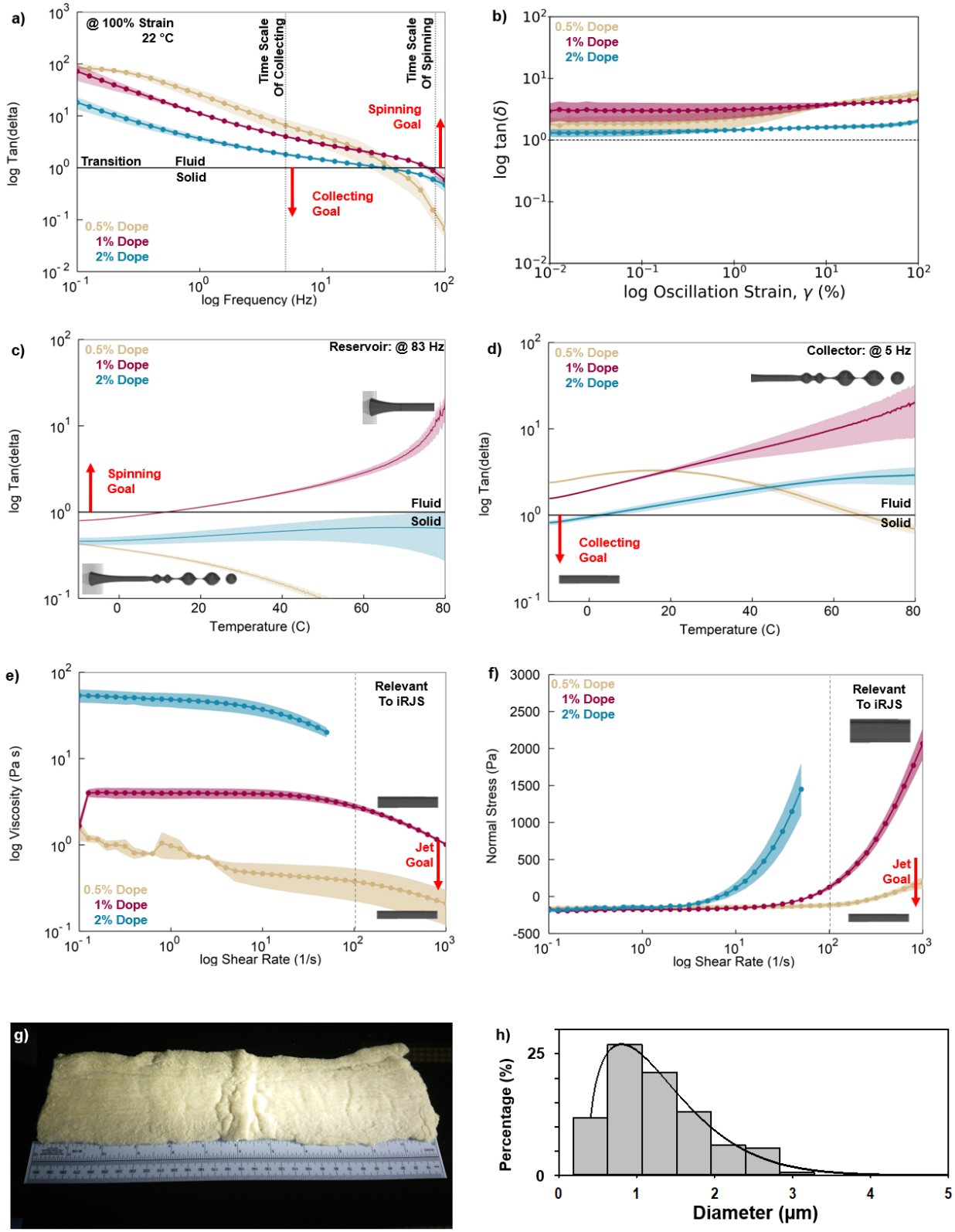
a)
@ 100% Strain
22 °C
Time Scale Of Collecting
Time Scale Of Spinning
Spinning Goal
Collecting Goal
Transition
Fluid
Solid
0.5% Dope
1% Dope
2% Dope
log Tan(delta)
log Frequency (Hz)
b)
0.5% Dope
1% Dope
2% Dope
log tan(δ)
log Oscillation Strain, γ (%)
c)
Reservoir: @ 83 Hz
0.5% Dope
1% Dope
2% Dope
Spinning Goal
Fluid
Solid
log Tan(delta)
Temperature (C)
d)
Collector: @ 5 Hz
0.5% Dope
1% Dope
2% Dope
Collecting Goal
Fluid
Solid
log Tan(delta)
Temperature (C)
e)
Relevant To iRJS
Jet Goal
0.5% Dope
1% Dope
2% Dope
log Viscosity (Pa s)
log Shear Rate (1/s)
f)
Relevant To iRJS
0.5% Dope
1% Dope
2% Dope
Jet Goal
Normal Stress (Pa)
log Shear Rate (1/s)
g)
h)
Percentage (%)
Diameter (μm)

assumed the material would solidify before deforming as the solution would be elastic enough to ensure diffusion of the acid before jet beading.

Along with ensuring that the jet is stable during spinning and collection, we need to ensure that the jet is shear-thinning and exits the orifice with the smallest possible diameter to enable small fibers. A viscosity decrease of the dope with increasing shear force ensures that the solution is shear thinning and able to thin into a jet during spinning. Shear rates relevant to the iRJS are greater than 100 1/s. At these shear rates, the .5% and 1% solutions undergo shear thinning. The 2% solution beaded and was not stable under rheological testing. Along with the fact that the 2% solution was not viable candidate for testing during the previous test, it failed this test as well. To ensure the solution had minimal jet size after exiting the orifice, the jet needs to have a minimal normal force during spinning. A normal generation leads to die swelling: where the jet of a solution exiting an orifice swells to a size greater than the orifice. The normal force generation across the surfaces adds a pressure that is released when the solution leaves the orifice. While Newtonian solutions have 10% die swelling at high shear rates, viscoelastic polymer dopes may have die swelling higher than 300% and and as low as 70%. A high positive normal force generation leads to a high die swelling ratio while a negative normal force leads to a low die swelling ratio. So while increasing the spinning speed will increase the shear rate and decrease jet size during jet thinning, growth in shear rate grows normal force generation. To avoid excess die swelling, 5k RPM was chosen to accelerate with a shear rate of 500 1/s to thin our 1% solution into thin jets.

From the rheological data, the 1% solution was chosen to be spun from the reservoir at room temperatures into a 1C water bath. To make the 5g sheets needed for testing, 500 grams of 1% solution was spun into the bath while 1 L of 10N NaOH was extruded into the bath at a rate to counteract the pH drop from the acid addition. After spinning, the sheets were pulled from the collector and transferred to a water bath which allowed any acid to diffuse out of the fiber sheets. After repeating this step, the sheets were frozen to -80C over night and then placed in a freeze dryer for three days to ensure that the water sublimed. If dried in ambient condition, the evaporation of water would cause the fibers to collapse due to surface tension of the remaining liquid. As a result, we were able to produce fiber sheets with fiber median diameter of 1.2 μm and a density of .1 g/cm^3. Compared to commercial fiber with a density of 1.4 g/cm^3 and 8 μm fiber size, we saw our fibers sheets have a greater porosity due to the lower density.

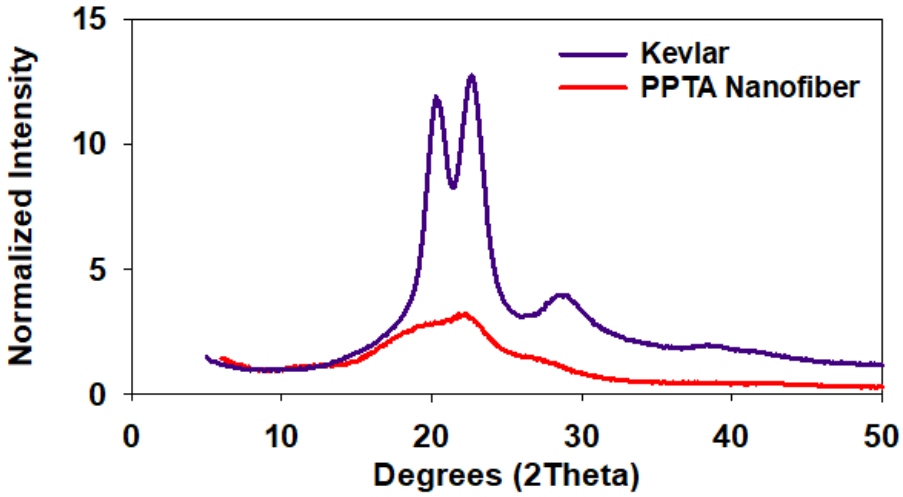

Figure 4.3.1: X-ray diffraction of the PPTA nanofiber sheets vs. commercial Kevlar fibers.

4.3 Structure and Mechanical Performance of Single Fibers

As amorphous and crystalline structures affect both mechanics and heat diffusion, we used x-ray diffraction to quantify their crystalline-amorphous ratio. X-ray diffraction revealed the 3 crystalline peaks at 19, 22, and 28 contributed to Kevlar fiber high mechanical properties. Examining the area of crystalline to amorphous peaks, the Kevlar was determined to have a crystallinity of 80%, agreeing with published values. The manufactured PPTA nanofibers showed significantly lower signal (Figure 4.3.1). As amorphous content does not provide x-ray signal as compared to crystalline samples, the lower signal was attributed to being primarily amorphous. Calculating the amorphous peaks, the nanofibers were determined to have 10% crystallinity. The nanofiber structure was more closely related to a cast film. With this structure, the nanofiber will have a slower timescale of heat diffusion through the fiber due to its random directionality unlike the crystalline Kevlar and therefore limit heat conductivity.

In addition to lowering heat conduction, the amorphous content of the fiber increases elongation to break while lowering the strength and modulus of the nanofiber compared to the commercial fiber. Using uni-axial tensile testing following ASTM D3822M-14, the changes of the mechanical properties of the laboratory fibers was determined to follow the structural changes (Figure 4.3.2). The modulus of the commercial fibers were 360x greater and its strength 10x greater. However, due to the amorphous content, the laboratory fibers had a 4X greater elongation to break. Following the relation between V_{50} and fiber me-

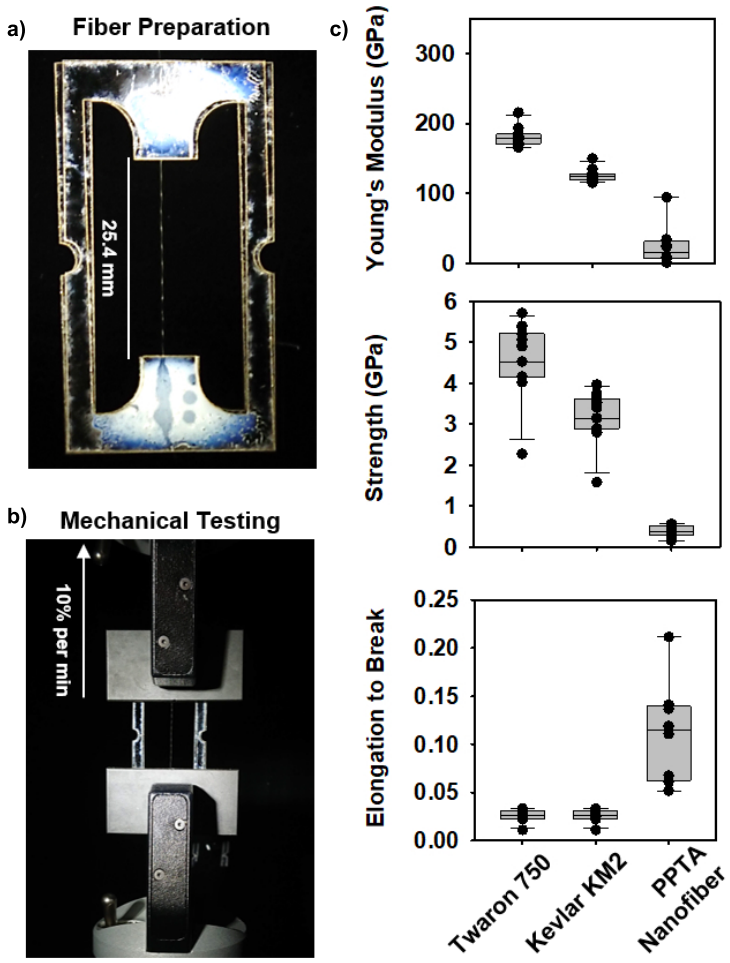

Figure 4.3.2: Mechanics of produced PPTA nanofibers were determined by uni-axial tensile testing. a) A fiber was attached to frames to enable loading into the tester and, after the frame was cut, the fiber was pulled to failure to determine the c) modulus, strength, and elongation to break.

chanical properties, the ballistic performance of the Twaron fibers was determined to be only 2.76 times greater than the nanofibers. This is the same predicted ballistic performance provided by ballistic nylon. As a result, the fiber sheets would provide similar fragmentation protection while increasing heat protection; the fibers would only sacrifice protection to small arms fire. Furthermore, the V_{50} analysis provided does not take into account how low melting point fibers melt during a ballistic impact. Therefore, we expect our fibers to perform better than ballistic nylon but poorer than commercial para-armid fiber weaves.

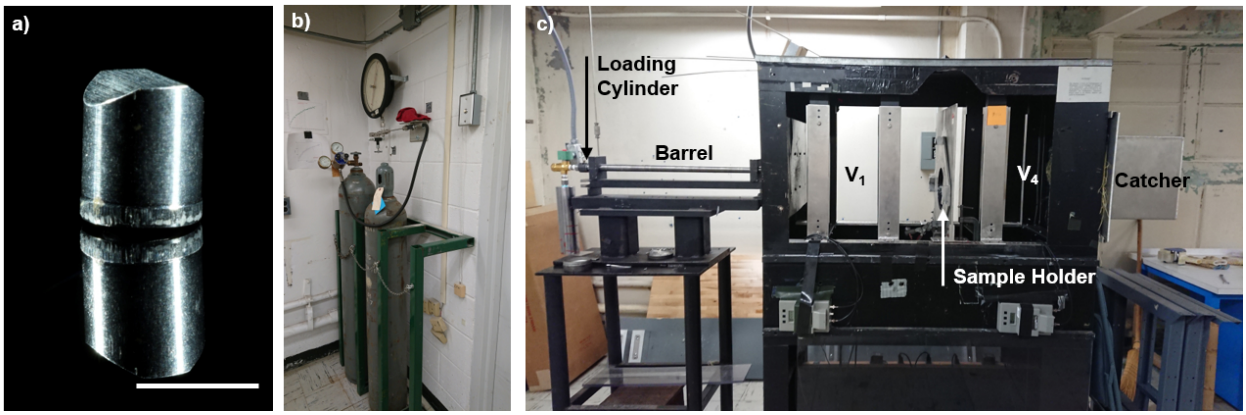

Figure 4.4.1: Set-Up for Fragmentation Testing. a) A fragment simulating projectile (scale bar = 5.45 mm) was accelerated b) by pressurized air through a c) testing range toward the sample. The velocity of the bullet was calculated using light gates at V_1 and V_4. V_1 was used to calculate the striking velocity and V_4 was used to calculate the residual velocity.

4.4 Ballistic Performance and Heat Insulation of Nanofiber Sheets

To verify the prediction of the mechanical testing, V_{50} testing was performed to quantify the fragmentation protection of the sheets. To test the V_{50} rating following the Combat Capability Soldier Center Protocols, a 1.1 g fragment-simulating projectile was accelerated towards the tested material using a controlled air pressure source (Figure 4.4.1). The effectiveness of the material's protection was determined by measuring the striking and residual velocity of the projectile before and after hitting the material. A registered residual velocity means a complete penetration for that striking velocity while a reading of no residual velocity means the fragment was completely stopped by the material or had too low a velocity to register. Visual inspection was used to verify if the fragment was completely stopped or was a partial penetration. To calculate one V_{50} data point, the four lowest velocities causing complete or partial were averaged with the four highest velocities leading to a complete stop. To fairly compare the unidirectionality of our sheets versus the bidirectionality of the control commercial fiber weaves, the nanofiber sheets were sandwiched between two Twaron 750D textile weaves. In addition to providing a fairer comparison, this material sandwich would more likely mimic a final product as a non-woven fibers are only used as insulation and not structure for clothing. To test if our fibers provided ballistic protection, nanofiber sheets were layered in 1, 2, or 3 layers between the woven textiles (Figure 4.4.2). Increasing the amount of nanofiber sheets increased the ballistic performance of the construct at a rate lower than using pure commercial fiber weaves (Figure 4.4.3).

Non-woven ballistic protection can be provided by either 1) increasing the effective area of the bullet

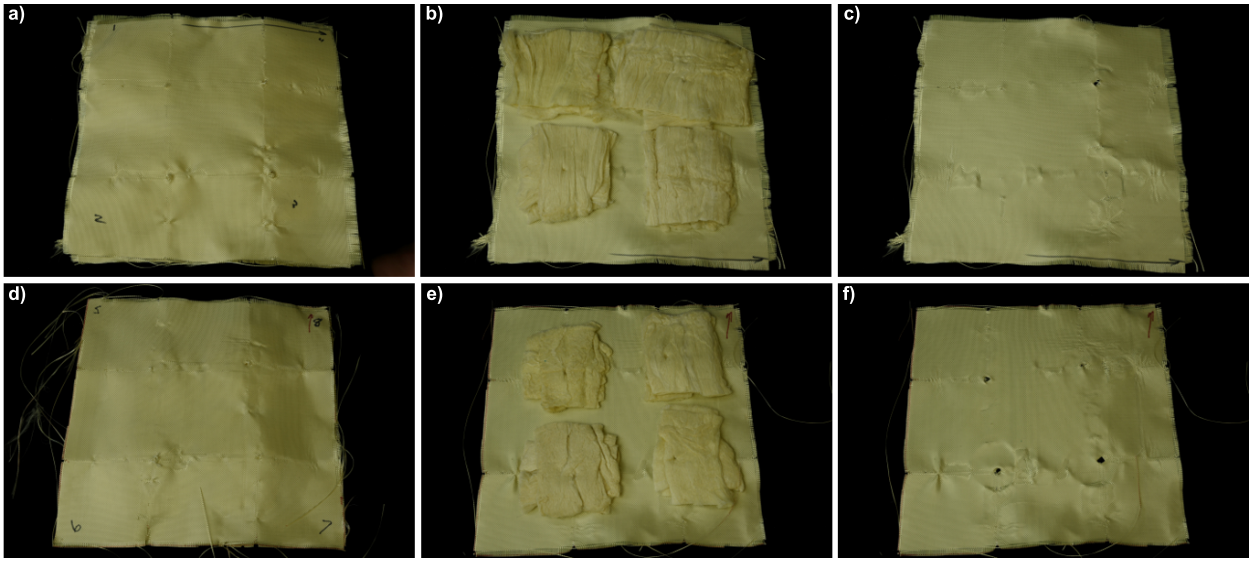

Figure 4.4.2: Example of Fiber Sandwich After Fragmentation Testing. Two samples of a,d) Twaron-b,e) Nanofiber-c,f) Twaron sandwiches shown to see the bullet impact on the a,d) top layers, b,e) the middle layer, and c,f) bottom layer.

by projecting a greater area to subsequent layers or 2) by acting as a mechanism for energy absorption. The effect of presenting greater projectile area is greatest when the fibers are placed in the front and energy absorption is most prominent when the fibers are placed in the rear of the construct. Testing the sheets in each of these configurations had too little a difference to conclude by what mechanism the nanofiber sheets provided protection. Furthermore, the PPTA nanofiber sheets had a V_{50} rating of 600 ft/s, 100 ft/s lower than having a only pure commercial fiber weaves.

However, the low trade-off in V_{50} protection allowed for improved heat insulation (Figure 4.4.4). To measure the heat insulation, we used a 600W heat source and probes to measure the temperature on both sides of one layer of the nanofiber sheet and control. Upon heating, the nanofiber sheets heated slower than the commercial fibers. Using this set-up, the heat conductivity k was determined by:

$$k = \frac{QL}{A\Delta T}$$

The heat conductivity for the nanofiber sheets was $1.76 \pm .59 \frac{W}{mK}$ while the commercial Twaron weaves were $3.85 \pm .32 \frac{W}{mK}$. as the nanofibers created using the methods described above are less dense and thicker, this lead to an insulation value, R, 20x higher than the commercial fibers as defined by $R = \frac{L}{k}$.

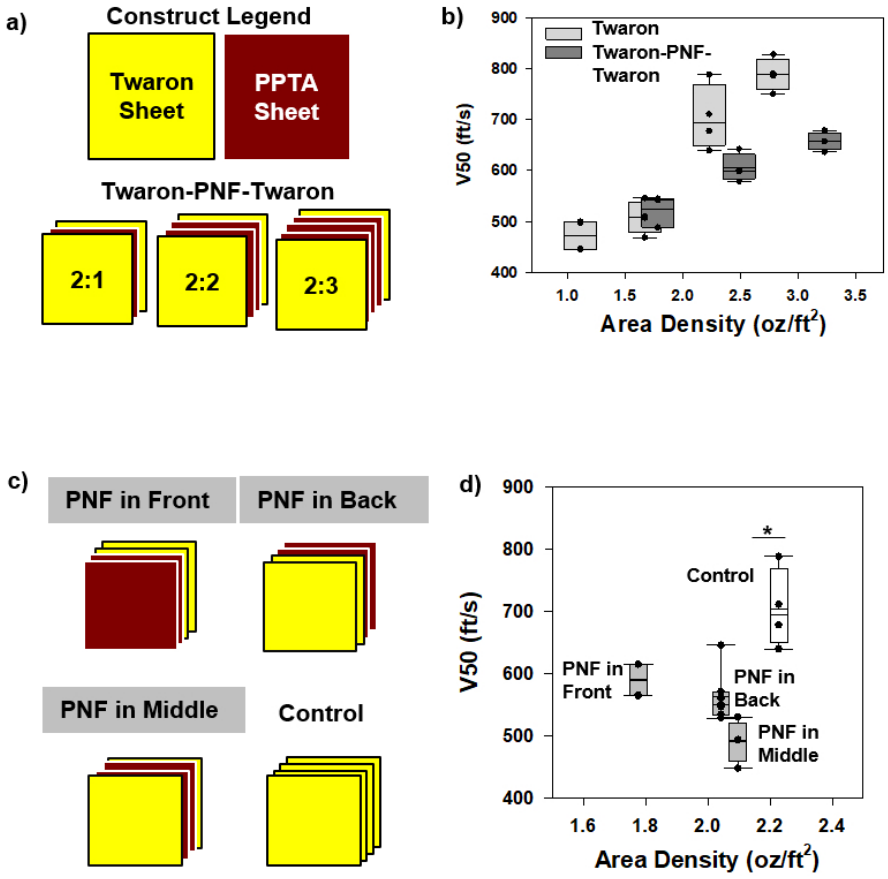

Figure 4.4.3: Fragmentation Performance of Produced Nanofiber Sheets. a) Samples of Twaron Stacks as a control and Twaron-Nanofiber-Twaron sandwiches were tested to see if the nanofibers provided b) ballistic protection. c) The placement of the nanofiber layer wast altered to determine it affect on d) ballistic rating.

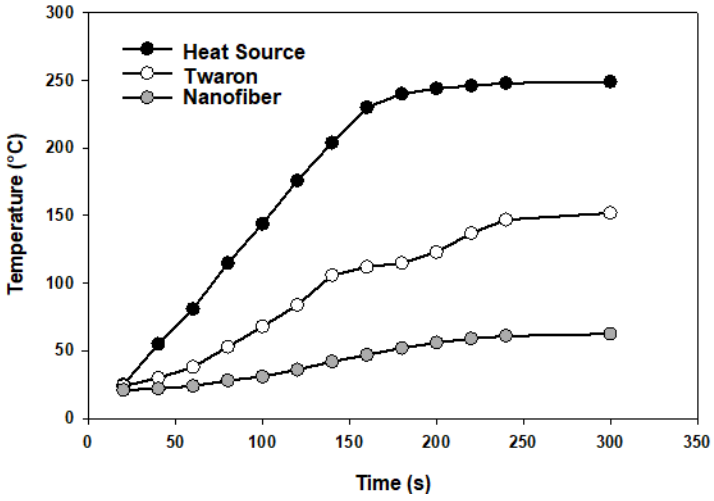

Figure 4.4.4: The rate of heating at the heat source and on the opposite side of the Twaron or nanofiber sample compared the heat transfer properties of the two materials.

4.5 Summary

By combining the structure of commercial continuous fibers with the porosity of aeorgels, para-aramid nanofiber sheets were prepared to overcome the trade-off between mechanical protection and heat insulation. Eventually this methodology may lead to creating combat uniforms that provide protection against the environment as well as protection against explosive fragmentation.

4.6 Experimental Design

Solution Preparation: PPTA-H2SO4 solutions were prepared in a 500 ml reaction vessel under nitrogen and heated at 85 C. The solute and solvent were mechanically stirred with an overhead stirrer and a PTFE coated anchor impeller at 300 RPM for 90 minutes to ensure complete dissolution. The solution was then stirred at 10 RPM for 30 minutes to degas the nitrogen from the dope.

Spinning Fibers: Fibers were fabricated using immersion-Rotary Jet Spinning (iRJS). 300 ml of polymer dope was extruded from a Nordson EFD syringe system (EFD 7012436) and 22 Gauge Tapered Tip (EFD 7018298) at 20 PSI into the iRJS reservoir spinning at 5k RPM. The centrifugal force of the reservoir extruded the solution through two 1 mm orifices, through an air gap, and into a 2 C water precipitating bath. To neutralize the added acid during spinning, a molar equivalent of 10 N Sodium Hydroxide (VWR BDH7247-4) was extruded through a syringe (EFD 7013899) at 5 PSI. After the completion of fiber spinning, the fiber sheet was placed in a wash bath for 30 minutes. Sodium hydroxide was then added until all residual acid was neutralized. The fibers were then placed in a secondary wash bath for two hours. To dry the sheet, the fibers were frozen at -80 C for 12 hours and then placed in a freeze dryer for 48 hours. The motor for the iRJS was a Nakanishi E3000 Motor (NR-3080S Spindle, EM-3080J Brushless motor, E3000 Controller, AL-C1204 Airline Kit) with a speed range from 1k to 80k RPM in 1 RPM increments. The reservoir (45.4 mm diameter and two 1 mm diameter orifices) was machined from Hastelloy C276 to resist corrosion form sulfuric acid.

Scanning electron Microscopy (SEM) SEM images were attained using the Harvard Center of Nanoscale Systems' Zeizz Supra FESEM. Images were gathered using a 5 kV electron source.

X-ray Diffraction: X-ray diffraction patterns were collected using Harvard University's Department of Chemistry and Chemical Biology X-ray Laboratory's Bruker D2 phaser over a 2θ rage of 5-90° with a scan speed of 3° min-1 and increment of 0.02°.

Rheological Testing: Rheological properties of PPTA-H_2SO_4 solutions were determined using a TA Instruments Discovery Hybrid 3 Rheometer with a cone plate geometry. The cone had a 40 mm diameter, 1.988° angle, and 40 μm truncation gap. A solvent trap was employed to reduce solvent loss during testing. Due to the corrosive properties of sulfuric acid, all materials in contact with the sample were Hastelloy C276. To load the sample, the cone was brought to a height above the plate defined by the truncation gap. After trimming the sample, the cone was raised and then brought back to the truncation gap, reducing normal force generated during loading. After loading, a 300s soak time ensured the sample reached equilibrium. Steady state sensing was employed over 300s of testing to ensure the sample reached equilibrium before data was recorded. If subsequent 30 second sample periods were with 5% tolerance of one another, then the sample was determined to have reached steady state and the next point was sampled.

Temperature dependent properties at 5 Hz, 83.3 Hz, 1% strain, were probed using a temperature ramp from -10 to 90 °C at a rate of 2.5 C per min. Changes in truncation gap distance due to thermal expansion was calibrated before testing. Flow dependent properties, was determined over a shear rate of .1 to 1000 1/s at 22 C sampled at 10 points per decade. Strain dependent properties were determined over a strain of 10-2 to 102 % sampled at 10 points per decade at 22 C and at both 83 and 5 Hz.

Fiber Tensile Testing: Following ASTM D3822/3822-14, the two ends of a single fiber were adhered to a 150- μm thick polycarbonate frame (fabricated on a UV laser cutter) using Loctite 770 Primer and Loctite 401 Adhesive. After curing for 12 hours, the frame was placed into the pneumatic grips of an Instron 5566. Before testing, the frame was cut to allow testing of the fiber only. The fiber was then pulled at a constant strain rate of 10% per min until it reached failure. After breaking, the fiber was visually inspected to ensure

failure occurred in the middle of sample, validating the test methodology. If it did not break between the edges and broke at the ends where the fiber was glued to the frame, the data was not used as the fiber itself was not tested.

Fragmentation Testing: Ballistic Testing measured the strike velocity and residual velocity of a fragment simulating projectile (FSP) to quantify ballistic resistance of the material in terms of V_{50} and energy absorbed. V_{50} is the velocity required for a projectile to penetrate a material at a rate of 50% of impacts. Energy absorbed is how much energy is absorbed by the material measured using the change of velocity of the bullet. Ballistic testing was performed at the Natick Combat Capabilities Development Command's Soldier Center and consisted of a pneumatic pressure system to launch the FSP, light gates to measure the V1 and V4 used to calculate Vs and Vr, a material mount, and a FSP catcher. The FSP was a 17 grain (1.1 gram) mass with skirt removed (have sketch and image). A pneumatic pressure system was used with the ability to change a variable pressure. Upon release, the variable pressure would cause the bullet to travel at a variable speed. Light gates measured speed V1 and V4. Calibrating the system allowed for calculations of Vs and Vr. The catcher was a metal box with one side open and filled with Kevlar KM2 fabric.

Heat Insulation Testing: Heat insulation was tested by using a 600 W heating source and the temperature probes on both sides of the samples were measured to evaluate the change in temperature over time and the heat conductivity of the samples.

Statistical Analysis: To determine statistical significance, data sets were analyzed to determine if they were normally distributed. If a data set had a $n > 30$ and skewness in the range of -.5 to .5, the data set was assumed to have a normal distribution. A normally distributed group of data was then tested using a One-Way ANOVA and a Posthoc Tukey method. If data sets had a $n < 30$ or a skewness outside the range of -.5 to .5, the data set was not assumed to be normally distributed. A data set with an unknown distribution was tested using ANOVA on Ranks and a Posthoc Mann-Whitney. A p-value $< .05$ was assumed to be statistically significant. Statistical Analysis was performed in SigmaPlot 13.

Chapter 5

Changing Modes of Abrasion to Improve Wear Resistance with Kevlar Nanofibers

Wear decreases the life span of industrial and consumer products: abrasive wear between boots and the ground thins the sole, abrasive wear between moving particles in pipes eats through the surface. Even though Leonardo DaVinci began studying the fundamental laws governing friction between sliding surfaces[92], the resultant surface damage from these sliding surfaces was not studied until after the establishment of the field of tribology. The field began following the 1966 Jost Report finding that this surface damage or wear costs 1.1% of the United Kingdom's Gross Domestic Product[92]. To reduce the cost of wear on the economy, the United Kingdom funded research to understand the wear process. Several types of wear were defined based on the mechanism of mass loss. For abrasive wear, the mechanism of mass loss occurs when an asperity (an edge or particle) scratches and removes material from the surface of the product.

As an improvement to the lifespan of products undergoing abrasion, fibers were introduced into polymer matrices to decrease the overall wear rate of the product. To describe this improved lifespan, Holm and Archard developed the volume wear rate to be inversely proportional to hardness and proportional to wear coefficient. However, the additional wear resistance of the matrix is based on the volume fraction of fiber added and not the interaction of the fibers with the matrix as defined by

$$\Gamma_{composite} = \varphi_{fiber}\Gamma_{fiber} + \varphi_{matrix}\Gamma_{matrix}$$

where Γ is wear rate and φ is the volume fraction[92]. As a result, fibers for reinforced composites were developed with the highest wear coefficient: Kevlar® microfibers developed as the the leading fiber for improving the abrasion rate of bulk polymer matrices.[6] For ease of production, the fibers are short, stable

fibers without control over fiber diameter. These fibers were chosen as abrasion rate and volume ratio were assumed to be the only factors affecting wear rate. While models have attempted to extend their understanding to account for composite modulus or multiple modes of wear (abrasion and adhesive wear), the underlying mechanism of abrasive wear remains unchanged.

The mechanistic volume wear rate remains valid for abrasive wear as the asperities are assumed to be much smaller than the fibers, the characteristic length scale of the composite. This results in only one material being abraded by one asperity at a time. We hypothesized that changing the mode of abrasion from a volume friction wear rate would require the invalidation of this assumption: the asperity would need to be of equal dimension to the fibers reinforcing the composite. This change of length scale ratios will cause the interactions between matrix and fiber to be dominant. To test if the diameter of the fiber affected the abrasion resistance of the composite, epoxy reinforced with custom PPTA nanofibers were abraded and compared to the abrasion of epoxy reinforced with commercial Kevlar microfibers.

5.1 Production of Staple Nanofibers for Composite Reinforcement

In order to change the mechanism of abrasive wear, fibers need to be on the same length scale as the asperities (Figure 5.1.1). PPTA nanofibers were manufactured following the fiber spinning protocol in section 4.6 using the immersion Rotary Jet-Spinning System. To summarize, centrifugal forces extrude the PPTA-sulfuric acid dope out an orifice, through an air gap, and into a precipitating water bath. As the bath rotates, its streamlines pull the spin fibers onto a collector. After freeze drying, the fibers were chopped to decrease the fiber length to produce staple fibers. Following this procedure, the PPTA staple nanofibers had a median diameter of 1.2 μm while the staple commercial microfibers had a median diameter of 45 μm (Figure 5.1.2).

5.2 Mechanical Properties of Fiber Reinforced Composites

Kevlar commercial microfibers are commonly used to reinforce epoxies (Figure 5.2.1). One system of commercial available epoxy from FibreGlast was employed to test if the commercial, larger fibers had a decreased wear rate compared to the PPTA nanofibers. To ensure that the fiber reinforcement did not de-

Figure 5.1.1: Length scale ratio of asperities to fibers will affect the wear rate by changing the mechanism of wear. When fibers are larger than the asperity, the asperity wear either the fiber or matrix one at a time leading to a volume wear rate. When fibers are the same size or smaller than the asperity, then the asperity will pull both the matrix and fiber at the same time leading to mechanical wear rate.

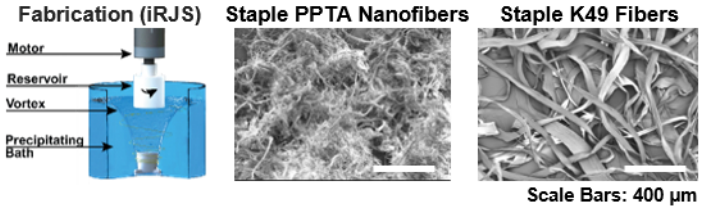

Figure 5.1.2: Staple PPTA nanofibers will be manufactured using the iRJS to make nanofibers (KNF) of a size smaller than staple commercial Kevlar 49 (K49) fibers.

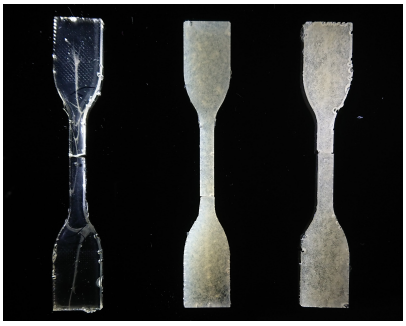

Figure 5.2.1: Representative Composite Dog Bones for Tensile Testing. From left to right: epoxy, Kevlar 49 reinforced composites, and PPTA nanofiber reinforced composites.

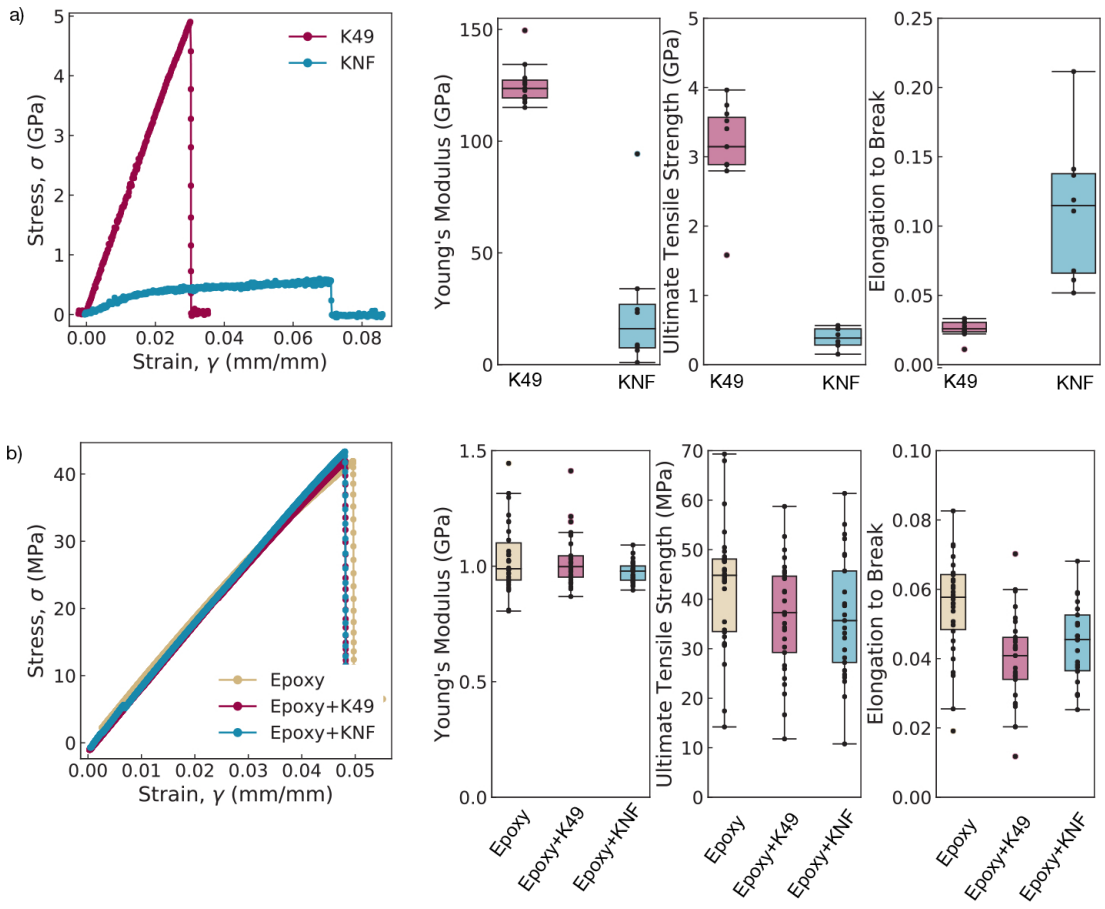

Figure 5.2.2: Mechanical properties of fibers and fiber reinforced pucks. a) Mechanical properties of fibers were analyzed by uni-axial tensile testing as seen by representative curves to determine differences in modulus, strength, and elongation to break. b) Despite difference in fiber mechanical properties, the properties of the composites had no difference among representative curves, modulus, strength, or elongation to break.

grade the mechanical properties of the reinforced composites, uniaxial tensile testing on epoxy, commercial fiber reinforced epoxy, and nanofiber reinforced epoxies were performed. Representative curves revealed that each of these sample types had equivalent Young's Modulus, ultimate tensile strength, and elongation to break. Therefore, any changes in rate of abrasive wear would not be affected by the mechanical properties of the composite (Figure 5.2.2).

5.3 Wear of Reinforced Composites Changes with Fiber-Asperity Size Ratio

To test the wear rate of the epoxy and reinforced epoxy systems, each of the types of materials were made into pucks (Figure 5.3.1). Then, an elliptical abrasion tester was employed to cycle the pucks on 400 grit

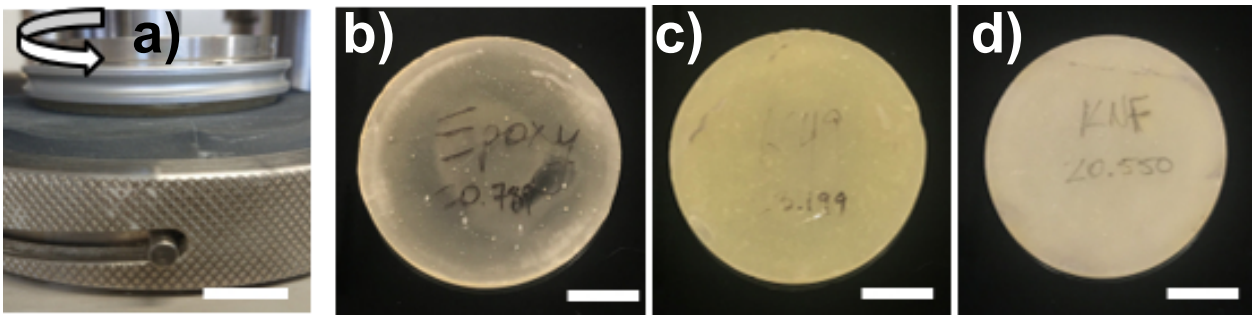

Figure 5.3.1: Abrasion testing of composites was performed on an a) elliptical tester were the pucks were moved elliptically on sand paper. Tested pucks were made from b) plain epoxy, c) Kevlar 49 reinforced epoxy, and d) PPTA nanofiber reinforced epoxy.

sandpaper. 400 grit sand paper was chosen due to its 10 μm asperity size. As the asperity size is greater than nanofibers but lower the commercial fibers, there would be a mechanistic change in abrasion rate loss. To abrade the samples, the samples were placed on the abrasion tester and tested for 130k cycles to ensure a completely abraded and evenly worn surface. After the cyclic wear, the change of mass of each sample was measured. The epoxy pucks had the greatest wear while the wear of the nanofiber reinforced puck was the smallest (Figure 5.3.2).

The change of rates of wear is attributed to a change in mechanical mode of wear from a volume fraction to mechanical fracture model. Since the nanofibers are smaller than the asperities, the asperities pull on both the matrix and the fiber simultaneously. In the case of the volume fraction wear, the asperities can only wear down either the matrix or the fiber at one time. The asperity cannot physically come in contact with both materials simultaneously. As a result, the volume fraction wear model is replaced by a fracture model of the fibers pulling from the fiber matrix

$$\Gamma_{composite} = \frac{s^3 r}{H\tau}$$

where s is the fiber strength, r is the fiber radius, H is the hardness, and τ is the friction between the fiber and matrix.

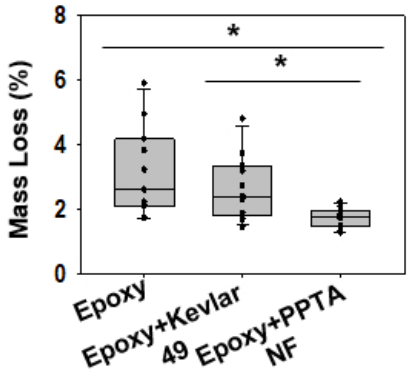

Figure 5.3.2: Wear rate of abraded pucks showed differences between the Kevlar 49 and PPTA nanofiber reinfroced composites.

5.4 Conclusions

Since the abrasion resistance increased for the nanofibers compared to the microfibers even at the same volume fraction of mixing, volume fraction models cannot be the dominant mechanism in this case. As a result, the interactions of the matrix and fiber are dominant. Despite the nanofiber filler being weaker in pure strength, we are able to increase the lifespan of the materials undergoing abrasion by using smaller fibers as a reinforcement.

5.5 Experimental Design

Epoxy and Reinforced-Epoxy Fabrication: The abrasion testing pucks were fabricated using both chopped nanofibers and Kevlar 49 pulp (Fibre Glast 544-C) as the filler and the matrix was made from System 2000 Laminating Epoxy Resin (Fibre Glast 2000-C) and 2020 Hardener (Fibre Glast 2020-C). Puck fabrication began with the stirring 36ml of System 2000 Resin on overhead mixer at 400 RPM for 3 minutes with nothing, .1g of Kevlar 49 pulp, or .1g of nanofibers. After the passing of the allotted time and upon achieving a homogeneous solution, 9ml of 2020 Hardener was added and mixed on an overhead mixer at 250 RPM for 5 minutes. The solution then was left to sit for 10 minutes, allowing the reaction to initiate. Following this step, the mixture was poured in cylindrical polydimethylsiloxane (Ellsworth Adhesives 184 SIL ELAST KIT 0.5KG) molds with a 90mm diameter and 6mm height and placed in a 120°C

oven overnight.

Epoxy Tensile Testing: Following Epoxy and Reinforced-Epoxy Fabrication, samples were molded to ASTM 638 Specimen Type 4 dog bone (25 mm gauge length). The fabricated dog bone was placed into the pneumatic grips of an Instron 5566. The dog bone was then pulled at a constant strain rate of 15% per min until it reached failure. After breaking, the dog bone was visually inspected to ensure failure occurred in the middle of sample, validating the test methodology. If it did not break between the edges and broke at the ends, the data was not used.

Chapter 6

Future Directions of Para-Aramid Nanofibers

This work has established a platform capable of producing nanofibers from polymer solutions requiring a non volatile solvent. As a result, the fabrication of unique fiber material became possible. Specifically, PPTA nanofiber sheets enabled a material to overcome the tradeoff between mechanical and heat insulation properties. In future work, the platform may enable fibers able to overcome the trade-off between strength and toughness and be able to improve the abrasion resistant of boot soles.

6.1 Overcoming the Trade-off Between Strength and Toughness

A material's strength, or its ability to withstand a force before breaking, arises primarily from its assembly of well-ordered crystalline domains. A material's toughness, or its ability to absorb energy, results from disordered amorphous phases. In traditionally engineered materials, these properties are mutually exclusive[93], leading to strong but brittle materials such as glasses, or stretchable but weak materials such as rubbers. Looking more specifically at high performance fibers, these materials have high strength values that are inversely proportional to their toughness (Figure 6.1.1), allowing them to absorb large initial forces, but often result in mechanical failure after impact forces exceed its strength. This failure arises from the fact that the fiber ratio of strength to toughness is proportional to its ratio of crystalline to amorphous phases[94] . One way that natural systems resolve this conflict is through the integration of these distinct phases[93]. For example, natural spider silks retain both high strength and toughness by having crystalline protein domains (beta sheets) dispersed in flexible amorphous regions[95]. A similar system has yet to be achieved using synthetic or produced fibers due to limitations in the current manufacturing

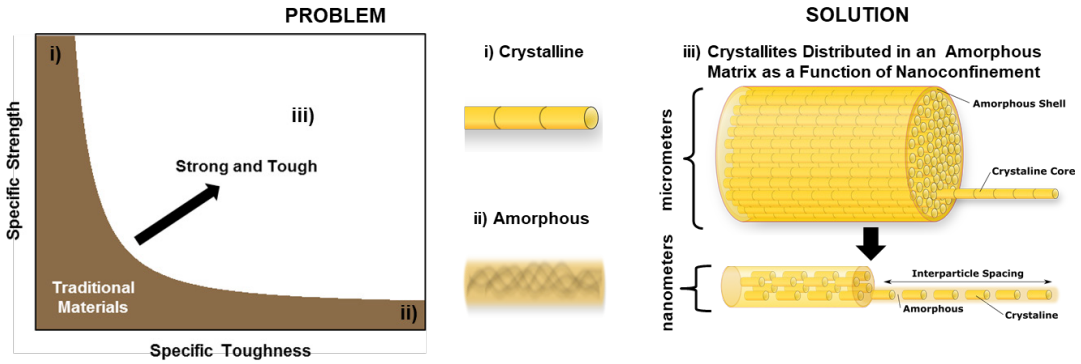

Figure 6.1.1: Overcoming the Strength-Toughness Tradeoff of Traditional Materials. a) A schematic illustrating the trade-off between strength and toughness. Materials are either i) crystalline and can withstand a large force or ii) amorphous and can absorb energy. b) We propose a new class of materials: iii) nanoconfined crystallites distributed within an amorphous phase, forming a brick-mortar structure nanofiber with high strength and toughness.

protocols. To overcome these limitations, we recently developed a nanofiber production platform where crystal formation is controlled during fiber formation[46]. Here, we will use this novel fabrication capacity to create nanofibers featuring variable ratios of crystalline/amorphous phases. Our research will focus on nanofiber production, where nano-crystallites, with length scales ranging from 20-500 nm, are confined in an amorphous matrix. We will determine the crystallite size, orientation, and distribution that maximize both strength and toughness of the material. We will then engineer these nanofibers into composites and textiles and evaluate their toughness and strength under high strain rates.

We hypothesize that trapping the crystallites into an amorphous matrix at a 1:1 ratio will result in fibers with toughness and strength higher than traditional microfibers. To test our hypothesis, we will enable nanoconfinement by spinning fibers of interest (Table 6.1.1) whose diameter are on the order of magnitude of the polymer crystallite length. For example, para-aramid fibers do not fold and have crystallites of length 500 nm; therefore, we will spin para-aramid fibers of size 500 – 1000 nm. Then, we will correlate fiber diameter to nanocrystal properties (size, orientation, and distribution) and to mechanical properties (strength and toughness).

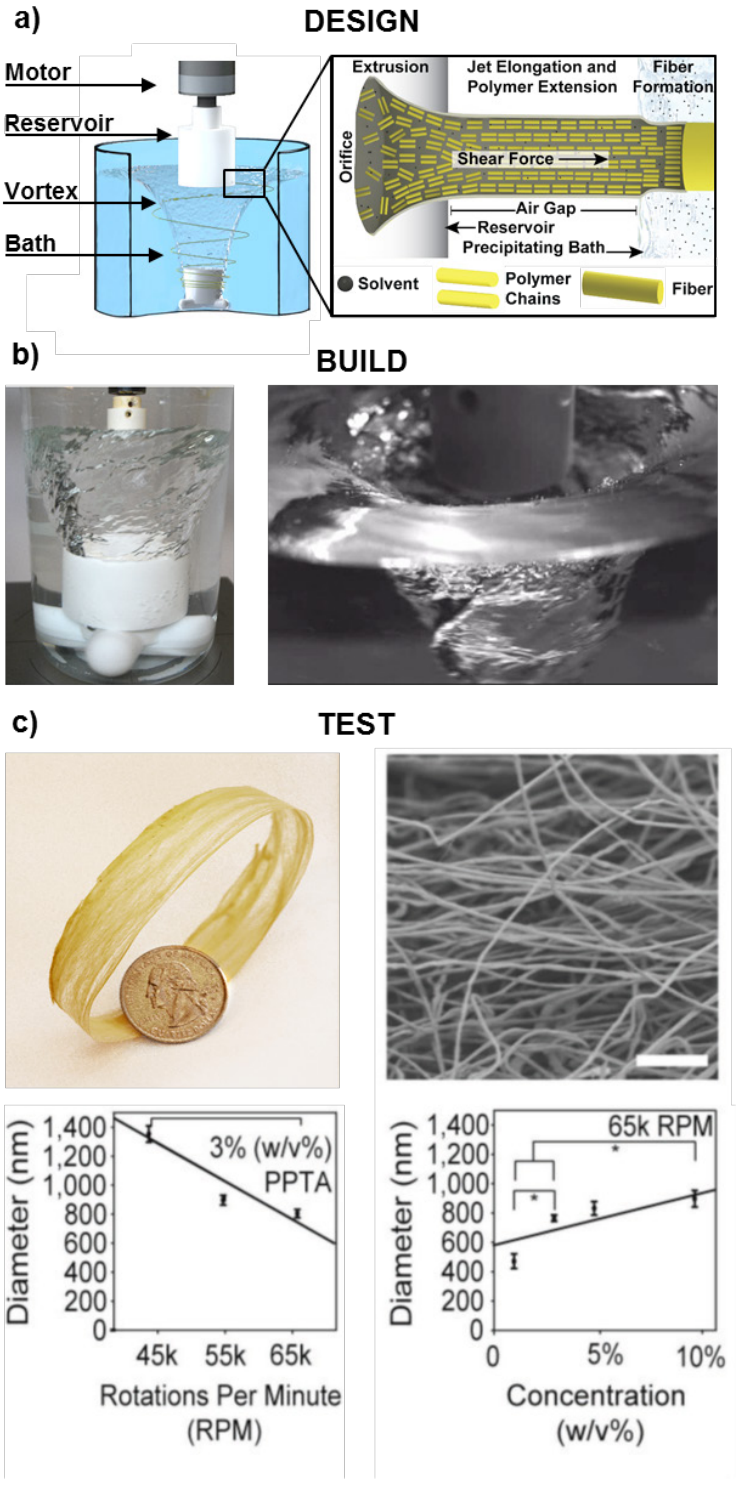

Figure 6.1.2: The immersion Rotary Jet-Spinning (iRJS) Platform to Produce Para-Aramid Nanofibers. a) The iRJS utilizes centrifugal forces to extrude a dope through an office and air gap before entering a precipitating bath where nanofiber formation occurs. b) The system was built utilizing a high-speed motor and sulfuric acid resistant materials. c) The iRJS was validated to produce para-aramid sheets consisting of nanofibers (scale bar = 40 μm) and control for diameter utilizing manufacturing parameters spinning speed and solution concentration.

Polymer Class	Polymer Name	Crystallite Length
Rigid rod, para-aramid	Poly(p-phenylene terephthalamide) (PPTA)	500 nm[94]
Flexible, thermoplastic	Ultra-high-molecular-weight polyethylene (UHWMPE)	70 nm[96]
Flexible, biopolymer	Silk	20 nm[97]

Table 6.1.1: Polymers of Interest. Listed here are the polymers that will be spun to investigate the function of nanoconfinement on mechanical properties.

Numerous applications require materials with high strength and toughness[93]. However, these mechanical properties are generally mutually exclusive since they arise from different nanoscale and microscale structures. Strength derives from crystalline structures with well-ordered bonds that respond synchronously to strain. Crystallization growth and strengthening mechanisms generally sacrifice toughness by transforming amorphous phases into crystallites. However, the resulting increase in crystal grain boundaries also increases the material's propensity to fail by crack propagation. Amorphous phases prevent crack propagation by increasing energy dispersion throughout the material. Nature overcomes this trade-off by integrating these distinct material phases as exemplified in silk's distribution of crystals within amorphous domains[93, 95]. This 'brick-mortar' structure has strength due to the crystallites and toughness since the amorphous protein bridges the individual crystal grain boundaries. Therefore, the problem we propose to solve is how to manufacture this brick and mortar structure using para-aramid polymers.

A major focus of our lab is understanding structure-function relations found in nature and their use for novel material manufacturing. Here, we apply these methods to the production of strong-tough para-aramid nanofibers. Para-aramid polymers are ideal as they do not fold, in contrast to most polymer classes, allowing for greater control of the crystallization processes. By reducing fiber diameter and ensuring rapid solidification during fiber formation, we will freeze meta-stable brick-mortar structures that increase fiber toughness without sacrificing strength.

To fabricate para-aramid nanofibers, we developed immersion rotary jet-spinning[46]. In the iRJS, fibers are formed by precipitation in a liquid bath, enabling nanofiber fabrication from non-volatile dopes (Figure 6.1.2). This includes para-aramid fibers spun from sulfuric acid solutions. No other nanofiber production platform is cable of producing these para-aramid nanofibers.

During traditional polymer manufacturing, para-aramid transitions from a liquid crystalline solution to

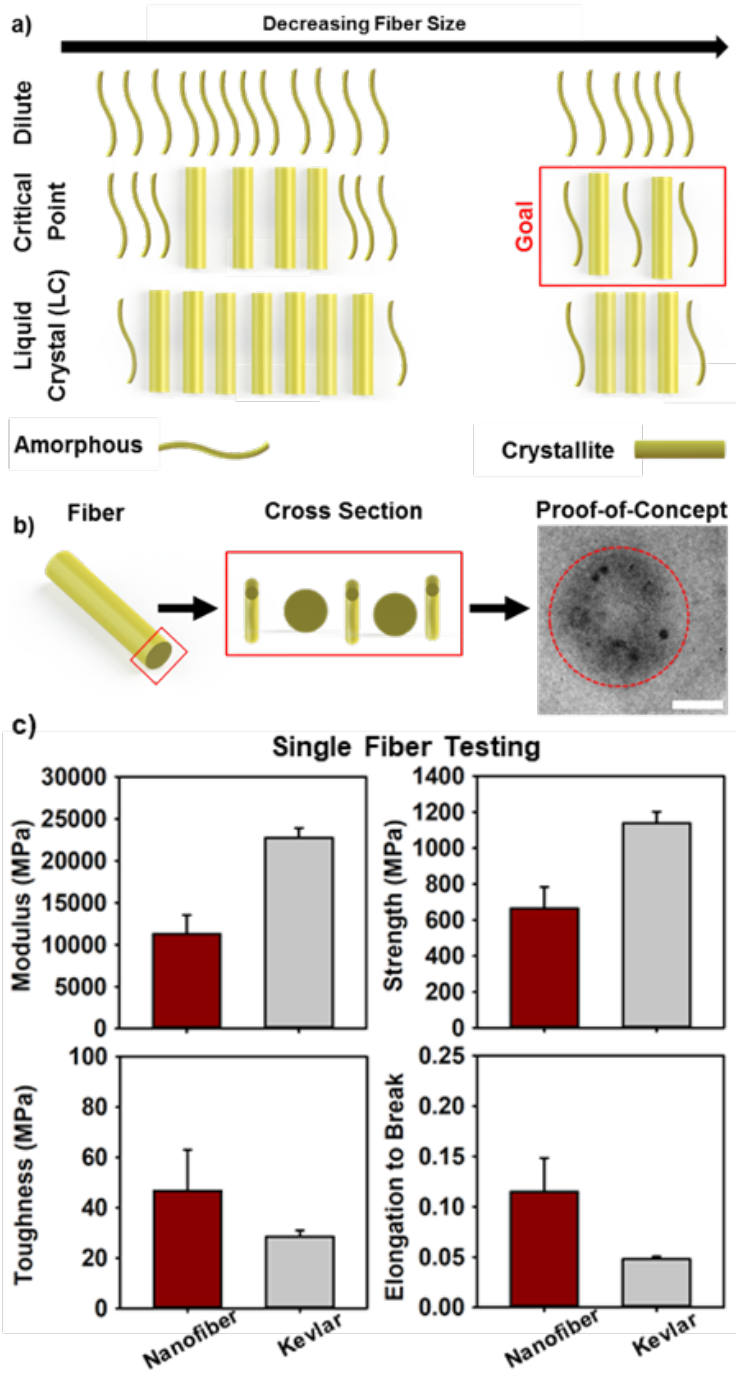

Figure 6.1.3: Freezing Metastable States of Para-Aramid Fibers to Increase Strength and Toughness. a) Geometric confinement will be used to alter the para-aramid fiber formation from dilute, critical point, and liquid crystal solutions. Decreasing fiber size will increase the timescale of solvent removal and fiber formation, allowing for the capture of the brick and mortar structure fibers. b) Fiber sectioning will be performed and visualized to measure crystallite percentage and distribution within fibers. c) Mechanical testing will be performed on single nanofibers to ensure that nanoscale observations influence the mechanical properties of the fibers.

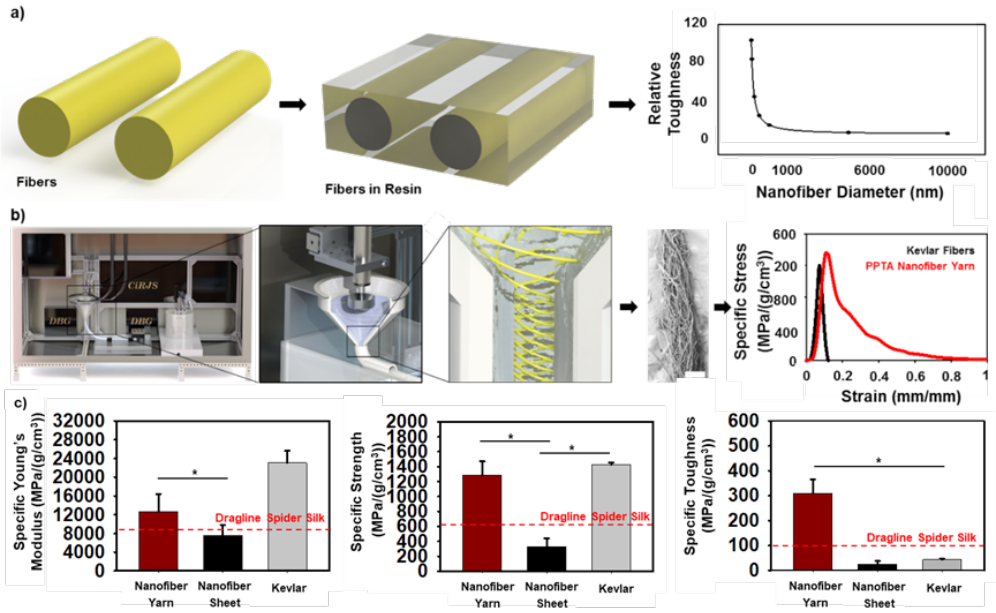

Figure 6.1.4: Validating Para-Aramid nanofiber Strength and Toughness in Macroscale Composites and Textiles. a) To make composites, nanofiber sheets will be embedded and cured in resin. Mechanical testing will be performed to validate that composite toughness increases with decreasing fiber diameter as predicted and illustrated in the graphed notional data. b) To fabricate textiles, we will utilize an already built funnel collection system to twist the nanofibers into yarns (scale bar = 200 μm). Mechanical testing will verify the increased strength and toughness of the nanofiber yarns compared to commercial fibers as represented here in hand-twisted yarns (n = 3).

an amorphous skin, crystalline core fiber. To achieve this architecture, it passes through a metastable, brick and mortar state that is not observed in the final product. However, when para-aramid fiber formation is restricted to the nanoscale, polymer crystallization will be dominated by nucleation rather than crystallite growth due to the greater surface area-to-volume ratios[98]. We hypothesize that this will result in smaller and more numerous crystallites interspersed between an amorphous phase. Furthermore, the smaller diameter fiber will allow quicker diffusion of the solvent, freezing this metastable state (Figure 6.1.3). To measure the effect of boundary conditions on crystallization, we will spin para-aramid nanofibers from dilute, critical point, and liquid crystal phases of solution to change the rate of nucleation and therefore the structure of the fiber (Figure 6.1.3a). We will then section and image the cross-section of the fibers in tunneling electron microcopy (TEM), atomic force microscopy, and scanning near field Raman microscopy to measure crystallization rate and crystallite distribution within the fiber, as illustrated in the TEM image (Figure 6.1.3). We will evaluate nanofiber mechanical properties by uni-axial tensile testing (Figure 6.1.3). These results be utilized to develop an analytic model to determine the rate of crystallite growth as a function of time and jet-elongation. Then, these parameters will be incorporated into a molecular dynamics

simulation to verify experimental results of nanoconfinement on crystallite growth and mechanics.

To engineering toughness mechanisms at larger length scales, we will produce and test composites and textile yarns. To fabricate composites, we will embed our nanofiber sheets into a matrix of polyvinyl butyral and phenolic resin using established methods. Since the toughness of a fiber composite is inversely proportional to fiber radius, we will add an additional toughening mechanism at the interface of the fibers and the resin [17]. To produce textiles, we will utilize a funnel collection system to allow the vortex streamlines to wrap individual nanofibers into yarns. With fibers twisted together, the nanofiber yarns will have an additional toughening mechanism due to increased surface force interaction between nanofibers (Figure 6.1.4). Preliminary results of nanofiber yarn mechanical data outperform nanofiber sheets, traditional high-performance fibers, and dragon line silk[99].

6.2 Nanofibers for Boot Abrasion Resistance

In addition to improving the strength of fibers to overcome the trade-off between strength and toughness as future direction of this research, the platform may be used to increase the abrasion resistance of boot soles. By changing the mechanism of abrasive wear, the smaller size of the PPTA nanofibers increased the abrasion resistance of stiff, epoxy pucks. Applying this mechanism to a polyurethane matrix, PPTA nanofibers as a abrasion resistance filler is being tested to improve the wear life of boots.

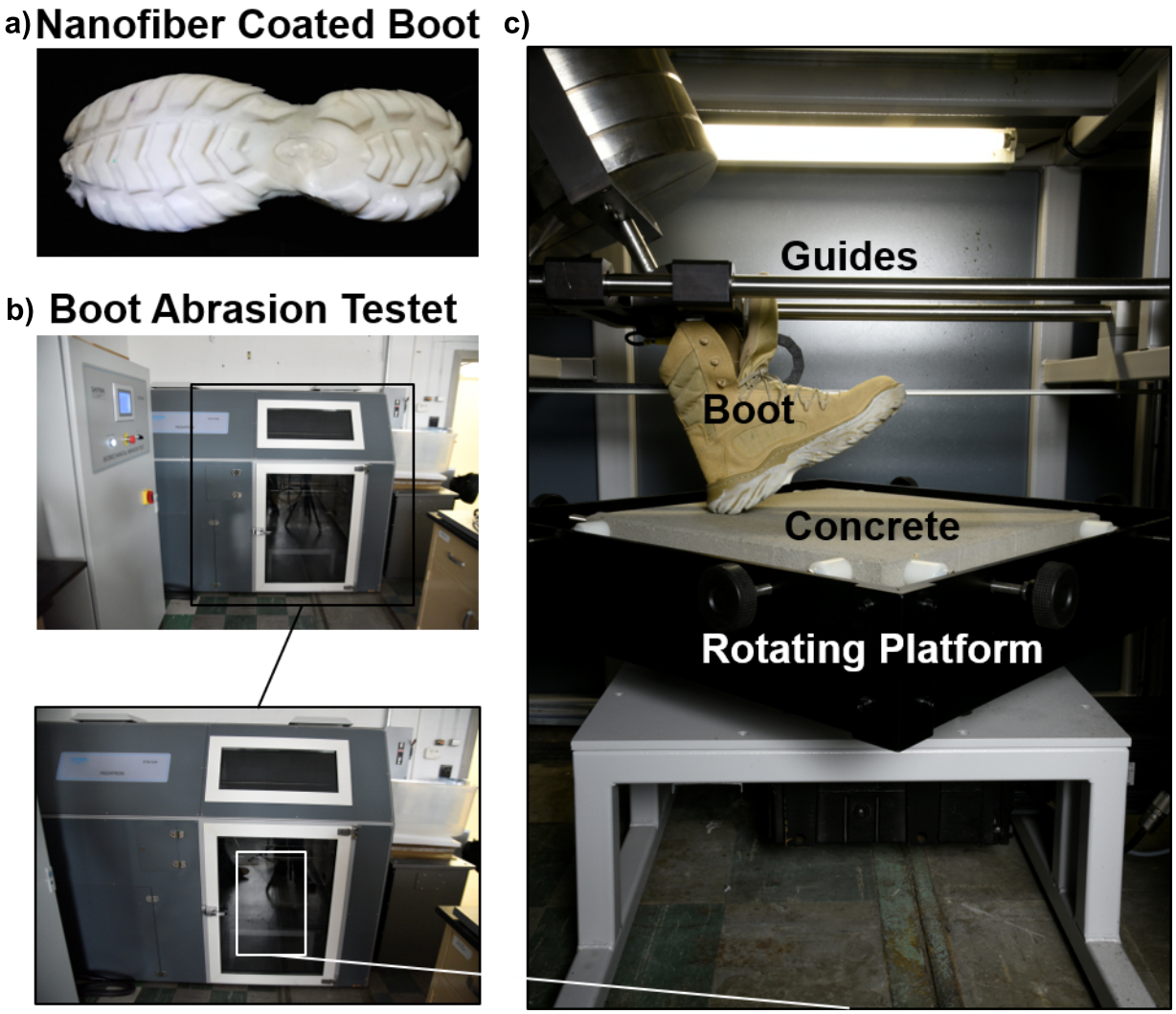

Figure 6.2.1: Abrasion Testing of PPTA Nanofiber Reinforced Polyurethane Boot Soles. a) A boot coated in PPTA nanofiber reinforced polyurethane as placed in an b) abrasion tester. To test the wear rate of the coated boot, the machine c) replicates the boot walking along a concrete bath. The concrete rotates to endure the boot does not land in the same place every step 6.2.1.

Chapter 7

Conclusion

In this work, fiber engineering has been employed to overcome extreme environments. One of the most extreme environments is the site of an improvised explosive device (IED). While Kevlar-ceramic vests protect the torso from IEDs, their weight is too great to protect the extremities without over encumbering the wearer. Materials with fragmentation protection for the extremities therefore need to add protection without adding weight. As uniforms, jackets, or tunics are worn to protect from the heat or cold, we hypothesized the addition of fragmentation protection to heat insulation would enable extremity protection from both threats simultaneously without adding weight. However, materials tend to trade-off between mechanical fragmentation protection and heat insulation. Para-armid fibers (PPTA), when structured in different forms are able to have either of the properties: woven fibers provide fragmentation protection while aerogels provide heat insulation. To overcome this trade-off, PPTA fibers would need to incorporate the structure-function of the mechanically strong fiber weaves and high-insulation fiber aerogels. To make this material, we incorporated continuous fibers with a porous network. As PPTA nanofibers were not able to be manufactured into continuous sheets, the immersion Rotary Jet Spinning (iRJS) platform was developed to solve this processing challenge. In addition, the iRJS extended the ability of nanofiber manufacturing to include the processing of polymer dopes from non-volatile solvents, not just PPTA-sulfuric acid dopes. The iRJS works by using centrifugal forces to extrude a polymer solution out an orifice, through an air gap to allow for jet-elongation and polymer alignments, and finally into a bath where the solvent diffused out of the jet to form the fiber. The bath itself is a rotating vortex: it pulls the precipitated fiber onto a collector to make a sheet of fibers. As this preliminary study only made small (.2g) sample sizes, the iRJS

system was up-scaled to allow for the continuous spinning of fiber sheets using a top loading reservoir, a larger bath, and a motorized collector. With this scaling of the iRJS, PPTA-sulfuric acid dopes were chosen to be viscous dominated during spinning to ensure jet thinning into a continuous jet and elastic dominated during collecting to ensure that jet set into a fiber without deforming. Following this procedure, PPTA nanofiber sheets were made to contain long continuous fibers running the length of the sheet while containing large pore sizes within. As single fibers had the mechanical performance to have a predicted fragmentation protection able to stop low velocity threats, fragmentation testing was performed to quantify their protection. While the PPTA nanofiber sheets had only an 85% fragmentation protection compared to commercial weaves, that 15% sacrifice enabled a 20x gain in heat insulation. As a result, PPTA nanofibers enabled a material moving towards providing simultaneous heat and fragmentation protection to survive in extreme environments. This was achieved by engineering the fiber and through the construction of fiber sheets.

This work has utilized a few of the areas in the fiber engineering field: the fundamental laws of spinning a good fiber and what is the structure of a good fiber. However, this work has not looked into either the defect mechanics of fibers or the synthesis of ideal polymers leading to high-performance fibers. To engineering future high-performance fibers, several questions in each of these area need to be addressed.

7.1 Questions to Define the Optimal Structure of a Fiber

First, the field needs to reconsider what the ideal structure of a fiber could be. Fibers generally fail at defects within a fiber. For crystalline fibers, this is at the interface between crystalline domains. To over come this limitation, it is assumed that the ideal structure will be perfectly homogeneous, containing only aligned polymer chains.[91] While this would allow for the polymer chains to fail instead of the crystalline grain boundaries, it would require a polymer chain of the same length as the intended fiber. The polymer chains would need be made continuously at the same timescale of making the continuous fiber in order to achieve this structure. Nature takes a different strategy and utilizes heterogeneous structures across multiple length scales to increase mechanical performance and decrease fault sensitivity in materials. The field of strong-tough materials has taken this fact to inspire novel mechanisms for improving mechanics of materials. The fiber engineering field should ask how to minimize and utilize defects to attain high-performing fibers by

answering the following questions:

- What are the benefits of a uniform fiber? What are the benefits of a core-shell fiber?
- At what length scale does the core-shell structure disappear?
- Can effects of defects be avoided within fibers?

High performance fibers have a core-shell structure where the skin is amorphous but contains aligned polymer chains while the core contains crystalline domains. The heterogeneous structure derives from the fact that the skin solidifies before the core, and the core has more time for crystallization to occur before complete solidification [6]. The homogeneous structure of the ideal fiber is most reflected in the shell of core-shell high performance fibers as the polymer chains are aligned but grain boundaries between polymer chain ends are minimized as the polymer chains are evenly distributed along the fiber length. Therefore, we need to enable mechanisms to study both the structure-function of the core and shell to understand how they influence fiber mechanics. Specifically, we need to see what the skin gains in elongation to break and work to rupture (energy a material absorbs before breaking) but looses in strength and modulus relative to the core.

In order to understand the the affects of the skin-core ratio on fiber mechanics, we need to study the timescale of formation for the crystalline core. Specifically, we need to understand at what length scale, due to faster diffusion, the core-shell structure disappears. By understanding at what length scale the core disappears, we can make a fiber similar to the hypothesized ideal fiber that only contains polymer chain end defects randomly distributed throughout the fiber instead of at the end of a crystalline domain. As a result, this will define the upper limit of what homogeneous fibers can obtain.

In order to improve fibers beyond a homogeneous structure, we will first need to ask if the effects of defects can be avoided. Nature uses relatively poor mechanical constituents to create strong and tough materials. This is done by using heterogeneous structures across multiple length scales. The natural design of these materials limits the effects of defects. For example, bone uses molecular uncoiling to induce plasticity, fibular sliding to constrain microcracking, fibril sliding between overlapping polymer chains, and crack bridging by collagen fibers.[93] Another material, nacre, uses a brick and mortar structure of crystals and amorphous regions to gain the mechanical benefit of both domains: the amorphous regions absorb crack-

ing along crystalline grain boundary defects while the crystal provides strength and stiffness. As the length scale effects the influence of defects, we need to ask what is the maximum size of fiber defects that does not affect its function. However, this needs to be studied from the perspective of both the fiber and mechanical engineering fields.

7.2 Questions to Define the Mechanisms of Fiber Mechanics

Between the fields of fiber engineering and mechanical engineering, several questions remain after this work that are critical in understanding how to achieve next generation high performance fibers:

- What is the flaw sensitivity of a fiber in relation to its size and geometry?
- Do nanofibers enable higher performing fibers or just enable another route to make higher performing fibers?

The limit to flaw sensitivity in materials is defined by a balance between a material's work to work to rupture (amount of energy a material can absorb before breaking) and the fracture energy (energy require to length a rip between two faces of a material).[100] While some materials have flaw sensitivity of 10 to 1 nm such as silica glass, elastomers (rubbers and polyurethanes) have a flaw sensitivity of 100 μm. For high performance, crystalline polymers, the flaw sensitivity needs to be defined. However, high-performance polymers are traditionally manufactured as fibers while fracture energy experiments have been done on rectangular objects. The field needs to develop fracture energy experiments in order to analyze the flaw sensitivity of high performance fibers and their inherent limits. Furthermore, we need to analyze if the structure of the fiber affects flaw sensitivity itself or just polymer alignment.

Nanofibers are proclaimed, within academia, to provide superior mechanical gains. However, the gains lack the achievement of commercial, traditional microfibers made from complex spinning, drawing, and annealing procedures. Each of these steps in traditional manufacturing helps induce polymer alignment along the fiber axis and to limit the amount of defects. The procedure of nanofiber spinning only seems to provide a mechanism of gaining improvements over a randomly organized fiber rather than push the field of materials science beyond traditional high performance microfibers. Nanofibers need a mechanism of improvement beyond defect sensitivity and polymer alignment. This needs to be done because their is an

inherent limit to gains made from these mechanisms.

7.3 Questions to Define the Fundamental Laws of Spinning

Discovering the limits and mechanisms of fiber mechanics only defines the limit of high performance fibers. The field needs to create a material with flaws at the length scale of flaw sensitivity. To do this, the field needs to develop the fundamental laws of spinning high performance fibers by first answering the following questions:

- What is the time scale of inter-chain bonding during flow?
- What is the barrier preventing gel-spinning of high performance nanofibers?
- What is the stability of jet?

The ideal fiber needs high polymer alignment to allow polymer chains to undergo intermolecular bonding. Therefore, we need to study the timescale of inter-chain bonding as induced by flow and shear forces. The recent coupling a Raman spectrometer with a rheometer will allow us to study and answer the time scale of polymer bonding under flow. With this time scale, we could start to understand how to build alignment within the fiber without the need of additional annealing steps and drawing. Furthermore, we need to study the barrier to spinning nanofibers from gel solutions. Higher performance fibers are usually manufactured from gel-solutions: a solution of high enough concentration to become semi-solid like a gel. Heating and high pressure extrusion of this gel is the first step in high performance manufacturing. This is key because gel solutions already contain intermolecular polymer interactions. However, most platforms spin from dilute solutions where there are no interactions between polymer chains, making it harder to induce polymer alignment. Finally, we need to define the stability of jets and the inherent length scale instability of a jet. Where will the jet be too small and therefore define the limit of our fiber size? Can we make the jet smaller by pulling on it during collection instead of just pushing on it during spinning?

7.4 Questions to Enable Functionality through Fiber Assembly

Beyond defining and building the ideal fiber, we need to create novel methods of utilizing those fibers in new constructs beyond textile weaves. To discover these new devices, we need to answer the following

questions:

- What is the role of non-wovens in ballistic protection?
- How do cells use fibers as structure? How does that inspire tensegrity structure?

First, we need to determine the role of non-wovens in ballistic protection. Traditionally, weaves have proven to have better ballistic performance as they are able to dissipate energy along fiber axes in two directions simultaneously. However, since the energy absorption and transfer mechanism of weaves is well understood, it has been easy to achieve that ideal structure. We do not understand the mechanism of energy absorption and transfer within a non-woven construct. Therefore, to build better non-wovens for ballistics, we need to understand the mechanism by which they provide ballistic protection. In addition, we need to look to create tensegrity building blocks. Cells are the building blocks of tissue and cells use fibers as structural elements to define their shape and therefore their function. We need to look at how to fabricate geometries with high compressive loads while only being fabricated from non-compressive bearing high performance fibers.

References

[1] R. C. Laible, *Ballistic Materials and Penetration Mechanics*. Elsevier, 2012.

[2] *Combat casualty care : lessons learned from OEF and OIF*. Falls Church, Virginia: Office of the Surgeon General, Department of the Army, 2012.

[3] "High performance fibers," in *High Performance Polymers and Engineering Plastics*, pp. 269–340, Hoboken, NJ, USA: John Wiley & Sons, Inc., 2011.

[4] F. Bauer, M. Kempf, F. Weiland, and P. Middendorf, "Structure-property relationships of basalt fibers for high performance applications," *Composites Part B*, vol. 145, pp. 121–128, 2018.

[5] L. Römer and T. Scheibel, "The elaborate structure of spider silk: structure and function of a natural high performance fiber," *Prion*, vol. 2, no. 4, 2008.

[6] H. H. Yang, "Kevlar Aramid Fiber," p. 2010, 1993.

[7] A. A. Griffith, "The phenomena of rupture and flow in solids," *Philosophical Transactions of the Royal Society of London. Series A, Containing Papers of a Mathematical or Physical Character (1896-1934)*, vol. 221, no. 582, pp. 163–198, 1921.

[8] J. Lyu, Z. Liu, X. Wu, G. Li, D. Fang, and X. Zhang, "Nanofibrous kevlar aerogel films and their phase-change composites for highly efficient infrared stealth," *ACS nano*, vol. 13, no. 2, 2019.

[9] C. V. Boys, "On the Production, Properties, and some suggested Uses of the Finest Threads," *Proceedings of the Physical Society of London*, vol. 9, no. 9, pp. 8–19, 1887.

[10] C. J. Luo, S. D. Stoyanov, E. Stride, E. Pelan, and M. Edirisinghe, "Electrospinning versus fibre production methods: from specifics to technological convergence.," *Chemical Society reviews*, vol. 41, no. 13, pp. 4708–4735, 2012.

[11] M. Jassal and S. Ghosh, "Aramid fibres-An overview," *Indian Journal of Fibre and Textile Research*, vol. 27, no. 3, pp. 290–306, 2002.

[12] D. Tanner, J. A. Fitzgerald, and B. R. Phillips, "The Keviar Story an Advanced Materials Case Study," *Adv Mater*, vol. 5, no. 5, pp. 151–156, 1989.

[13] V. Shabafrooz, M. Mozafari, D. Vashaee, and T. Lobat, "Electrospun nanofibers: From filtration membranes to highly specialized tissue engineering scaffolds," *Journal of nanoscience and nanotechnology*, vol. 14, no. 1, pp. 522–34, 2014.

[14] J. Lannutti, D. Reneker, T. Ma, D. Tomasko, and D. Farson, "Electrospinning for tissue engineering scaffolds," *Materials Science and Engineering: C*, vol. 27, no. 3, pp. 504–509, 2007.

[15] K. Y. Lee and D. J. Mooney, "Alginate: Properties and biomedical applications," *Progress in Polymer Science (Oxford)*, vol. 37, no. 1, pp. 106–126, 2012.

[16] C. Borselli, H. Storrie, F. Benesch-Lee, D. Shvartsman, C. Cezar, J. W. Lichtman, H. H. Vandenburgh, and D. J. Mooney, "Functional muscle regeneration with combined delivery of angiogenesis and myogenesis factors," *Proc Natl Acad Sci USA*, vol. 107, no. 8, pp. 3287–3292, 2010.

[17] J. Kim and D. Reneker, "Mechanical properties of composites using ultrafine electrospun fibers," *Polymer Composites*, vol. 20, no. 1, pp. 124–131, 1999.

[18] Z. M. Huang, Y. Z. Zhang, M. Kotaki, and S. Ramakrishna, "A review on polymer nanofibers by electrospinning and their applications in nanocomposites," *Composites Science and Technology*, vol. 63, no. 15, pp. 2223–2253, 2003.

[19] R. Vasita and D. S. Katti, "Nanofibers and their applications in tissue engineering," *International Journal of Nanomedicine*, vol. 1, no. 1, pp. 15–30, 2006.

[20] S. Paramonov, H.-W. Jun, and J. Hartgerink, "Self-Assembly of Peptide–Amphiphile Nanofibers: The Roles of Hydrogen Bonding and Amphiphilic Packing," *Journal of the American Chemical Society*, vol. 128, no. 22, pp. 7291–7298, 2006.

[21] J. D. Hartgerink, E. Beniash, and S. I. Stupp, "Self-Assembly and Mineralization of peptide-Amphiphile Nanofibers," *Science*, vol. 294, no. 5547, pp. 1684–1688, 2001.

[22] P. X. Ma and R. Zhang, "Synthetic nano-scale fibrous extracellular matrix," *Journal of Biomedical Materials Research*, vol. 46, no. 1, pp. 60–72, 1999.

[23] C. Pang, G.-Y. Lee, T.-i. Kim, S. Kim, H. Kim, S.-H. Ahn, and K.-Y. Suh, "A flexible and highly sensitive strain-gauge sensor using reversible interlocking of nanofibres," *Nature Materials*, vol. 11, no. 9, pp. 795–801, 2012.

[24] A. Tokarev, D. Asheghali, I. M. Griffiths, O. Trotsenko, A. Gruzd, X. Lin, H. A. Stone, and S. Minko, "Touch and Brush Spinning of Nanofibers," *Advanced Materials*, vol. 27, no. 41, pp. 1–7, 2015.

[25] A. Tokarev, O. Trotsenko, I. M. Griffiths, H. A. Stone, and S. Minko, "Magnetospinning of Nano and Microfibers," *Advanced Materials*, vol. 27, no. 23, pp. 3560–3695, 2015.

[26] P.-L. Josep, R.-M. Marta, U. Hartfelder, I. Imaz, D. Maspoch, and P. S. Dittrich, "Coordination Polymer Nanofibers Generated by Microfluidic Synthesis," *Journal of the American Chemical Society*, vol. 133, no. 12, pp. 4216–4219, 2011.

[27] M. Numata, Y. Takigami, M. Takayama, T. Kozawa, and N. Hirose, "Hierarchical Supramolecular Spinning of Nanofibers in a Microfluidic Channel: Tuning Nanostructures at a Dynamic Interface," *Chemistry - A European Journal*, vol. 18, no. 41, pp. 13008–13017, 2012.

[28] S. K. Smoukov, T. Tian, N. Vitchuli, S. Gangwal, P. Geisen, M. Wright, E. Shim, M. Marquez, J. Fowler, and O. D. Velev, "Scalable Liquid {Shear-Driven} Fabrication of Polymer Nanofibers," *Advanced Materials*, vol. 27, no. 16, pp. 2642–2647, 2015.

[29] H. M. Golecki, H. Yuan, C. Glavin, B. Potter, M. R. Badrossamay, J. A. Goss, M. D. Phillips, and K. K. Parker, "Effect of solvent evaporation on fiber morphology in rotary jet spinning.," *Langmuir : the Journal of Surfaces and Colloids*, vol. 30, no. 44, pp. 13369–13374, 2014.

[30] M. Badrossamay, K. Balachandran, A. K. Capulli, H. M. Golecki, A. Agarwal, J. A. Goss, H. Kim, and K. Shin, "Engineering hybrid polymer-protein super-aligned nanofibers via rotary jet spinning," *Biomaterials*, vol. 35, no. 10, pp. 3188–3197, 2014.

[31] M. Badrossamay, M. Holly, J. A. Goss, and K. Parker, "Nanofiber assembly by rotary jet-spinning.," *Nano Lett*, vol. 10, no. 6, pp. 2257–2261, 2010.

[32] P. Mellado, M. H. A, M. R. Badrossamay, J. A. Goss, L. Mahadevan, and K. Parker, "A simple model for nanofiber formation by rotary jet-spinning," *Appl Phys Lett*, vol. 99, no. 20, p. 203107, 2011.

[33] J. D. Schiffman and C. L. Schauer, "A Review: Electrospinning of Biopolymer Nanofibers and their Applications," *Polymer Reviews*, vol. 48, no. 2, pp. 317–352, 2008.

[34] J.-W. Lu, Y.-L. Zhu, Z.-X. Guo, P. Hu, and J. Yu, "Electrospinning of sodium alginate with poly(ethylene oxide)," *Polymer*, vol. 47, no. 23, pp. 8026–8031, 2006.

[35] C. A. Bonino, M. D. Krebs, C. D. Saquing, S. Jeong, K. L. Shearer, E. Alsberg, and S. A. Khan, "Electrospinning alginate-based nanofibers: From blends to crosslinked low molecular weight alginate-only systems," *Carbohydrate Polymers*, vol. 85, no. 1, pp. 111–119, 2011.

[36] C. D. Saquing, C. Tang, B. Monian, C. A. Bonino, J. L. Manasco, E. Alsberg, and S. A. Khan, "Alginate–Polyethylene Oxide Blend Nanofibers and the Role of the Carrier Polymer in Electrospinning," *Industrial & Engineering Chemistry Research*, vol. 52, no. 26, pp. 8692–8704, 2013.

[37] Y. Liu, J. Chen, V. Misoska, and G. Wallace, "Preparation of novel ultrafine fibers based on DNA and poly(ethylene oxide) by electrospinning from aqueous solutions," *Reactive and Functional Polymers*, vol. 67, no. 5, pp. 461–467, 2007.

[38] S. Safi, M. Morshed, S. A. H. Ravandi, and M. Ghiaci, "Study of electrospinning of sodium alginate, blended solutions of sodium alginate/poly (vinyl alcohol) and sodium alginate/poly (ethylene oxide)," *Journal of Applied Polymer Science*, vol. 105, no. 5, pp. 3245–3255, 2007.

[39] H. Oh, H. Pant, Y. Kang, K. Jeon, B. Pant, C. Kim, and H. Kim, "Synthesis and characterization of spider-web-like electrospun mats of meta-aramid," *Polymer International*, vol. 61, no. 11, pp. 1675–1682, 2012.

[40] H. Oh, S. Han, and S. Kim, "A novel method for a high-strength electrospun meta-aramid nanofiber by microwave treatment," *Journal of Polymer Science Part B: Polymer Physics*, vol. 52, no. 12, pp. 807–814, 2014.

[41] J. M. D. T. S Villar-Rodil, J I Paredes, A Martínez-Alonso, "Combining thermal analysis with other techniques to monitor the decomposition of poly (m-phenylene isophthalamide)," *Journal of Thermal Analysis and Calorimetry*, vol. 70, no. 1, p. 37, 2002.

[42] L. Yao, C. Lee, and J. Kim, "Fabrication of electrospun meta-aramid nanofibers in different solvent systems," *Fibers and Polymers*, vol. 11, no. 7, pp. 1032–1040, 2010.

[43] W. Yang, H. Yu, M. F. Zhu, H. W. Bai, and Y. M. Chen, "Poly(m-phenylene isophthalamide) ultrafine fibers from an ionic liquid solution by dry-jet-wet-electrospinning," 2006.

[44] R. Mead-Hunter, A. J. C. King, and B. J. Mullins, "Plateau rayleigh instability simulation," *Langmuir*, vol. 28, no. 2, pp. 6731–6735, 2012.

[45] W. Zuo, M. Zhu, W. Yang, H. Yu, Y. Chen, and Y. Zhang, "Experimental study on relationship between jet instability and formation of beaded fibers during electrospinning," *Polymer Engineering & Science*, vol. 45, no. 5, pp. 704–709, 2005.

[46] G. M. Gonzalez, L. A. MacQueen, J. U. Lind, S. A. Fitzgibbons, C. O. Chantre, I. Huggler, H. M. Golecki, J. A. Goss, and K. K. Parker, "Production of synthetic, para-aramid and biopolymer nanofibers by immersion rotary jet-spinning," *Macromolecular Materials and Engineering*, vol. 302, no. 1, p. 1600365, 2017.

[47] A. Grosberg, P. L. Kuo, C. L. Guo, N. A. Geisse, M.-A. Bray, S. P. Sheehy, and K. K. Parker, "Self-organization of muscle cell structure and function," *PLoS computational biology*, vol. 7, no. 2, p. 1001088, 2011.

[48] W. E. Teo, R. Gopal, R. Ramaseshan, K. Fujihara, and S. Ramakrishna, "A dynamic liquid support system for continuous electrospun yarn fabrication," *Polymer*, vol. 48, no. 12, pp. 3400–3405, 2007.

[49] M. Yousefzadeh, M. Latifi, W. E. Teo, M. Amani-Tehran, and S. Ramakrishna, "Producing continuous twisted yarn from well-aligned nanofibers by water vortex," *Polymer Engineering and Science*, vol. 51, no. 2, pp. 323–329, 2011.

[50] M. Yousefzadeh, M. Latifi, M. Amani-Tehran, W.-E. Teo, and S. Ramakrishna, "A note on the 3D structural design of electrospun nanofibers," *Journal of Engineered Fibers and Fabrics*, vol. 7, no. 2, pp. 17–23, 2012.

[51] K. I. Draget, O. Smidsrod, and S.-B. G., "Polysaccharides and Polyamides in the Food Industry, Properties, Production and Patents," p. 771, 2005.

[52] I. Brownlee, C. Seal, M. Wilcox, P. Dettmar, and J. Pearson, "Applications of Alginates in Food," in *Alginates: Biology and Applications*, vol. 13, pp. 211–228, 2009.

[53] H. H. Tønnesen and J. Karlsen, "Alginate in drug delivery systems.," *Drug development and industrial pharmacy*, vol. 28, no. 6, pp. 621–630, 2002.

[54] X. Zhao, J. Kim, C. A. Cezar, N. Huebsch, K. Lee, K. Bouhadir, and D. J. Mooney, "Active scaffolds for on-demand drug and cell delivery.," *Proceedings of the National Academy of Sciences of the United States of America*, vol. 108, no. 1, pp. 67–72, 2011.

[55] C. K. Kuo and P. X. Ma, "Ionically crosslinked alginate hydrogels as scaffolds for tissue engineering: part 1. Structure, gelation rate and mechanical properties.," *Biomaterials*, vol. 22, no. 6, pp. 511–521, 2001.

[56] A. D. Augst, H. J. Kong, and D. J. Mooney, "Alginate hydrogels as biomaterials.," *Macromolecular Bioscience*, vol. 6, no. 8, pp. 623–633, 2006.

[57] Bhattarai, Li, Edmondson, and Zhang, "Alginate Based Nanofibrous Scaffolds: Structural, Mechanical, and Biological Properties," *Advanced Materials*, vol. 18, no. 11, pp. 1463–1467, 2006.

[58] H. Nie, A. He, J. Zheng, S. Xu, J. Li, and C. C. Han, "Effects of chain conformation and entanglement on the electrospinning of pure alginate.," *Biomacromolecules*, vol. 9, no. 5, pp. 1362–1365, 2008.

[59] S. Jeong, M. D. Krebs, C. A. Bonino, S. A. Khan, and E. Alsberg, "Electrospun Alginate Nanofibers with Controlled Cell Adhesion for Tissue Engineeringa," *Macromolecular bioscience*, vol. 10, no. 8, pp. 934–943, 2010.

[60] G. Kim and K. Park, "Alginate-nanofibers fabricated by an electrohydrodynamic process," *Polymer Engineering & Science*, vol. 49, no. 11, pp. 2242–2248, 2009.

[61] C. A. Bonino, K. Efimenko, S. Jeong, M. D. Krebs, E. Alsberg, and S. A. Khan, "Three Dimensional Electrospun Alginate Nanofiber Mats via Tailored Charge Repulsions," *Small*, vol. 8, no. 12, pp. 1928–1936, 2012.

[62] W. Churchill, "Thoughts and Adventures," 1942.

[63] M. L. Langelaan, K. J. Boonen, R. B. Polak, F. P. Baaijens, M. J. Post, and D. W. van der Schaft, "Meet the new meat: tissue engineered skeletal muscle," *Trends in Food Science & Technology*, vol. 21, no. 2, pp. 59–66, 2010.

[64] M. J. Post, "Cultured meat from stem cells: challenges and prospects.," *Meat science*, vol. 92, no. 3, pp. 297–301, 2012.

[65] S. L. Kwolek, P. W. Morgan, J. R. Schaefgen, and L. W. Gulrich, "Synthesis, Anisotropic Solutions, and Fibers of Poly(1,4-benzamide)," *Macromolecules*, vol. 10, no. 6, pp. 1390–1396, 1977.

[66] S. Roth, M. Burghammer, A. Janotta, and C. Riekel, "Rotational Disorder in Poly(p-phenylene terephthalamide) Fibers by X-ray Diffraction with a 100 nm Beam," *Macromolecules*, vol. 36, no. 5, pp. 1585–1593, 2003.

[67] D. Xu, K. Okuyama, F. Kumamaru, and T. M. journal, "Morphorogical and structural studies on large spherulites of poly(p-phenylene terephthalamide)," *Polymer journal*, 1984.

[68] W. Judith, S. Joannès, R. Bruant, C. Clerc, M. Osa, A. Bunsell, and A. Marcellan, "Multiaxial mechanical behavior of aramid fibers and identification of skin/core structure from single fiber transverse compression testing," *Journal of Polymer Science Part B: Polymer Physics*, vol. 00, no. 00, p. 00, 2015.

[69] J. Kalantar and L. T. Drzal, "The bonding mechanism of aramid fibres to epoxy matrices - Part 1 A review of the literature," *Journal of Materials Science*, vol. 25, pp. 4186–4193, 1990.

[70] G. Srinivasan and D. H. Reneker, "Structure and morphology of small diameter electrospun aramid fibers," *Polymer International*, vol. 36, no. 2, pp. 195–201, 1995.

[71] J. Yao, J. Jin, E. Lepore, N. M. Pugno, C. W. Bastiaansen, and T. Peijs, "Electrospinning of p -Aramid Fibers," *Macromolecular Materials and Engineering*, vol. 300, no. 12, pp. 1238–1245, 2015.

[72] Y. Park, J. Lee, Y. Nam, and W. Park, "Breathable properties of m-Aramid nanofibrous membrane with high thermal resistance," *Journal of Applied Polymer Science*, vol. 132, no. 8, pp. 41515–21, 2015.

[73] C. and Siepermann, M. Yang, and W. A. Functional …, "Reactive aramid nanostructures as high-performance polymeric building blocks for advanced composites," *Advanced Functional …*, 2013.

[74] H. Yan, J. Li, W. Tian, L. He, X. Tuo, and Q. T. Advances, "A new approach to the preparation of poly (p-phenylene terephthalamide) nanofibers," *RSC Advances*, 2016.

[75] F. Croisier, A. S. Duwez, C. Jerome, A. F. Leonard, K. O. Van Der Werf, P. J. Dijkstra, and M. L. Bennink, "Mechanical testing of electrospun PCL fibers," *Acta Biomaterialia*, vol. 8, no. 1, pp. 218–224, 2012.

[76] C. L. Pai, M. C. Boyce, and G. C. Rutledge, "On the importance of fiber curvature to the elastic moduli of electrospun nonwoven fiber meshes," *Polymer*, vol. 52, no. 26, pp. 6126–6133, 2011.

[77] U. Stachewicz, I. Peker, W. Tu, and A. H. Barber, "Stress delocalization in crack tolerant electrospun nanofiber networks," *ACS Applied Materials and Interfaces*, vol. 3, no. 6, pp. 1991–1996, 2011.

[78] C. T. Koh, D. G. T. Strange, K. Tonsomboon, and M. L. Oyen, "Failure mechanisms in fibrous scaffolds," *Acta Biomaterialia*, vol. 9, no. 7, pp. 7326–7334, 2013.

[79] F. Vollrath and D. P. Knight, "Liquid crystalline spinning of spider silk," *Nature*, vol. 410, no. 6828, pp. 541–548, 2001.

[80] T.-M. Wu and J. Blackwell, "Comparison of the axial correlation lengths and paracrystalline distortion for technora and kevlar aromatic polyamide fibers," *Macromolecules*, vol. 29, no. 17, pp. 5621–5627, 1996.

[81] M. Vorechosky, V. Sadilek, and R. Rypl, "Probabilistic Evaluation of Crack Bridge Performance in Fiber Reinforced Composites," *Engineering MECHANICS*, vol. 20, no. 1, pp. 3–11, 2013.

[82] E. G. Chatzi and J. L. Koenig, "Morphology and structure of kevlar fibers: A review," *Polymer-Plastics Technology and Engineering*, vol. 26, no. 3-4, pp. 229–270, 1987.

[83] L. Penn and F. Milanovich, "Raman spectroscopy of kevlar 49 fibre," *Polymer*, vol. 20, no. 1, pp. 31 – 36, 1979.

[84] P. Kim, C. Chang, and S. Hsu, "Normal vibrational analysis of a rigid rod polymer: poly(p-phenylene terephthalamide)," *Polymer*, vol. 27, no. 1, pp. 34 – 46, 1986.

[85] K. D. Rice, A. L. Forster, M. A. Riley, and N. G. Paulter Jr, *Investigations of Near-Edge Ballistic Impacts on Law Enforcement Body Armor*. 2014.

[86] R. J. Koopmans and J. Molenaar, "The "sharkskin effect" in polymer extrusion," *Polymer Engineering & Science*, vol. 38, no. 1, pp. 101–107, 1998.

[87] R. J. Koopmans, *Die swell or extrudate swell*, pp. 158–162. Dordrecht: Springer Netherlands, 1999.

[88] H. M. Tawancy, R. B. Herchenroeder, and A. I. Asphahani, "High-performance ni-cr-mo-w alloys," *JOM*, vol. 35, no. 6, pp. 37–43, 1983.

[89] J. Lyu, Z. Liu, X. Wu, G. Li, D. Fang, and X. Zhang, "Nanofibrous kevlar aerogel films and their Phase-Change composites for highly efficient infrared stealth," 2019.

[90] P. M. Cunniff, "Dimensionless parameters for optimization of textile-based body armor systems," in *Proceedings of the 18th international symposium on ballistics*, pp. 1303–1310, San Antonio: Texas, 1999.

[91] K. Uetani and K. Hatori, "Thermal conductivity analysis and applications of nanocellulose materials," *Science and Technology of advanced MaTerialS*, vol. 18, no. 1, pp. 877–892, 2017.

[92] B. Bhushan, *Introduction to tribology*. New York: John Wiley & Sons, 2002.

[93] R. O. Ritchie, "The conflicts between strength and toughness," *Nature materials*, vol. 10, no. 11, p. 817, 2011.

[94] Y. Rao, A. Waddon, and R. Farris, "Structure–property relation in poly (p-phenylene terephthalamide)(ppta) fibers," *Polymer*, vol. 42, no. 13, pp. 5937–5946, 2001.

[95] S. Keten, Z. Xu, B. Ihle, and M. J. Buehler, "Nanoconfinement controls stiffness, strength and mechanical toughness of β-sheet crystals in silk," *Nature materials*, vol. 9, no. 4, p. 359, 2010.

[96] D. Dijkstra and A. Pennings, "The role of taut tie molecules on the mechanical properties of gel-spun uhmwpe fibres," *Polymer Bulletin*, vol. 19, no. 1, pp. 73–80, 1988.

[97] Y. Termonia, "Molecular modeling of spider silk elasticity," *Macromolecules*, vol. 27, no. 25, pp. 7378–7381, 1994.

[98] H. Wu, W. Wang, Y. Huang, and Z. Su, "Orientation of syndiotactic polystyrene crystallized in cylindrical nanopores," *Macromolecular rapid communications*, vol. 30, no. 3, pp. 194–198, 2009.

[99] F. Teulé, Y.-G. Miao, B.-H. Sohn, Y.-S. Kim, J. J. Hull, M. J. Fraser, R. V. Lewis, and D. L. Jarvis, "Silkworms transformed with chimeric silkworm/spider silk genes spin composite silk fibers with improved mechanical properties," *Proceedings of the national academy of sciences*, vol. 109, no. 3, pp. 923–928, 2012.

[100] C. Chen, Z. Wang, and Z. Suo, "Flaw sensitivity of highly stretchable materials," *Extreme Mechanics Letters*, vol. 10, pp. 50–57, 2017.